Deformed Geometries and the Gauge/Gravity Duality

Lauren Greenspan
Doutoramento em Física
Departamento de Física e Astronomia da Faculdade de Ciências da Universidade do Porto
2017

Orientador
Dr. Miguel Sousa Costa, Professor, Faculdade de Ciências da Universidade do Porto

Coorientador
Dr. João Penedones, Professor, Ecole Polytechnique Federale de Lausanne

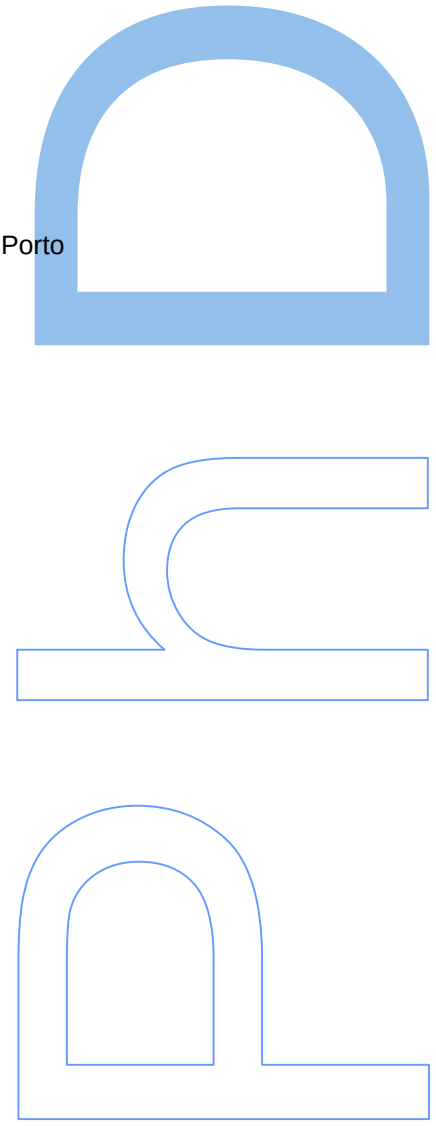

Lauren Greenspan

Deformed Geometries and the Gauge/Gravity Duality

Centro de Fisica do Porto
Departamento de Física e Astronomia
Faculdade de Ciências da Universidade do Porto

Fevereiro de 2017

Acknowledgements

I am extremely fortunate to have had the opportunity to broaden my academic and cultural horizons by pursuing my PhD in Porto. It was a pleasure to be supervised by Miguel Costa and João Penedones, and I am immensely grateful for their guidance, patience, and refreshing humanity. They each have a particular intuition for their work, and I enjoyed learning from the ways they think about, learn, and discuss physics.

I never imagined that I would be given the chance to travel and learn from so many physicists at excellent institutions worldwide. I am extremely grateful for collaborations with Jorge E. Santos and for his very patient mentoriship in the numerical methods necessary for all of the work in this thesis. I would also like to thank Benson Way, for making himself available to answer the most inane of my questions. I was also fortunate to spend a lot of my time during my PhD at the Perimeter Institute for Theoretical Physics, where I had countless discussions with many interesting people. In particular, I would like to thank Pablo Bosch and Stephen Green for enlightening conversations. I am eternally grateful for PI for giving me the necessary background and confidence to pursue a PhD in physics, and for the amazing network of PSI students that provided me with friendship and support throughout my PhD.

My time at CFP was greatly improved by the other students and postdocs there. Thanks to Catarina Cosme, Jisha Chandroth, Vasco Gonçalves, Miguel Oliveira, and others for impromptu bouts of laughter, physics help, and Portuguese lessons that brought relief to tough days. I would especially like to mention Emi Trevisani for engaging in useful discussions, exploring new places with me, and for taking on the task of becoming my first great friend in Portugal.

I would also like to thank Florbela Martins, and the rest of the CFP staff, for facilitating all that goes on behind the scenes and making my life infinitely easier. As for funding, my studies would not have been possible without the financial support from FCT/IDPASC under fellowship SFRH/BD/51983/2012.

My experience so far from home would have been incredibly lonely if not for the friends I made outside of the department. I enjoyed dancing, cooking, eating, and sharing stories and experiences with each of you. While in Portugal, it was a comfort to know I had friends back home in New York to keep in touch with. Thanks for making time for me, for inspiring me in all sorts of ways, and for letting me try and teach you physics. Thanks most of all to PL, for supporting my adventure

abroad, never accepting my self doubt, and always being there.

I am indebted to my incredible, unconventional family, especially my dad, for allowing me to pursue what made me happy, my brother Ethan, for his infinite love and laughter, and to my mom, for absolutely everything. Thank you for your support, for keeping me sane and grounded, and for believing in me.

Abstract

In this thesis, we use state of the art numerical methods to study three new examples of polarized geometries with particular emphasis on their roles in the gauge/gravity duality. The gauge/gravity duality is of great theoretical interest as it allows us to relate the difficult problems of strongly coupled field theories with those of easier to solve space-time geometries. Of these geometries, there are few analytical examples. The numerical solutions constructed in this thesis therefore encompass a novel contribution to gauge/gravity duality research. In each example, we consider static and stationary solutions to the Einstein equations and perform the corresponding thermodynamic analysis resulting in a phase diagram that could be used to describe a dual field theory at strong coupling. First, we will discuss asymptotically AdS_4 solutions deformed by a constant electric field. Next, we consider coupling this solution to a neutral scalar field. The resulting geometries are dual to deformed ABJM theory in three dimensions. Finally, we construct the asymptotically flat, 11 dimensional black hole solutions dual to the deconfined phase of the BMN matrix model. The BMN matrix model can be studied directly at strong coupling using Monte Carlo techniques, providing an important test of the gauge/gravity conjecture by way of our strong coupling prediction.

Resumo

Nesta tese usamos métodos numéricos avançados para estudar três exemplos de novas geometrias polarizadas, dando especial ênfase aos papéis que estas desempenham na dualidade gauge/gravity. Esta dualidade é de grande interesse teórico, pois permite relacionar o problema de teorias de campo fortemente acopladas, que são de difícil resoluç ão, com problemas de geometrias espaço-tempo, mais fáceis de resolver. Existem poucos exemplos analíticos destas geometrias. Portanto, as soluções numéricas construídas nesta tese constituem uma nova contribuição na pesquisa sobre a dualidade gauge/gravity. Em cada exemplo, consideramos soluções estáticas e estacionárias das equações de Einstein e realizamos a análise termodinâmica correspondente, que resulta num diagrama de fases que poderá ser utilizado para descrever uma teoria de campo dual em acoplamento forte. Primeiro, discutimos soluções que são assintoticamente AdS_4 deformadas por um campo eléctrico constante. De seguida, consideramos acoplar esta solução a um campo escalar neutro. As geometrias resultantes são duais à teoria ABJM deformada em três dimensões. Finalmente, construímos soluções de buracos negros assimptoticamente planas em 11 dimenções, duais à fase desconfinada do modelo de matriz BMN. O modelo de matriz BMN pode ser estudado directamente no regime de acoplamento forte com técnicas de Monte Carlo, fornecendo um teste importante da conjectura gauge/gravity através da nossa previsão de acoplamento forte.

Contents

List of Figures

Chapter 1

Outlook

An important goal of theoretical physics is to find a coherent way to explain all of the fundamental forces in the universe. Such a unified framework requires a theory of quantum gravity, a quantum mechanical theory described by general relativity at low energy. String theory is one of the best known examples. It hinges on the idea that all matter is made up of tiny, vibrating strings that look like localized, particle-like excitations when observed from the human scale, giving rise to the fundamental particles seen in nature and providing a quantum mechanical description of their interactions. All string theory spectra contain a massless spin two particle that plays the role of a graviton, making it a theory of quantum gravity. At low energies, string theory reduces to supergravity which contains gravitational interactions described by general relativity, resulting in a UV complete gravitational theory.

There is a well-known correspondence between string theories in certain backgrounds and field theories. At weak coupling, these can be studied by perturbation theory. In principle, however, it is very difficult to study directly the dynamics of the strongly coupled theory that is often of interest to physicists. Such strongly coupled systems are present in many different areas of physics and include QCD and quark confinement, the big bang, and high temperature superconductors. Theoretical techniques like integrability are able to solve highly symmetric cases like $\mathcal{N} = 4$ super Yang Mills, but this leaves many theories that more accurately describe the world we live in out of reach. In order to study theories which are not protected by supersymmetry or solvable by integrability, we need a different set of tools.

The gauge/gravity duality offers another such approach. It says that a strongly coupled gauge

theory in d dimensions can be related to a theory of gravity in $d+1$ dimensions. A nice way to view the duality is to consider the fact that type II string theory contains solitonic objects called branes as well as open and closed strings. String modes propagate in the bulk of AdS as well on the branes, and all of the modes can interact with each other. On one hand, the dynamics of the N Dp-branes and the open strings that end on them can be described by a $U(N)$ gauge theory. On the other hand, the branes act as sources for closed strings; they form bound states in which closed strings interact. This description is given by a string theory on a certain gravitational background. In the limit in which the open and closed string modes decouple from one another, we can consider the open and closed string sectors independently. In this way, the gauge/gravity duality is a dual description of branes as well as open and closed strings. If we then consider each theory in the low energy limit, the gauge theory becomes strongly coupled and the string theory reduces to a supergravity coupled to gauge fields encoding the D-brane charges. Hence the duality allows us to trade a difficult, strongly coupled problem for an easier gravitational one.

Since the gauge theory lives in one less dimension than the theory of gravity, the correspondence is often called "holography." In the same way that a two dimensional image creates a three dimensional hologram without needing any extra information, gravity in the bulk encodes the same content as the theory living on its boundary. There is a conjectured dictionary that translates the calculation of bulk and boundary observables. As an example, consider a gapless UV fixed point described by a conformal field theory. The Anti-de Sitter (AdS) geometry corresponds to a vacuum state of this theory, which lives on the AdS boundary. Local operators on the boundary are mapped to fields in the bulk and depend, in particular, on their asymptotic behavior. These fields deform the bulk geometry and give a contribution to the corresponding boundary stress energy tensor. There is a one to one map between bulk gauge symmetries and conserved currents, or global symmetries, on the boundary. Since the gauge/gravity duality has such a crucial role in this thesis, we give an overview of this duality in chapter two, with particular emphasis on its dual brane description.

The gauge/gravity duality is perhaps one of the most powerful tools in theoretical physics, as it allows us to solve a very complicated, strongly coupled system by solving the Einstein equations for its corresponding bulk geometry. These are a set of nonlinear partial differential equations with lamentably few analytic solutions. Numerically, however, one can scan the landscape of spacetime geometries on a computer to find interesting new solutions. Numerical methods have been developed

to run dynamical simulations of phenomena like black hole binaries, turbulence, and instabilities. There is also a whole world of interesting new static and stationary solutions such as deformed horizons and non-spherical topologies. This thesis will focus on the latter class. By studying the thermodynamics of such static solutions, we will gain insight on the phase structure of their strongly coupled field theory duals.

The third chapter sketches the numerical toolkit used throughout the thesis. The Einstein field equations are of hyperbolic type. In other words, they formulate an initial value problem and are well-posed to study time evolution. For static solutions, we instead need a boundary value problem defined by a set of elliptic PDEs. In this thesis, we employ the deTurck trick to fix the residual gauge freedom in the equations of motion, resulting in the Einstein-deTurck equations, which are elliptic in nature. Once we have a well-posed boundary value setup, we solve our systems using spectral methods and a Newton-Rhapson scheme. Spectral methods define basis functions and derivatives using all points on a grid, and converge with fewer gridpoints compared to finite difference methods. The problems considered in this thesis are all codimension two, with all functions dependent on a radial and angular coordinate. In general, we will expand the radial direction in a Chebyshev basis and the angular direction in a Fourier basis.

In the fourth chapter, we put these numerical techniques into practice by looking at geometries in four-dimensional anti-de Sitter (AdS) space-time that are polarized by an external electric field. AdS behaves like a box, with a well-defined boundary at spatial infinity. Unlike flat space, this box effectively bounds the electric field so we can study its effect on spacetime geometry. Such polarized geometries are solutions to Einstein-Maxwell theory with a negative cosmological constant that asymptote to global AdS_4 with conformal boundary $S^2 \times \mathbb{R}_t$. We turn on a space-dependent electrostatic potential which preserves the asymptotic AdS behaviour. For simplicity we focus on the case of a dipolar electrostatic potential. We find two new geometries: (i) an AdS soliton that includes the full backreaction of the electric field on the AdS geometry; (ii) a polarised neutral black hole that is deformed by the electric field, accumulating opposite charges in each hemisphere. For both geometries we study boundary data such as the charge density and the stress tensor. For the black hole we also study the horizon charge density and area, and further verify a Smarr formula. Then we consider this system at finite temperature and compute the Gibbs free energy for both the AdS soliton and black hole phases. The corresponding phase diagram generalizes the Hawking-Page phase transition. The AdS soliton dominates the low temperature phase and the

black hole the high temperature phase, with a critical temperature that decreases as the external electric field increases. Finally, we consider the simple case of a free charged scalar field on $S^2 \times \mathbb{R}_t$ with conformal coupling. For a field in the $SU(N)$ adjoint representation we compare the phase diagram with the above gravitational system.

Chapter four offers a novel application of the numerical methods as well as a worked example of the black hole thermodynamics developed in chapter two. However, in order to get a complete picture of black hole polarization in the gauge/gravity framework, we must consider Einstein-Maxwell theory coupled to a scalar field. This is dual to ABJM theory in 3 dimensions. In chapter five, we study the thermodynamics dual to ABJM at strong coupling. ABJM is a superconformal Chern-Simons matter theory that can be described by a configuration of M2 branes in the decoupling limit. Three dimensional ABJM is dual to string theory on $AdS_4 \times \mathbf{CP^3}/\mathbb{Z}_\mathbf{k}$ [1]. At low energy, this can be described by a consistent truncation of type IIA supergravity coupled to one scalar field and one gauge field. Again, we find two branches of solutions corresponding to soliton and black hole geometries. For a certain range of the electric field $\mathcal{E}$, we find two distinct branches of the AdS soliton that exist for the same value of $\mathcal{E}$. For the black hole, we find between two and four branches depending on the value of the electric field and horizon temperature. These branches meet at critical values of the electric field and impose a maximum value of $\mathcal{E}$ that should be reflected in the dual field theory. For both the soliton and black hole geometries, we study boundary data such as the stress tensor. For the black hole, we also consider horizon observables such as the entropy. At finite temperature, we consider the Gibbs free energy for both phases and determine the phase transition between them. We find that the AdS soliton dominates at low temperature for an electric field up to the maximum value. Using the gauge/gravity duality, we propose that these solutions are dual to deformed ABJM theory and compute the corresponding weak coupling phase diagram.

The above two examples can be compared with field theory calculations at weak coupling. In certain instances it is possible to find examples of the gauge/gravity duality that allow us to test the correspondence by comparing computations on both sides in the strong coupling regime. We can do this by considering the large N reduction [2] of gauge theories to a Matrix Quantum Mechanics (MQM). The reduced $0+1$-dimensional theories can be more easily simulated on a computer using Monte Carlo techniques, and the results can be compared with their AdS duals. This gives us access to regimes that are not protected by supersymmetry and that cannot be computed using

integrability.

The D0-brane MQM is one such known example. Also known as BFSS, after the authors in [3], the theory contains an $SO(9)$ global symmetry as well as nine bosons and sixteen fermions, each in the adjoint of $SU(N)$. Finite temperature Monte Carlo simulations of BFSS were found to match low temperature predictions from the dual BH thermodynamic analysis including, remarkably, quantum corrections [4, 5]. This was a highly non-trivial test of the gauge/gravity duality as it was able to match observables on both sides in the strong-coupling regime. BFSS, however, has an ill-defined canonical ensemble. This instability is suppressed at large N, but it means that only metastable states can exist at finite temperatures. Instead, we consider a massive deformation of BFSS, called the BMN matrix model [6]. The mass terms added to the Lagrangian to achieve this deformation acts as a potential, containing the D0-banes and resolving the instability. The mass can also be used to define two dimensionless parameters with which to parametrize a phase diagram: the temperature and coupling. At zero 't Hooft coupling, this theory undergoes a Hagedorn phase transition. This continues to a confinement/ deconfinement phase transition at weak coupling.

At the level of the Lagrangian, this theory coincides with the truncation of $\mathcal{N}$=4 Super Yang Mills (SYM) to its zero modes on a 3-sphere. It is reasonable, then, to assume that our system also undergoes a Hawking-Page-like phase transition at strong coupling, as it does in $AdS_5 \times S^5$, the supergravity dual to $\mathcal{N}$=4 SYM. This is precisely what we found [7]. By turning on a gauge field in the non-extremal D0-brane background, we numerically construct the supergravity solutions dual to a massive deformation of the BMN matrix model at strong coupling and study the corresponding thermodynamics. We so this by solving the bulk equations of motion, using the boundary conditions to maintain the D0-brane asymptotics while turning on the appropriate non-normalizable mode at the boundary that corresponds to the relevant deformation from BFSS to BMN. By monitoring the free energy of these solutions, we find the critical temperature marking a first-order phase transition. Below this temperature, the black D0-brane is no longer thermodynamically favored and the dominant phase is that of the vacuum, which can be described by the Lin-Maldacena geometries [8, 9]. As a highly non-trivial test of our numerics, we also construct a Smarr formula, which exploits the inherent symmetries of a problem to relate physical quantities at the horizon with those at the boundary [10].

A Monte Carlo search has already been done at a single fixed temperature [11]. Compared with our result, it implies a non-monotonic behavior of the critical temperature as a function of

the coupling. A more systematic Monte-Carlo simulation of the BMN matrix model is ongoing, and the preliminary picture seems to confirm our result, thus reinforcing evidence in favor of the gauge/gravity duality.

Chapter 2

The Gauge/ Gravity Duality

Dualities in theoretical physics are powerful and often surprising tools, connecting academic fields that would otherwise have little to do with one another. They generally relate physics at two different regimes, exploiting a mapping of symmetries or physical observables between the two sides of the correspondence. In some cases, a duality is a reductionist tool. For example, each of the consistent string theories known to us are related by dualities, leading to the discovery that each corresponds to a different limit of a single string theory. In other cases, dualities relate two qualitatively different theories. The gauge/gravity duality is one such example. It relates two completely distinct but physically equivalent formulations with a one to one map between states in each theory. The duality can be thought of in several ways. First, it can be used to relate a strongly coupled field theory to a weakly couple gravitational theory, thus establishing a strong/weak duality. It is also built on a foundation of D-branes, leading to a dual description of them. Lastly, the D-brane duality arises from the decoupling limit of string theory, leading to an open/closed string duality. These varied perspectives open string theory and its duals up to many different points of view and ways of thinking.

The original motivation for string theory was to describe strong particle interactions. The high energy behavior of strong interactions is described by QCD, an $SU(3)$ Yang Mills theory, which contains 1-dimensional string-like objects called flux tubes which form between separated quarks and anti-quarks. However, at low energy the theory becomes strongly coupled and difficult to study.

If we consider instead an $SU(N)$ gauge theory, we can do a perturbative expansion in the dimensionless parameter proportional to $1/N$, which behaves like a coupling constant for string

interactions in the limit where N is large. Feynman diagrams now naturally organize themselves in powers of $1/N$ and λ. So instead of tuning the Yang Mills coupling g_{YM}, there is a new 't Hooft coupling $\lambda = g_{YM}^2 N$ which governs the field theory in the large N limit[12]. The 't Hooft limit is reached for $N \to \infty$ while keeping λ fixed. Moreover, the diagrammatic expansion is of the same form as that for closed oriented strings with coupling constant $g_s \sim 1/N$, suggesting a deep relation between string theories and gauge theories.

What are the properties of a string theory dual to an arbitrary gauge theory? If one attempts to construct a string theory dual to, for example, a 4-dimensional gauge theory, it is necessary to couple the string world sheet to a Louiville type field which arises from the string quantization in four dimensions. The system can then be viewed as a Kaluza-Klein reduction of a 5-dimensional string theory. Thus the duality is holographic, it relates a $d+1$-dimensional string theory with a d-dimensional gauge theory that lives on its boundary.

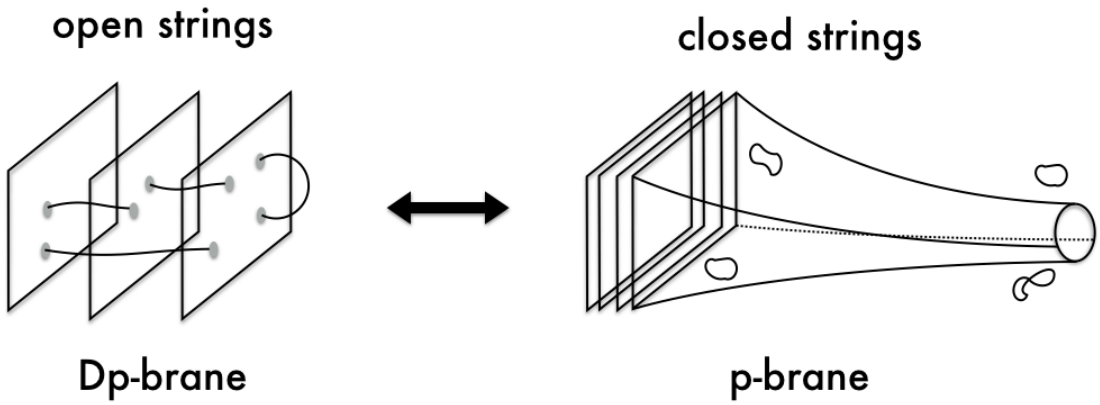

Figure 2.1: A dual picture of D-branes

The holographic connection between gauge and string theories is intrinsic to the gauge/gravity duality, and can be better understood by considering branes and their dual nature. Branes are solitonic objects in string theory. Closed strings move around in brane backgrounds and split into open strings when they come in contact with the branes, which then act as dynamical endpoints for open strings. Consider figure 2.1, which gives a sketch of the duality. Seen from the open string point of view, the figure shows a stack of N branes with open strings stretched between them. From the closed string perspective, we see that the branes source a geometry in which closed strings interact. The gauge/gravity duality relates the two sides of this image by either zooming in to or away from the branes. Up very close, we see each of the individual degrees of freedom

of the branes and open strings. Very far away, we lose the branes as separate objects and see only a (possibly) hot, dense, and charged object that deforms the spacetime around it. In order to isolate these perspectives, we should restrict ourselves to the region where the open and closed string modes decouple from one another. This means that in the effective action for the massless string modes

$$S = S_{open} + S_{closed} + S_{int}, \tag{2.1}$$

we should take the limit where $S_{int} \to 0$. This excludes terms that couple background spacetime fields to fields living on the brane. Expanding the action at weak coupling in powers of the string scale l_s, we get an action for massless string modes plus stringy excitations. To leading order, $S_{int} = 0$ and the open and closed string modes decouple from one another. This is known as the decoupling, or low energy, limit.

The strongest form of the gauge/gravity duality states that string theory on a certain background is dynamically equivalent to a quantum field theory living on its boundary. When the field theory is strongly-coupled, string theory is weakly-coupled, and visa-versa, making this a strong/weak coupling duality. This is valid for any value of N and 't Hooft coupling $\lambda = g_{YM}^2 N \sim g_s N$. A weaker form of the correspondence exists in the so-called 't Hooft limit, which takes N to be large while keeping λ fixed. In this region of parameter space, the field theory is in the planar limit. The dual string theory is classical and the string coupling is small, suppressing string loop corrections. A genus expansion in the string theory can be mapped to a $1/N$ expansion in the field theory. It is often desirable to consider the limit in which the field theory is strongly coupled. This is also known as the large 't Hooft limit $\lambda \gg 1$ and corresponds to the low energy limit of string theory described by supergravity, when the string length l_s is small compared with the radius of curvature. This is the weakest form of the duality and is where we will focus our attention throughout this thesis.

In this chapter, we aim to make the above claims more precise. First, we review the gauge/gravity duality with a particular emphasis on its brane construction, summarizing the key results of [13], [14], [15], and [16]. Consider for clarity that p-branes are objects in supergravity and Dp-branes the objects in the field theory. We focus on the gravity side, which is the cornerstone of this thesis. First, we discuss the role of branes in string theory and how they arise on both the gauge and gravity sides of the duality. Next, we derive some bulk observables, including the temperature and entropy of the black brane horizon. Finally, we relate asymptotic bulk quantities to observables

of the boundary field theory. These include the boundary stress tensor and energy. These are the tools we will need to study the black hole thermodynamics and generate a phase diagram describing the strongly-coupled system.

2.1 Dp-branes: A Field Theoretic Description

Consider the open string sector in type II string theory. In flat space, the dynamics are described by the Polyakov action. In the conformal gauge, the bosonic part can be written as

$$S = \frac{1}{4\pi\alpha'} \int d\tau d\sigma \partial_\mu X^a \partial^\mu X_a, \tag{2.2}$$

where τ and σ are the coordinates of the string world sheet denoted by greek letters $\mu = 0, ..., d-1$, and $\alpha' = l_s^2$ where l_s is the string length. In order to solve for the motion of the string X, we must specify boundary conditions at its endpoints $\sigma = 0, \pi$. These can be of Neumann or Dirichlet type. Neumann boundary conditions allow the endpoints of the string to move freely, while Dirichlet conditions fix them to a point in space. What is special about this point? Consider the endpoints of a string in d dimensions with Neumann boundary conditions for p of the $d-1$ endpoint coordinates and Dirichlet boundary conditions for the remaining $d-p-1$.

$$\begin{aligned} \partial_\sigma X^a &= 0, \quad a = 0, ..., p \\ X^a &= c^a, \quad a = p+1, ..., d-1, \end{aligned} \tag{2.3}$$

where a is a worldvolume index. This breaks the Lorentz group such that $SO(1, d-1) \to SO(1, p) \times SO(d-p-1)$. In other words, the endpoints of the string lie in a $(p+1)$-dimensional hypersurface called a Dp-brane, for the space of *D*irichlet boundary conditions in p spatial dimensions. D0-branes, which we will consider later, are also called D-particles, D1 branes are string, and so on. If $p = d-1$ and all of the string boundary conditions are of Neumann type, the D-branes are not localized at any specific points and fill the space. There is also D(-1)-branes, or D-instantons, which are localized in time and related to tunneling effects.

By looking at the mode expansion for open strings with Dirichlet boundary conditions at both ends, one finds that the momentum

$$p^a = \int_0^\pi d\sigma \frac{\partial_\tau X^a(\tau, \sigma)}{2\pi\alpha'} \tag{2.4}$$

is not conserved. This is because the brane breaks translational invariance in this direction, impeding the flow of momentum. This implies that branes are dynamical objects that respond to background fields such as gravity, just liked the strings that end on them. Open string endpoints have charges analogous to charged point particles that deform the brane by coupling to gauge fields living on it.

We will now look more closely at how the open string sector is described by a gauge theory in the decoupling limit. Keeping only the lowest energy field of type II string theory, we get the Dirac-Born-Infeld, or DBI action

$$S_{DBI} = \frac{-1}{(2\pi)^p \alpha'^{(p+1)/2}} \int d^{p+1}\xi e^{-\Phi} \sqrt{-\det\left(g_{ab} + B_{ab} + 2\pi\alpha' F_{ab}\right)}, \tag{2.5}$$

where ξ are the coordinates of the D-brane worldvolume, ϕ is a dilaton, F is the field strength of a one-form gauge field A living on the brane, and g_{ab} and B_{ab} are the metric and Kalb-Ramond 2-form field "pulled back" to the D-brane world volume

$$g_{ab} = \frac{\partial X^A}{\partial \xi^a} \frac{\partial X^B}{\partial \xi^b} g_{AB}. \tag{2.6}$$

This comes from the insertion of a graviton vertex operator in the string theory. How can we understand the physical meaning of the constants in the above action? First, holes in the string worldsheet add a factor of $e^{2\Phi}$ to the Euler characteristic. Since holes are interpreted in string perturbation theory as loops and these are governed by the string coupling g_s, it is natural to identify the dilaton with the string coupling as $e^{\Phi} = g_s$. If B and F are set to zero, the DBI action looks like the polyakov action (2.2) for the fundamental string. The prefactor $\left((2\pi)^p g_s \alpha'^{(p+1)/2}\right)^{-1}$ then acts like the tension T_p of the D-branes. The tension, and energy, scale as $1/g_s$, which blows up when the string coupling is small. This means that unlike strings, D-branes are non-perturbative objects in string theory.

Now consider the dynamics of a brane in flat space coupled to a gauge field A, with $B = 0$ and constant dilaton. To leading order in α', the DBI action looks like

$$S_{DBI} = -\left(2\pi\alpha\right)^2 \frac{T_p}{4} \int d^{p+1}\xi F_{ab} F^{ab}. \tag{2.7}$$

In the above expression, we have used the expansion $\det(1 + M) = 1 - \frac{1}{2}\mathrm{Tr}(M^2) + \ldots$. This looks exactly like the action of a $U(1)$ Yang-Mills theory with coupling constant

$$g_{YM}^2 = \left(T_p \left(2\pi\alpha\right)^2\right)^{-1} = (2\pi)^{p-2} g_s \alpha'^{(p-3)/2}. \tag{2.8}$$

This is a very useful relation that relates both sides of the correspondence.

The DBI action can be generalized to include couplings to other fields. In addition, Chern-Simons terms can be added to describe the theory at hand. The action (2.7) shows that open strings on a single brane are described by an Abelian $U(1)$ gauge theory. This can be generalized by considering a stack of N coincident Dp-branes. The strings now come with two extra indices that label the branes on which the strings begin and end. These indices are encoded in Chan-Paton factors that correspond to global symmetries of the worldsheet action and local symmetries of the target spacetime. The theory of oriented strings stretched between N coincident Dp-branes is described by a non-Abelian $U(N)$ gauge theory. The effective coupling constant for the field theory is given by g_sN. String perturbation theory is valid when the strings are weakly coupled, for $g_sN \ll 1$. This is the description "close to" the branes from the open string perspective; it makes contact with the string worldsheet. In the limit $g_sN \gg 1$, the theory is strongly coupled and we should look to the dual description for insight.

The limit $l_s \to 0$ must be taken such that it doesn't accidentally destroy any field theory quantities. Consider, for example, a probe brane at a position r away from a stack of N branes at $r = 0$. This breaks the gauge group from, for example, $U(N+1) \to U(N) \times U(1)$, and gives a Higgs expectation value U to a scalar field in the field theory proportional to

$$U = \frac{r}{\alpha'} = \frac{r}{\ell_s^2}. \tag{2.9}$$

For this to remain finite, we must define the decoupling limit as $l_s \to 0$ while keeping U fixed. U sets the energy scale of the field theory and r is the radial coordinate of the p-brane geometry. At large r, close to the boundary, the field theory is in the UV and at small r, in the narrow "throat" of 2.1, it is in the infrared. We can think of r or U as a holographic coordinate that connects (or separates) the bulk and boundary theories. In the next section, we will write the geometry in terms of U to more easily keep in contact with the dual field theory.

2.2 p-branes: A Gravitational Description

From the closed string perspective, the branes are massive, charged objects that source fields in type II string theory. This contains a graviton and a dilation, as well as one, two, and three-form fields. As we are taking the low energy limit $l_s \to 0$, we can again consider only the massless sector

of type IIA supergravity. The full conjecture of the gauge/gravity duality states that this should also hold at higher energies, when the supergravity is described by string theory. The bosonic part of the type IIA supergravity action is

$$S_{IIA} = \frac{1}{2\kappa_{10}^2}\int d^{10}x\sqrt{-g}\, e^{-2\Phi}\left(R + 4\partial_\mu\Phi\partial^\mu\Phi - \frac{1}{2}|H_3|^2\right) \\ - \frac{1}{4\kappa_{10}^2}\int d^{10}x\left(F_2\wedge\star F_2 + \widetilde{F}_4\wedge\star\widetilde{F}_4 + B_2\wedge F_4\wedge F_4\right) \tag{2.10}$$

where

$$F_p\wedge\star F_p = \sqrt{-g}|F_p|^2 = \tfrac{1}{p!}\sqrt{-g}F_{\mu_1\ldots\mu_p}F^{\mu_1\ldots\mu_p}, \tag{2.11}$$

and

$$F_2 = dA_1\,, \quad H_3 = dB_2\,, \quad F_4 = dA_3. \tag{2.12}$$

The theory has a dilaton field Φ, a metric tensor $g_{\mu\nu}$, and one, two, and three-form gauge field A_1, B_2, and A_3, respectively. It is useful to define the field strength $\widetilde{F}_4 = F_4 - A_1\wedge H_3$ to simplify notation. The factor of the dilaton in front of the Einstein-Hilbert term is a relic from the tree-level action computed in string perturbation theory, which comes with a factor of $1/g_s^2$. It is convenient move to the Einstein frame by setting

$$ds_E^2 = e^{-\frac{\Phi}{2}}ds_{string}^2 \tag{2.13}$$

$$g_{\mu\nu}^E \equiv \widetilde{g}_{\mu\nu} = e^{-\Phi/2}g_{\mu\nu}. \tag{2.14}$$

In this frame, the equations of motion take the canonical form

$$R_{\mu\nu} - \frac{1}{2}\widetilde{g}_{\mu\nu}R = 8\pi G_{10}T_{\mu\nu}. \tag{2.15}$$

$T_{\mu\nu}$ is the Stress-Energy tensor:

$$8\pi G_{10}T_{\mu\nu} = \frac{-2}{\sqrt{-\widetilde{g}}}\frac{\delta S_{matter}}{\delta\widetilde{g}^{\mu\nu}} = 4\nabla_\mu\Phi\nabla_\nu\Phi - 2\widetilde{g}_{\mu\nu}\left(\nabla\Phi\right)^2 - \frac{e^{-\Phi}}{4}\left(\widetilde{g}_{\mu\nu}|H_3|^2 - H_\mu{}^{\sigma\beta}H_{\nu\sigma\beta}\right) \\ - \frac{e^{3\Phi/2}}{2}\left(\frac{1}{2}\widetilde{g}_{\mu\nu}|F_2|^2 - F_\mu{}^\sigma F_{\nu\sigma}\right) - \frac{e^{\Phi/2}}{4}\left(\widetilde{g}_{\mu\nu}|\widetilde{F}_4|^2 - \widetilde{F}_\mu{}^{\sigma\beta\lambda}\widetilde{F}_{\nu\sigma\beta\lambda}\right). \tag{2.16}$$

The overall constant in the action is related to the ten dimensional Newton's constant by $2\kappa_{10}^2 = (2\pi)^7\ell_s^8 = 16\pi G_{10}$, with $\ell_s^2 = \alpha'$. By varying the action with respect to Φ, B_2, A_1, A_3, and $\widetilde{g}_{\mu\nu}$, respectively, we get the equations of motion:

$$\nabla^2\Phi - \frac{e^{-\Phi}}{2}|H_3|^2 - \frac{3e^{3\Phi/2}}{4}|F_2|^2 - \frac{e^{\Phi/2}}{4}|\widetilde{F}_4|^2 = 0 \tag{2.17}$$
$$d\left(e^{-\Phi}\star H_3\right) + d\left(e^{\Phi/2}A_1\wedge\star\widetilde{F}_4\right) - \frac{1}{2}F_4\wedge F_4 = 0$$
$$d(e^{3\Phi/2}\star F_2) - e^{\Phi/2}H_3\wedge\star\widetilde{F}_4 = 0$$
$$d\left(e^{\Phi/2}\star\widetilde{F}_4\right) + H_3\wedge F_4 = 0.$$

Non-trivial $p =$ even solutions of the supergravity equations of motion are called p-branes [13]. In the closed-string limit $g_sN \gg 1$, the stack of N Dp-branes causes the spacetime to backreact strongly, sourcing the p-brane geometry. This is the higher-dimensional analogue of the Reissner-Nordstrom black hole, and reflects the same mass and charge as N Dp-branes. Keeping only the background fields g and Φ as well as a gauge field A_{p+1} that naturally couples to a $p+1$ dimensional hypersurface, we can write the non-extremal p-brane geometry as

$$\frac{ds^2}{ls^2} = e^{-\Phi/2}\left\{h^{-\frac{1}{2}}(U)\left(-f(U)dt^2 + \sum_{i=1}^{p}dx_i^2\right) + h^{\frac{1}{2}}(U)\left[\frac{dU^2}{f(U)} + U^2d\Omega_{8-p}^2\right]\right\}\ , \tag{2.18}$$
$$e^{\Phi} = g_sl_s^{-3}h^{\frac{3-p}{4}}(U)\ , \qquad A_{p+1} = \frac{1}{g_s}\left[l_s^4h^{-1}(U) - 1\right]dx^0\wedge\cdots\wedge dx^p\ .$$

The form of the dilaton is $e^{\Phi_0+\Phi}$, where e^{Φ_0} is the constant, asymptotic value g_s. In the above,

$$h(U) = l_s^4\left(1 + \left(\frac{R}{l_s^2U}\right)^{7-p}\right)\ , \qquad f(U) = 1 - \left(\frac{U_0}{U}\right)^{7-p}. \tag{2.19}$$

R can be thought of as a fundamental scale depending on p and U_0 corresponds to the location of the p-brane horizon. The gauge/gravity duality tells us how to relate gravity parameters to those in the gauge theory. An expression for R can be found by computing the total charge for the N Dp-branes, each of which carries one unit of the $(p+1)$-form flux. The total charge is found by integrating the flux through the sphere at infinity. In the string frame, it is

$$Q = \frac{1}{16\pi G_{10}}\int_{S^{8-p}}\star F_{p+1} = N. \tag{2.20}$$

The field theory and supergravity parameters are related by

$$\left(\frac{R}{\ell_s}\right)^{7-p} = d_pg_sN\ , \qquad d_p = (4\pi)^{(5-p)/2}\Gamma\left(\frac{7-p}{2}\right)\ . \tag{2.21}$$

The supergravity solution is valid when the length scale R is large to avoid curvature corrections. This means that the closed string perspective is valid in the region $g_sN \gg 1$ and the corresponding

field theory is at large 't Hooft coupling. Note that taking R to be large is equivalent to setting $l_s \to 0$.

The form of h is restricted by the equations of motion to be a harmonic function. In the asymptotic region $r \gg R$, the metric approaches flat space, while $r \ll R$ corresponds to the near-horizon geometry. Figure 2.1 depicts closed string modes propogating in both the asymptotic and near-horizon regions. However, in the supergravity regime, in order to keep U fixed while taking the decoupling limit, r must be small. This has the benefit of keeping only the closed string modes that propogate deep in the bulk "throat".

In the decoupling or near-horizon limit, the function h becomes

$$h(U) = \frac{d_p g_s N}{l_s^{3-p} U^{7-p}}. \tag{2.22}$$

The extremal limit of (2.18) is achieved by setting $U_0 \to 0$. These are BPS states of type IIA supergravity as they preserve half of the background Poincare supercharges. The mass per unit volume of the p-brane obeys the inequality

$$M \geq \frac{N}{(2\pi)^p g_s l_s^{p+1}}. \tag{2.23}$$

The extremal geometry given above arises when this bound is saturated. When M is greater than this, we have a non-extremal black p-brane.

The geometry (2.18) with h given by (2.22) describes the near-horizon geometry of a black p-brane. This looks like a black hole in warped $AdS_{p+2} \times \mathcal{M}^{D-p-2}$, where $\mathcal{M}$ is a compact manifold and D is the space-time dimension. It is a smooth geometry deep in the p-brane "throat", as shown in figure 2.1. The radius of the throat is set by the length scale R or, equivalently, by the Dp-brane charge. The energy measured by an observer at infinity is redshifted by a factor of $\sqrt{-g_{tt}}$, which is infinite for $p < 7$ as $r \to 0$. In other words, the geometry produces an infinite gravitational well that decouples it from the asymptotic region. For $p = 3$, the extremal geometry is given by $AdS_5 \times S^5$ and the dual field theory is conformal, $\mathcal{N} = 4$ super Yang Mills in four dimensional Minkowski space. It was this canonical example that made the gauge/gravity duality famous, and the reason it is often called AdS/CFT.

Type IIA supergravity is a Kaluza-Klein reduction of 11D supergravity (SUGRA), which is the low energy description of M-theory. Given a solution of type IIA supergravity, we can construct a

solution of 11D SUGRA by

$$ds_{11}^2 = e^{-\frac{2}{3}\Phi} ds_{10}^2 + e^{\frac{4}{3}\Phi}(d\zeta + A_1)^2 \ , \qquad A_3 = A_3 + d\zeta \wedge B_2 \ . \tag{2.24}$$

For the extremal D0-brane solution we get

$$g_s^{2/3} ds_{11}^2 = -dt^2 + dr^2 + r^2 d\Omega_8^2 + g_s^2 d\zeta^2 + \left(\frac{R}{r}\right)^7 (g_s d\zeta - dt)^2 \, . \tag{2.25}$$

We will consider the D0-brane case later on in this thesis.

The 11D theory contains only a 3-form gauge field that couples to a 2-brane or, by way of the electric-magnetic duality, a 5-brane. These are known as M2 and M5 branes. A stack of N M2-branes in the large N limit sources the solution

$$\begin{aligned} \frac{ds^2}{l_s^{8/3}} &= h(U)^{-2/3} \eta_{\mu\nu} dx^\mu dx^\nu + h(U)^{1/3} \left(dU^2 + U^2 d\Omega_7^2\right) \\ A_3 &= l_s^4 h(U)^{-1} dx^0 \wedge dx^1 \wedge dx^2, \end{aligned} \tag{2.26}$$

where h is the harmonic function

$$h(U) = l_s^4 \left(1 + \frac{l^6}{l_s^{12} U^6}\right) \tag{2.27}$$

and the length scale $l^6 = 32\pi^2 N l_p^6$, where l_p is the planck length. We will consider the gauge/gravity duality applied to M2-branes later on in the thesis.

2.3 Bulk Observables

We can obtain thermodynamic quantities of the black p-brane by looking at its near-horizon geometry, $U \approx U_0$. [4, 17] A black hole is said to be in thermal equilibrium with a heat bath of temperature T. This temperature is fixed by the size of the thermal circle at infinity by periodically identifying the time coordinate in the Euclidean path integral. To calculate the Hawking temperature, we first Wick rotate to Euclidean time $\tau = it$:

$$\Delta\tau = \beta = T^{-1}. \tag{2.28}$$

The circle must close off smoothly to ensure regularity at the horizon. Around $U = U_0$, $f(U) \approx f'(U)|_{U=U_0} (U - U_0)$ and $h(U) \approx h(U_0)$. The metric looks like

$$\frac{ds^2}{l_s^2} = \Omega \left\{ \frac{\sqrt{h(U_0)}}{(U - U_0)\ f'(U)|_{U=U_0}} \left((U - U_0)^2 \frac{f'(U)|_{U=U_0}}{h(U_0)} d\tau^2 + dU^2 \right) + \dots \right\}, \tag{2.29}$$

where Ω is an overal conformal factor that comes from being in the Einstein frame and the ... lead to the remaining regular terms. This looks like polar coordinates $d\mathcal{R}^2 + \mathcal{R}^2 d\phi^2$ under the identification

$$\mathcal{R} = 2\sqrt{(U-U_0)\frac{h(U_0)^{1/2}}{f'(U)|_{U=U_0}}}, \qquad \phi = \frac{f'(U)|_{U=U_0}}{2\sqrt{h(U_0)}}. \tag{2.30}$$

The coordinate ϕ has periodicity 2π to ensure the absence of a conincal deficit. This gives us the period of the circle of compactification for τ

$$\beta = d\tau = 4\pi h^{1/2}\frac{2}{f'(U)|_{U=U_0}} \tag{2.31}$$

and the temperature

$$T = \frac{1}{\beta} = \frac{2^{(p-9)/2}(p-7)l_s^{(p-3)/2}\pi^{(p-9)/4}U_0^{(p-5)/2}}{\sqrt{g_s N\,\Gamma\left((7-p)/2\right)}}. \tag{2.32}$$

The Bekenstein-Hawking entropy is proportional to the area of its event horizon in the Einstein frame:

$$\begin{aligned} S = \frac{A}{4G_{10}} &= \frac{1}{4G_{10}}\int \sqrt{-\widetilde{g}_{U=U_0}}\,[dx_1\ldots dx_p d\theta_1\ldots d\theta_{8-p}] \\ &= \frac{2^{(p-1)/2}g_s^{3/2}l_s^{-(p+3)/2}\pi^{3(p-7)/4}U_0^{(9-p)/2}\sqrt{N\,\Gamma\left((p-7)/2\right)}}{\Gamma\left(5-p\right)}. \end{aligned} \tag{2.33}$$

We will use this value of the black hole entropy to determine the free energy of the corresponding gauge theory.

2.4 Boundary Observables

By the gauge/gravity dictionary, each field in the bulk corresponds to a gauge-invariant single-trace operator on the boundary. For example, bulk gauge fields are dual to boundary symmetry currents. These fields transform in the same representation of the gauge group that governs the boundary theory. Consider the dimensional reduction of type IIA string theory to $AdS_{p+2}\times\mathcal{M}^{8-p}$. The type IIA fields can be expanded in a complete set of "spherical" harmonics on the compact space, forming Kaluza-Klein towers on the internal space $\mathcal{M}^{8-p}$. For example, the Kaluza-Klein expansion of a field ϕ on $AdS_5\times S^5$ looks like

$$\phi(x_i,\Omega_5) = \sum_{l=0}^{\infty}\phi^l(x_i)Y^l(\Omega_5), \tag{2.34}$$

where the x_i are the coordinates on AdS_5 and Y^l are the spherical harmonics. The supergravity equations of motion determine the masses and couplings of the fields on AdS_p. These are fields of scalar, vector, and tensor type that are related with single-trace scalar, vector, and tensor operators in the dual large N field theory. In this section, we flesh out some of the tools necessary from the gravity point of view to make contact with field theory observables.

Consider as an example a scalar field ϕ with mass m dual to a primary operator. The holographic dictionary gives the relation

$$m^2 l^2 = \Delta(\Delta - d), \tag{2.35}$$

where l is the AdS scale, Δ is the mass dimension of the scalar primary operator, and d is the dimension of the boundary theory. Its motion is governed by the Klein-Gordon equation

$$(\nabla^2 - m^2)\phi = 0, \tag{2.36}$$

where the covariant derivative is computed with respect to the AdS metric. In Poincare coordinates, this is

$$ds^2 = \frac{l^2}{z^2}\left(dz^2 + \eta_{\mu\nu}dx^\mu dx^\nu\right). \tag{2.37}$$

The AdS boundary is located at $z = 0$. Decomposing the field into Fourier modes in the x^μ directions and considering a plane wave ansatz of the form

$$\phi(z, x) = e^{ip^\mu x_\mu}\phi_p(z), \tag{2.38}$$

(2.36) reduces to an equation with two independent solutions characterized by the asymptotics of ϕ.

$$\phi_p(z \to 0) \sim z^{\Delta_\pm}, \tag{2.39}$$

where $\Delta_\pm$ are the roots of (2.35), which gives $\Delta_+ > \Delta_-$ and $\Delta_- = d - \Delta_+$. Let us define $\Delta_+ \equiv \Delta$. The behavior of ϕ as $z \to 0$ is

$$\phi(z, x) \sim \phi_0 z^{d-\Delta} + \phi_+ z^\Delta + \dots \tag{2.40}$$

In the above expression, the mode ϕ_0 looks like a source and ϕ_+ like a response. In fact, ϕ_0 sources an operator with dimension Δ in the dual field theory, which incurs a vacuum expectation value ϕ_+ as a result. The modes ϕ_+ and ϕ_0 are called normalizable and non-normalizable, respectively. In general, a field theory is constructed out of a set of normalizable and non-normalizable modes which are solutions to the equations of motion, as we have seen in this example. The normalizable modes

propagate in the bulk and represent physical states of the dual field theory, or equivalently of string theory in AdS. Actions evaluated on normalizable solutions remain finite. The non-normalizable modes are field configurations that encode operator insertions in the boundary field theory. Non-normalizable modes are non-fluctuating, and violently perturb the asymptotic geometry. These sources can couple to relevant, marginal, or irrelevant operators in the dual field theory. Irrelevant operators change the theory in the UV, so the corresponding contribution to the action is infinite. In this thesis, we consider only relevant operator insertions that preserve the asymptotics of the gravity theory. Later on, we will turn on such non-normalizable modes to find supergravity solutions dual to a deformed boundary gauge theory.

In general, the partition function

$$Z\left[\phi_0^i\right] = e^{-W\left[\phi_0^i\right]} = \left\langle T e^{-\int d^d x \phi_0^i(x) \mathcal{O}(x)_i} \right\rangle \tag{2.41}$$

relates the state of the bulk fields to a correlation function of boundary operators that depends on the boundary value ϕ_0^i of the bulk field ϕ^i. This can be treated semi-classically in the large N limit, in which case the generating functional W is just the supergravity action evaluated on the asymptotic value of the field $\phi(z,x)^i$. From the generating functional, we can calculate correlation functions of composite gauge-invariant operators holographically, by taking derivatives with respect to the sources

$$\langle \mathcal{O}_1(x_1) \dots \mathcal{O}_n(x_n) \rangle = (-1)^n \left. \frac{\delta^n W}{\delta\phi_0^1(x_1) \dots \delta\phi_0^n(x_n)} \right|_{\phi_0=0}. \tag{2.42}$$

The general prescription is as follows. First, write down a supergravity action that encodes all of the bulk fields dual to the operators of the boundary theory reduced over the compact space. Then solve the corresponding equations of motion subject to the boundary conditions of the bulk fields, defined in the UV. Finally, take derivatives of the on-shell action to get correlation functions of the field theory.

We must also account for divergent terms in the on-shell action for these correlation functions to be finite. In what follows, we sketch a methods for canceling divergences and computing the energy of the boundary QFT known as holographic renormalization [18, 19]. The cancellation of divergences will be important for our calculation of the boundary stress tensor, so we will use the metric as an example. However, the same logic holds for other fields. The Euclidean gravity action in AdS_{d+1} is

$$S = \frac{1}{16\pi G_{d+1}} \int d^{d+1}x \sqrt{g} \left(R + \frac{d(d-1)}{l^2} \right) + \frac{1}{8\pi G_{d+1}} \int d^d x \sqrt{\gamma} K. \tag{2.43}$$

The second term is the Gibbons-Hawking boundary term, which is a remnant of the equations of motion. K and γ are the extrinsic curvature and induced metric on the boundary. We impose that the metric is asymptotically AdS. Because of this, the action diverges due to a cosmological constant term which is proportional to the volume of spacetime. It is convenient to move to Fefferman-Graham coordinates, where the metric takes the form

$$ds^2 = l^2 \left(\frac{d\rho^2}{4\rho^2} + \frac{1}{\rho} g_{\mu\nu}(\rho, x) dx^\mu dx^\nu \right). \tag{2.44}$$

Solutions to the Einstein equations admit an expansion of the form

$$g_{\mu\nu}(\rho, x) = g^{(0)}_{\mu\nu}(x) + \rho^{1/2} g^{(1)}_{\mu\nu}(x) + \rho g^{(2)}_{\mu\nu}(x) + \cdots + \rho^{d/2} \ln \rho h^{(d)}_{\mu\nu}(x) + \ldots. \tag{2.45}$$

The coefficients $g^{(i)}$ depend only on x. In general, some will be fixed by solving the equations of motion order by order at the boundary and others will be left free. These are normalizable modes, and involve derivatives of the full bulk solution evaluated at the boundary. In the pure gravity example, the coefficients multiplying half-integer powers of ρ can be shown to vanish. In the $d = 3$ cases we will consider in this thesis, the log terms are non-vanishing but do not lead to a conformal anomaly.

To regularize the action, we introduce a cut-off $\epsilon > 0$ and integrate ρ up to that cut-off. Inputting the above expansion into the action gives

$$S = \frac{1}{16\pi G_{d+1}} \int d^{d+1}x \sqrt{g^{(0)}} \left(\epsilon^{-d/2} a_{(0)} + \epsilon^{-d/2+1} a_{(2)} + \cdots - \log \epsilon a_{(d)} \right) + S_{finite}, \tag{2.46}$$

where S_{finite} encodes all terms that don't diverge as $\epsilon \to 0$. The coefficients $a_{(i)}$ to fourth order are

$$\begin{aligned} a_{(0)} &= \frac{2}{l}(d-1), \qquad a_{(2)} = \frac{lR}{2(d-1)}, \\ a_{(4)} &= \frac{l^3}{2(d-2)^2} \left(R^{\mu\nu} R_{\mu\nu} - \frac{1}{d-1} R^2 \right). \end{aligned} \tag{2.47}$$

The simplest way to remove divergences that arise from these coefficients is by counter term subtraction. From the renormalized action $S_{ren} = S - S_{CT}$, we can then derive the expectation value of the stress tensor from the on-shell action from (2.42). It is

$$\langle T_{\mu\nu} \rangle = \frac{2}{\sqrt{g_0)}} \frac{\delta S_{ren}}{\delta g^{\mu\nu}_{(0)}} = \lim_{\epsilon \to 0} \left(\frac{l^{d-2}}{\epsilon^{d/2-1}} T_{\mu\nu}(\gamma) \right), \tag{2.48}$$

where γ is the induced metric at the cut-off.

The counter terms required to cancel the divergences that arise from each coefficient depends on the dimension. For the four-dimensional asymptotically AdS space times we will consider in this thesis, the $a_{(4)}$ term vanishes. The others can be canceled by adding counter terms of the form [20, 21]

$$S_{CT} = -\frac{1}{8\pi G_4}\int_{\partial M} d^3x\sqrt{\gamma}\left(1-\frac{l^2}{12}R\right), \tag{2.49}$$

where R is the three-dimensional Ricci tensor. The corresponding boundary stress tensor is

$$T_{\mu\nu}(\gamma) = \frac{1}{8\pi G_{(4)}}\left(K_{\mu\nu} - K\,\gamma_{\mu\nu} + G_{\mu\nu} - 2\gamma_{\mu\nu}\right). \tag{2.50}$$

The first two terms are the extrinsic curvature and its trace, respectively, and come from the Gibbons-Hawking-York boundary term in the on-shell action. The last two terms are from the counter term contribution, with $G_{\mu\nu}$ the Einstein tensor of the induced metric. Integrating this solution over the sphere at infinity gives an expression for the energy that we will compute later.

Counter terms such as the ones computed above are known for certain geometries such as asymptotically AdS in $d+1 \leq 5$ [20], but in general are difficult to find. In particular, there is no known extension of holographic renormalization for asymptotically flat space times that only involve local counterterms.

2.5 Smarr formulae

Smarr formulae are particularly important in situations in which the solution is presented numerically. For every Killing vector v of our numerical solutions, we can define an antisymmetric tensor whose conservation follows from the equations of motion and the fact that the metric and matter fields are invariant under the symmetries generated by v. In other words

$$\mathcal{L}_v g = \mathcal{L}_v C = 0\ , \tag{2.51}$$

where C is a matter field of arbitrary rank and g is the metric tensor. Conservation also follows from the identity

$$\nabla_b\nabla^b v_a = -R_{ab}v^b\ . \tag{2.52}$$

In the language of differential forms, this means that for a spacetime dimension $d+1$ we have a closed $(d-1)$-form

$$d\left(\star K_v\right) = 0\,, \tag{2.53}$$

where

$$K_v = \frac{1}{2}(K_v)_{ab}\, dx^a \wedge dx^b \ . \tag{2.54}$$

Integrating $d(\star K_v)$ over a d-dimensional surface Σ_{12} of constant time with $y_1 < y < y_2$, where y is the radial coordinate from the horizon at $y = 0$ to $y = \infty$, we conclude that

$$0 = \int_{\Sigma_{12}} d \star K_v = \int_{\partial\Sigma_{12}} \star K_v = \int_{\Gamma(y_2)} \star K_v - \int_{\Gamma(y_1)} \star K_v \ , \tag{2.55}$$

where we used the fact that the boundary of Σ_{12} has two disjoint components $\Gamma(y_2)$ and $\Gamma(y_1)$ (with opposite orientations). This is known as a Komar integral, and shows that the integral

$$I_v(y) = \int_{\Gamma(y)} \star K_v \, , \tag{2.56}$$

over the closed surface of constant time and radial coordinate y is independent of y. The Smarr formula is obtained by equating the integral over the horizon $I_v(0)$ to the integral at infinity $I_v(\infty)$. In this way, it relates observables at the horizon to those at infinity. Checking the identity (2.55) will prove a powerful test of our numerical solutions.

For pure Einstein gravity, the Komar integrand is $R^a_b v^b$, which vanishes by the equations of motion. The analysis for asymptotically AdS geometries is more involved than for the asymptotically flat case because of the cosmological constant [10]. It was shown that for $2k$-derivative terms in the lagrangian, a Komar boundary term with $2k-1$ derivatives is needed. Since the cosmological constant term has zero derivatives, we need to find a -1-derivative term to derive an appropriate Smarr relation.

For a general killing vector v, $\nabla_a v^a = 0$ and we can define at least locally a two-form ω such that $v^b = \nabla_a \omega^{ab}$. Inverting this equation, it is simple to see that ω can be written as

$$\omega^{ab} = \frac{2}{\sqrt{g}} \int \sqrt{g}\, dx^{[a} v^{b]} \, , \tag{2.57}$$

which is an integral, or -1-derivative term in some sense. The ω term is necessary in AdS to cancel divergences that arise from the cosmological constant term in the action. The conserved two-form for pure AdS gravity is

$$(K_v)^{ab} = \nabla^a v^b + \frac{2\Lambda}{d-2}\omega^{ab}. \tag{2.58}$$

This result will be generalized later in the thesis to include fields coupled to gravity that come about through the equations of motion.

Chapter 3

Numerical Techniques

Solving the equations of motion for geometries without spherical symmetry generally requires the use of numerical methods. In this section we give a summary of these methods as they apply to our work. Unless otherwise stated, all of our work is coded in Mathematica and can be run in a reasonable amount of time on a laptop computer.

3.1 Generalized Harmonic Einstein Equations

In what follows, we will follow the logic and prescription first conceived in [22, 23] and reviewed in [24] to see that the Einstein equations can be recast in an elliptic form. Consider for simplicity the vacuum Einstein equations

$$R_{\mu\nu} = 0. \tag{3.1}$$

The same prescription will hold for geometries coupled to matter. This is a system of second-order PDE's where the metric components are the functions for which we want to solve. They are hyperbolic equations, and on small scales, solutions to these equations propagate dynamically along a lightcone like a wave. The problem can only be formulated as an initial value problem where we must specify the behavior of the initial data on a past lightcone or Cauchy surface. For the static, Euclidean geometries we will consider in this thesis, the Einstein equation becomes weakly elliptic. It can now be formulated as a boundary value problem, but it retains the gauge invariance that

leads to a loss of numerical control. To see this, consider linear perturbations $h_{\mu\nu}$ of the form

$$g_{\mu\nu} \to g_{\mu\nu} + h_{\mu\nu}. \tag{3.2}$$

The principle part of the operator acting on such perturbations is dominated by their very short wavelength behavior and describes the character of (3.1) around the background $g_{\mu\nu}$. Locally, this is the second-order term

$$P_g h_{\mu\nu} = \frac{1}{2} g^{\alpha\beta} \left(\partial_\mu \partial_\alpha h_{\beta\nu} + \partial_\nu \partial_\alpha h_{\beta\mu} - \partial_\alpha \partial_\beta h_{\mu\nu} - \partial_\mu \partial_\nu h_{\alpha\beta} \right). \tag{3.3}$$

A Partial Differential Equation is elliptic around some background if short wavelength perturbations do not, at any point, propagate like a wave. This is equivalent to saying that equation (3.3) is nonzero everywhere for a general solution

$$h_{\mu\nu} = a_{\mu\nu} e^{i k_\alpha x^\alpha} \tag{3.4}$$

for some choice of constants $a_{\mu\nu}$ and non-zero $k_\mu \in \mathbb{R}$. However, we can also write h as an infinitesimal diffeomorphism generated by a vector field ξ, which gives:

$$h_{\mu\nu} = \nabla_{(\mu} \xi_{\nu)} \tag{3.5}$$

$$P_g h_{\mu\nu} = 0. \tag{3.6}$$

This pure gauge term is annihilated by the principle part. Thus our equations (3.1) are not elliptic as a consequence of their diffeomorphism invariance. As a result, the boundary conditions do not specify a unique solution but only fix its diffeomorphism class. By choosing appropriate boundary conditions, the diffeomorphism class of the solution can be fixed, but this is not enough to exactly specify the solution and ensure we numerically evolve to the one we want, as a pure gauge perturbation 3.5 can always be added to the physical solution 3.4 without contributing to the principal part. As we search for a numerical solution using a relaxation method, short-wavelength, pure-gauge modes remain present. As it attempts to converge, small errors from the gauge modes will build up until we can no longer trust the solution. To prevent this from happening, we need to prevent pure gauge fluctuations from becoming important by fixing the gauge.

Instead of the vacuum Einstein equations, consider the harmonic Einstein equations, also known as the Einstein-deTurck equations:

$$R^H_{\mu\nu} = R_{\mu\nu} - \nabla_{(\mu} \xi_{\nu)} = 0 \tag{3.7}$$

$$\xi^\lambda \equiv g^{\mu\nu} \left(\Gamma^\lambda_{\mu\nu} - \overline{\Gamma}^\lambda_{\mu\nu} \right). \tag{3.8}$$

The approach was first introduced in [23] and studied in great detail in [25]. Its generalization to finding stationary solutions of the form discussed in this manuscript was first detailed in [26]. In (3.8), Γ is the Levi-Civita connection of the ansatz metric $g_{\mu\nu}$ and $\overline{\Gamma}$ is a "reference connection" that has the same asymptotics and symmetries as the solutions we want to find. This amounts to matching the boundary conditions of the metrics g and $\overline{g}$. The gauge fixing term (3.5) in (3.7) puts the short wavelength behavior of the physical and pure gauge modes on equal footing. Then, fixing ξ projects out the pure gauge modes. The principle part of (3.7) is

$$P_g h_{\mu\nu} = -\frac{1}{2}\partial_\alpha \partial^\alpha h_{\mu\nu}. \tag{3.9}$$

Note this this way to fix the gauge is a covariant formulation of the Harmonic gauge, as it involves the difference of two reference connections. The above prescription is the same if matter fields are present. For a general theory of gravity coupled to matter, the equations are

$$\begin{aligned} \widetilde{E}_{\mu\nu} &= E_{\mu\nu} - \nabla_{(\mu}\xi_{\nu)} = 0\,, \\ E_{\mu\nu} &= R_{\mu\nu} - T_{\mu\nu}. \end{aligned} \tag{3.10}$$

For the codimension two geometries we will consider, $\widetilde{E}_{\mu\nu}$ can be recast into the form

$$\gamma^{\mu\nu}\partial_\mu\partial_\nu Q_i + F_i(\partial_\alpha Q_k, Q_k) = 0, \tag{3.11}$$

where Q_i represent the field content of the theory and F_i is a complicated function of the metric and matter fields and their first derivatives, and $\gamma^{\mu\nu}$ is a two-dimensional positive-definite matrix. This means that, under the appropriate boundary conditions, $\widetilde{E}_{\mu\nu}$ forms a system of elliptic partial differential equations.

The gauge-fixed equations are elliptic for a Riemannian background g, but to ensure that solutions to (3.7) are also solutions of $E_{\mu\nu} = 0$, we must check a posteriori that $\xi = 0$. A solution to (3.7) with non-vanishing ξ is called a Ricci soliton, and proper boundary conditions are important for avoiding them. [1]

It is clear that any solution to $\widetilde{E}_{ab} = 0$ with $\xi = 0$ is a solution to $E_{ab} = 0$, however, the converse is not necessarily true. It is therefore important to check a posteriori that the condition $\xi = 0$ is satisfied. Under some special circumstances, and for certain types of matter fields, one can show

[1] The above analysis holds for Euclidean geometries like the ones we will be considering. For Lorentzian geometries the equations are hyperbolic, and while the above prescription could work in this case, the solutions are not necessarily locally unique, and more care must be taken to distinguish Ricci solitons from Ricci flat solutions.

that Ricci solitons cannot exist [25]. However, the cases under consideration are not under this special class. Fortunately, since the system of partial differential equations $\widetilde{E}_{ab} = 0$ is Elliptic, it can be solved as a boundary value problem for well-posed boundary conditions and the solutions should be locally unique. This means that an Einstein solution cannot be arbitrarily close to a soliton solution and one should easily be able to distinguish the Einstein solutions of interest from solitons by monitoring ξ. In the rest of the thesis, we will solve the Harmonic Einstein equation using the numerical techniques developed in the next section.

3.2 Spectral Methods

There are many ways to solve a differential equation numerically. All require a choice of grid and a way to define derivatives discretely. With spectral methods, derivatives are estimated using a polynomial approximation that includes all points on the grid. These derivatives act as a matrix on the functions for which we want to solve, turning a boundary value problem into an linear problem. It hinges on the assumption that we can expand the solution in an finite sum of basis functions called interpolating functions. For $(N+1)$ points, the interpolating function is a polynomial of degree $(N+1)$ which relaxes to the solution at each point and after each iteration. The first step in implementing these methods is to define a derivative operator. It can be shown that for non-periodic domains, using a non-uniform array of points greatly improves the rate of convergence to a solution. This is because a uniform grid can exhibit a Runge phenomenon, or large extrema near the boundary points, which get worse by a factor of 2^{N+1}.

To combat this issue, we choose a grid distribution with a greater density of points near the boundaries. The simplest example defines the Chebyshev points [27]. For a grid with minimum a and maximum b, they are given by

$$r_j = \frac{a+b}{2} - \frac{a-b}{2}\cos\frac{\pi j}{N} \;\; ; \; j = \{0, ..., N\}\,. \tag{3.12}$$

Figure 3.1 shows the interpolation of a test function $f(x) = x/(1+10x^2)$ on equidistant and Chebyshev grids, respectively. The blue curve interpolating on the uniform grid has obvious Runge phenomena near the endpoints, while the yellow curve, interpolating on the Chebyshev grid, approximates the solution everywhere. In addition, deviations of the polynomial interpolant on a Chebyshev grid decreases with the number of gridpoints like 2^{-N}.

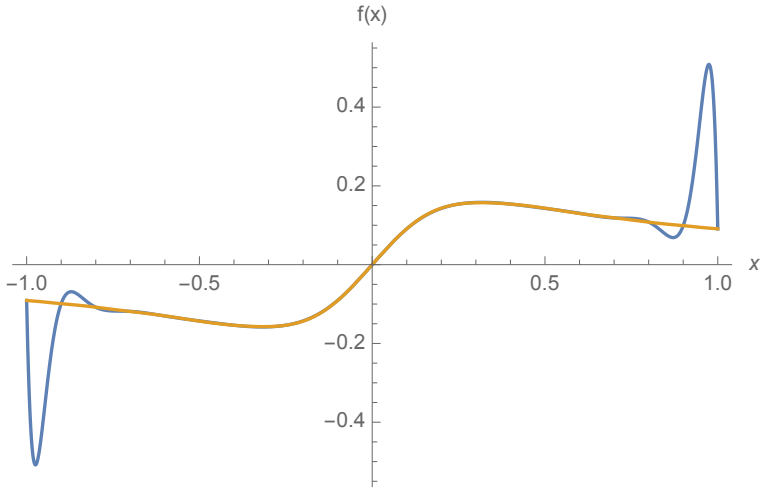

Figure 3.1: Interpolation of the test function $f(x) = x/(1 + 10x^2)$ on a uniform grid (blue curve) and Chebyshev grid (yellow curve) for $n = 10$ points. The uniform interpolation exhibits Runge phenomena.

The Cheybshev points are the stereographic projection of a uniformly spaced grid on a circular arc onto a line, as depicted in figure (3.2). The polynomial interpolant is

$$p_N(r) = \sum_{j=0}^{N} l_j(r) q_j, \tag{3.13}$$

$$l_j(r) = \prod_{p=0, p\neq j}^{N} \frac{r - r_p}{r_j - r_p}. \tag{3.14}$$

A solution found using spectral methods on a Chebyshev domain converges exponentially with N

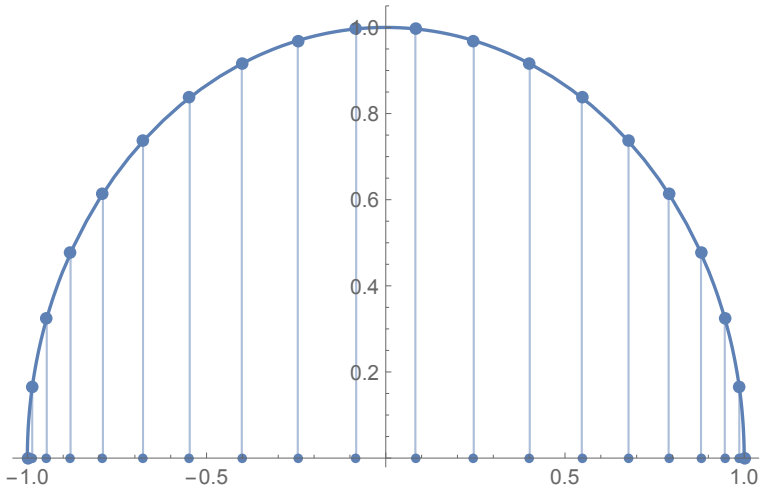

Figure 3.2: The Chebyshev points.

to a solution q. Differentiating the above polynomial p_N is the same as acting with the derivative of l_j on q_j. This is the differentiation operator in one dimension:

$$(D_N)_{ki} = l_i'(r_k), \tag{3.15}$$

where the prime denotes a derivative with respect to r and (D_N) is an $N+1$ dimensional square matrix. The operator for the n-th derivative can be easily obtained by computing the inner product of n copies of D_N. The problems we will be considering are codimension two, and our solutions will be functions of a radial coordinate r and an angular coordinate θ. We have the freedom, through a change of coordinates, to express θ in terms of a new coordinate x bounded on a domain from 0 to 1 and discretize the grid (r, x) using chebyshev interpolation in both directions. This has the advantage of removing trigonometric functions from the equations of motion which can in some cases be much simpler to solve. However, we may also use the periodicity of the ansatz functions to expand them in a Fourier basis in the θ direction. This can also be expressed as a change of coordinates from the Chebyshev points and also leads to exponential converges for periodic domains. For a 2π-periodic function, the grid points are evenly spaced on the domain $(0, 2\pi)$ and the interpolant is derived using the periodic sinc function [27]

$$l_j(\theta) = \frac{\sin\left(\frac{N+1}{2}(\theta - \theta_j)\right)}{(N+1)\tan\left(\frac{\theta-\theta_j}{2}\right)} \tag{3.16}$$

for $N+1$ even. The n'th-order derivative matrices are then constructed by differentiating the above function n times as written above.

We can generalize this result to act on a function of two variables by treating the two directions as independent $N+1$ dimensional grids. This forms a tensor product space, and we can use the denominated Kronecker product to compute the derivative operators for respective directions r and θ. They are

$$\begin{aligned} D^\theta &= I_{N+1} \otimes D^\theta_{N,} \\ D^r &= D^r_N \otimes I_{N+1}, \\ D^{r,\theta} &= D^r_N \otimes D^\theta_N. \end{aligned} \tag{3.17}$$

The same can be done to construct the second derivatives over the full domain. We will use these derivative operators to discretize our equations of motion. The solution q is then a vector of length $(N+1)^2$, one point for each of the values at (r, θ). We implement a Newton's method scheme

as follows. First, we discretize our second-order differential equations $E_i[q_i] = 0$ by replacing all functions by $(N+1)^2$-dimensional vectors and all derivatives by the matrices defined above. We begin with a smart choice of q_i and Taylor expand our equation around that choice.

$$E_i(q_j + \delta q_j) \approx E_i(q_j) + M_{ij}\delta q_j \tag{3.18}$$

$$M_{ij} = \frac{\partial E_i}{\partial q_j} + \frac{\partial E_i}{\partial(\partial_r q_k)} D^r_{kj} + \frac{\partial E_i}{\partial(\partial_\theta q_k)} D^\theta_{kj} + ... \tag{3.19}$$

Solving the equations of motion amounts to solving the linear equation (3.18), which gives us a solution δq_j to the above expansion. We then set

$$q_j \to q_j + \delta q_j \tag{3.20}$$

and continue this process until δq_j converges to 0 with the desired accuracy.

3.2.1 Boundary Conditions

In the polarised black hole and ABJM sections that follow, we will use the symmetries of our grid to force the symmetry properties of the solution at the axes of symmetry instead of imposing boundary conditions at these points. Consider a radial coordinate $r \in [0, 1]$. The horizon at $r = 0$ is an axis of symmetry; it is the origin of the Euclidean thermal circle. Since it is not an actual boundary, instead of imposing a condition on a solution to the equations of motion at the point $r = 0$, we want to say that the function is a smooth function of r^2. Instead of the interval $[0, 1]$, we choose the interval $[-1, 1]$ with the point $r = 0$ excluded. We then derive the differentiation matrices (3.15) on the doubled domain. Schematically, this looks like

$$\partial_r q = \begin{bmatrix} D_{11} & D_{12} \\ D_{21} & D_{22} \end{bmatrix} \begin{bmatrix} q_1 \\ q_2 \end{bmatrix}, \tag{3.21}$$

where q_1 and q_2 are the functions over $[-1, 0)$ and $[1, 0)$, respectively, and D_{ij} are block matrices. Since the function obeys the symmetry $r \to -r$, $q_1 = q_2$, and the doubled matrix can be truncated such that

$$D^r_N = D_{21} + D_{22}. \tag{3.22}$$

This acts only on functions of r^2 over the domain $(0, 1]$ to save on computational time and memory. A similar procedure can be carried out in the Fourier direction. First, we define a $4(N+1)\times 4(N+1)$ differentiation matrix on the domain $(0, 2\pi)$ in order to end up with a differentiation matrix that

acts on $(0, \pi/2)$. In this case, the solutions to the equations of motion behave differently at the axes of symmetry $\theta = 0, \pi/2$. For example, the diagonal metric components are symmetric about both of these points, but the off-diagonal component is antisymmetric about $\theta = \pi/2$. We must define different differentiation matrices D_N^θ to reflect these differences. We can write this as

$$\partial_\theta q = \begin{bmatrix} D_{11} & D_{12} & D_{13} & D_{14} \\ D_{21} & D_{22} & D_{23} & D_{24} \\ D_{31} & D_{32} & D_{33} & D_{34} \\ D_{41} & D_{42} & D_{43} & D_{44} \end{bmatrix} \begin{bmatrix} q_1 \\ q_2 \\ q_3 \\ q_4. \end{bmatrix}. \tag{3.23}$$

Consider the case of the diagonal metric component described above. Let us define the subdomains S_i of the q_i as follows

$$S_1 = (0, \pi/2)\,, \quad S_2 = (\pi, \pi/2)\,, \quad S_3 = (\pi, 3\pi/2)\,, \quad S_4 = (2\pi, 3\pi/2)\,. \tag{3.24}$$

With the full differentiation matrix defined on the domain ordered like this, the q_i with these symmetries are all equal. The truncated differentiation matrix on the domain of interest $(0, \pi/2)$ is then

$$D_N^\theta = D_{11} + D_{12} + D_{13} + D_{14}. \tag{3.25}$$

In the rest of the thesis, we will discretize the Einstein-deTurck equations on these domains and solve them using the spectral methods outlined in this chapter.

Chapter 4

Polarized Black Hole in AdS

What happens if we place a neutral black hole in a background electric field? Intuitively, one expects that the BH should polarize and deform in response to the applied electric field. We will show that this intuition is indeed correct but, in order to be rigorous, we first need to understand what it means to apply an electric field in general relativity. In this chapter, we will restrict ourselves to four-dimensional spacetimes.

4.1 Introduction

Let us start by considering classical solutions of Einstein-Maxwell theory

$$R_{\mu\nu} = 2F_{\mu\alpha}F_{\nu}{}^{\alpha} - \frac{1}{2}g_{\mu\nu}F_{\alpha\beta}F^{\alpha\beta}\,, \qquad \nabla_{\mu}F^{\mu\nu} = 0\,, \tag{4.1}$$

with $F = d\mathcal{A}$. This is the minimal theory that can contain polarised black holes. Remarkably, 40 years ago Ernst [28] constructed the following exact solution

$$ds^2 = \lambda^2(y,\theta)\left[-\left(1-\frac{y_0}{y}\right)dt^2 + \frac{dy^2}{1-\frac{y_0}{y}} + y^2 d\theta^2\right] + \frac{y^2\sin^2\theta d\phi^2}{\lambda^2(y,\theta)}\,, \qquad \mathcal{A} = \mathcal{E}(y_0 - y)\cos\theta dt\,, \tag{4.2}$$

where $\lambda(y,\theta) = 1 + (\mathcal{E}/2)^2 y^2\sin^2\theta$. The parameter y_0 is the areal radius of the black hole and $\mathcal{E}$ parameterizes the background electric field. In the absence of the black hole ($y_0 = 0$) and to linear order in $\mathcal{E}$ the solution describes flat spacetime with a constant electric field along $z = y\cos\theta$.

This solution realizes the intuition of black hole polarization and deformation. The charge

density on the horizon (or electric flux) is given by

$$\frac{dQ}{d\Omega} = \frac{1}{4\pi} \frac{2y_0\gamma\cos\theta}{\left(1+\gamma^2\sin^2\theta\right)^2}\,, \qquad \gamma = \frac{\mathcal{E}y_0}{2}\,. \tag{4.3}$$

As expected, the electric field $\mathcal{E}$ induces a positive charge density in the upper hemisphere $0 \leq \theta < \frac{\pi}{2}$ and a negative charge density in the lower hemisphere $\frac{\pi}{2} < \theta \leq \pi$. The horizon also gets deformed. The equatorial perimeter shrinks to $2\pi y_0/(1+\gamma^2)$ while the length of a meridian expands to $\pi y_0\left(1+\gamma^2/2\right)$. While our intuition works at small distances, the backreaction of the electric field drastically changes the geometry far from the black hole. To see that consider the length of an equatorial circle ($\theta = \pi/2$) as a function of the coordinate y in the solution without black hole ($y_0 = 0$). This length increases from zero at $y = 0$ until it reaches a maximum at $y = 2/\mathcal{E}$, and then decreases towards zero as $y \to \infty$. This shows that our original picture of a black hole placed in an approximately flat spacetime with a background electric field is only realized for $y_0 \ll 2/\mathcal{E}$ or $\gamma \ll 1$. For strong electric fields, i.e. $\gamma \gg 1$, the Ernst solution describes different physics.

In this thesis we study polarised black holes in Anti-de Sitter (AdS) spacetime. One motivation is the study of neutral black hole polarization in a context where the asymptotic geometry of spacetime is not destroyed by the presence of a background electric field. Another motivation is the study of conformal theories subject to an external electric field. We consider the action

$$S = \frac{1}{16\pi G_N}\int d^4x\sqrt{-g}\left(R + \frac{6}{l^2} - F_{\alpha\beta}F^{\alpha\beta}\right) + \frac{1}{8\pi G_N}\int d^3x\sqrt{h}K \tag{4.4}$$

where l is the AdS length scale and we also added the Gibbons-Hawking-York boundary term. The field equations are

$$R_{\mu\nu} + \frac{3}{l^2}\,g_{\mu\nu} = 2F_{\mu\alpha}F_{\nu}{}^{\alpha} - \frac{1}{2}g_{\mu\nu}F_{\alpha\beta}F^{\alpha\beta}\,, \qquad \nabla_\mu F^{\mu\nu} = 0\,. \tag{4.5}$$

We will look for solutions which asymptote to global AdS_4 with a conformal boundary given by $S^2 \times \mathbb{R}_t$. In the gauge/gravity duality a $U(1)$ gauge field $\mathcal{A}_\alpha$ in the bulk is dual to a global current operator J_a in the boundary theory, with lower case latin indices running over the boundary coordinates. In general, turning on a source C_a for the operator J_a on the boundary theory corresponds to a non-normalizable mode of the bulk gauge field. For a source given by a generic electrostatic potential

$$C_t = \Phi(\theta,\phi) = \sum_{l,m} a_{l,m}Y_l^m(\theta,\phi)\,, \tag{4.6}$$

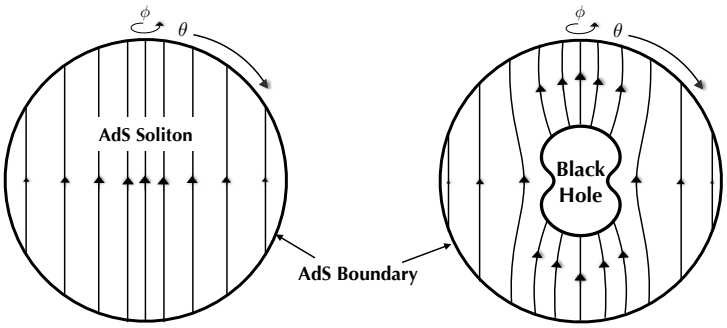

Figure 4.1: Pictorial representation of the two new geometries found in this work. (Left) *AdS* soliton with the electric field throughout space; (Right) Black hole polarised by the electric field.

where Y_l^m are the usual scalar harmonics on S^2, the gauge field near the boundary will have the asymptotic behaviour

$$\mathcal{A} \approx \big(\Phi(\theta,\phi) + 4\pi G_N \rho(\theta,\phi)\, z\big) dt\,, \tag{4.7}$$

where $\{t, \theta, \phi, z\}$ are Fefferman-Graham coordinates in *AdS* [29]. This means that we can turn on any space dependent electrostatic potential (or chemical potential) on the sphere at infinity, without destroying the *good* asymptotic *AdS* behaviour. In other words, the dual theory may be deformed by the relevant operator $C_a J^a$ without altering the UV physics. The response function $\rho(\theta,\phi)$ reads the charge density, that is, how charges are distributed on the sphere due to the interaction with the electric field.

For simplicity in this thesis we shall consider the particular case of a dipolar potential

$$\Phi(\theta) = \mathcal{E}\cos\theta \tag{4.8}$$

at the conformal boundary. With this boundary condition we will construct horizonless solutions describing an *AdS* soliton with a non-trivial electric field. It describes the vacuum of the dual deformed CFT. Then we construct polarised black hole solutions with the same boundary conditions. Figure 4.1 gives a pictorial description of both geometries. We also study the phase diagram of this system at finite temperature, generalizing the Hawking-Page phase transition for the case of an external electric field. A simple analysis of a free charged scalar field on $S^2 \times \mathbb{R}_t$, with conformal coupling, shows a qualitatively similar phase diagram. In appendix B we present the perturbative analysis of the *AdS* soliton solution up to third order in $\mathcal{E}$, which provides a test of our numerics.

4.2 Electric flux in AdS

Let us first consider the new AdS soliton that results from turning on an electric field. In the case of a geometry with axial symmetry a convenient ansatz for our numerical implementation is (setting the AdS radius $l = 1$)

$$ds^2 = \frac{1}{(1-r^2)^2}\Bigg\{ A(r,x)\, d\tau^2 + \frac{4\, G(r,x) dr^2}{2-r^2} + r^2(2-r^2)\left[\frac{4\, C(r,x)}{2-x^2}\left(dx + \frac{H(r,x)dr}{r}\right)^2 + B(r,x)\,(1-x^2)^2 d\phi^2\right]\Bigg\}, \tag{4.9}$$

$$\mathcal{A} = -\, i\, r\, D(r,x)\, d\tau\,,$$

where r is a radial coordinate running from $r = 0$ at the center of space, to $r = 1$ at the AdS boundary. We shall work in the Euclidean setting with the time coordinate τ periodically identified and defined by $t = -i\tau$, as usual. Global AdS corresponds to $A = G = B = C = 1$ and $H = D = 0$. In this case, the usual radial AdS coordinate y is related to r by $y = r\sqrt{2-r^2}/(1-r^2)$ and x is related to the usual polar angle on the S^2 via $x\sqrt{2-x^2} \equiv \cos\theta$. $x \in [-1, 1]$ parametrises the polar coordinate on S^2. Since we consider a dipolar source (5.6), there is a reflection $x \to -x$ symmetry (corresponding in the usual polar coordinates to $\theta \to \pi - \theta$) so we can restrict the domain to $x \in [0, 1]$. We will use the reflection properties of the functions A, G, C, B, H, and D to discretise the equations of motion on a domain bounded by $r = 0, 1$ and $x = 0, 1$. Since the point $r = 0$ is not a boundary but a fixed point of the coordinate system, we need to impose that the geometry is smooth at this point. For the above ansatz this is the same as imposing that the first derivatives along r vanish at $r = 0$. The same logic applies to the fixed point at the axis of symmetry $x = 1$. In this case smoothness implies that the first derivatives along x vanish at $x = 1$, together with $B(r, 1) = C(r, 1)$ and $H(r, 1) = 0$. Finally at $x = 0$, the fixed point of the symmetry $x \to -x$, we require that the first derivatives along x vanish, except for the functions $D(r, x)$ and $H(r, x)$ which vanish at that point.

In the end we are left with one real boundary at $r = 1$. Here we impose that the metric approaches that of global AdS by setting

$$A(1,x) = B(1,x) = C(1,x) = G(1,x) = 1\,, \quad H(1,x) = 0\,. \tag{4.10}$$

We turn on the gauge field by using the boundary condition

$$D(1,x) = \Phi(x)\,, \tag{4.11}$$

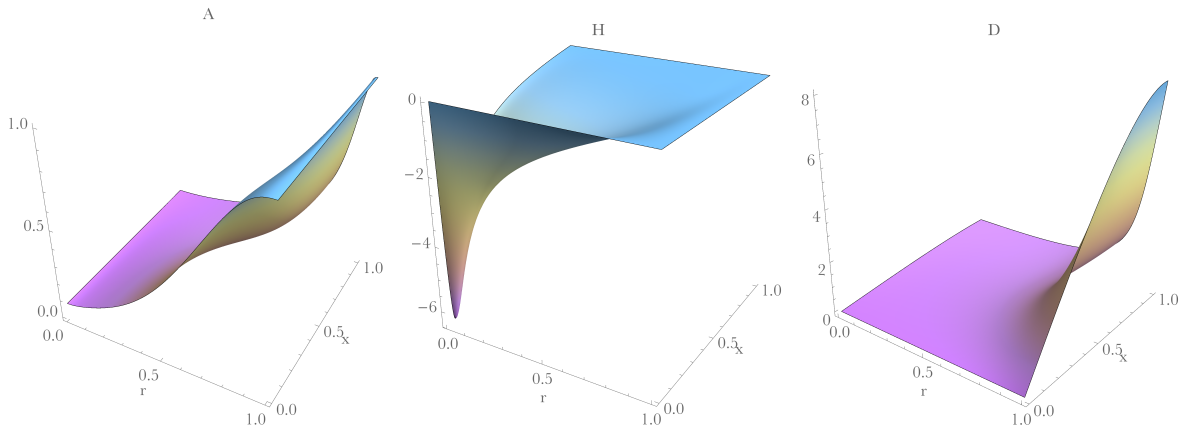

(a) (b) (c)

Figure 4.2: Functions A, H and D for $\mathcal{E} = 8.028$. In this case we used a numerical grid of 200×200 points.

where $\Phi(x) = \mathcal{E}x\sqrt{2-x^2}$ is the dipolar potential (5.6) expressed in terms of x.

We find the solutions using the Einstein-deTurck equations with reference metric given by the functions $A(r,x) = B(r,x) = C(r,x) = G(r,x) = 1$ and $H(r,x) = 0$ in (5.8), which gives a set of elliptic PDE's for the six functions of (5.8). We start with pure AdS as a seed for a solution with small electric field parameter $\mathcal{E}$, and then increase $\mathcal{E}$ using each solution as a seed for the next. These methods were first introduced in [23, 22] and reviewed in [24].

4.2.1 Numerical Solution

In figure 4.2 we show some of the functions in the ansatz (4.9) for a value of the electric field $\mathcal{E}$. We can now calculate several boundary observables, including the charge density $\rho(\theta)$ defined in (4.7), which can be expressed as

$$\frac{1}{4\pi G_N} \star F|_{r=1} = \rho(\theta)\, d\Omega_2\,, \tag{4.12}$$

where $d\Omega_2$ is the volume form on the unit S^2. This is plotted in figure 4.3 for several values of the electric field magnitude. The charge density is maximal at the pole and vanishes at the equator, as expected from the choice of boundary condition.

We can also compute the stress tensor of the boundary theory (2.50) derived in section 2.4. The stress tensor is evaluated using the Fefferman-Graham-like asymptotic expansion of the metric

functions up to $O(1-r)^5$ including logs, for example,

$$A(r,x) = \sum_{i=0}(1-r)^i \alpha_i(x) + \log(1-r)\sum_{i=4}(1-r)^i a_i(x)\,. \tag{4.13}$$

The α's that are not fixed by the equations of motion describe normalizable modes that are then fixed by the boundary conditions. We can determine these by computing derivatives of the appropriate numerical solutions and evaluating them at $r = 1$. For the AdS ansatz written above, the energy density only depends explicitly on the $g_{\tau\tau}$ metric component, that is on the function $A(r,x)$,

$$T_t^{\,t} = -\frac{3\alpha_3(\theta)}{128\pi G_N}\,. \tag{4.14}$$

This is plotted in figure 4.4a. Note that even though we used the coordinate x in the numerics, we decided to plot all our boundary quantities as a function of θ, since this is a more familiar coordinate on the S^2. Like the charge density, $T_t^{\,t}$ is maximal at the pole, minimal at the equator and increases for increasing $\mathcal{E}$. In figure 4.5 we also show the total energy of the boundary theory,

$$E = \int d\Omega_2 T_t^{\,t}\,, \tag{4.15}$$

as a function of $\mathcal{E}$.

For the spatial components of the stress tensor we have

$$\begin{aligned} T_\theta^{\,\theta} &= \frac{-3\big(\alpha_3(\theta)+\beta_3(\theta)\big)}{128\pi G_N}\,, \\ T_\phi^{\,\phi} &= \frac{3\beta_3(\theta)}{128\pi G_N}\,. \end{aligned} \tag{4.16}$$

Here, β_3 is the third-order power-law mode for the metric function B. These are also plotted in figures 4.4b and 4.4c. The $\theta\theta$ component is positive for points below a critical value of θ dependent

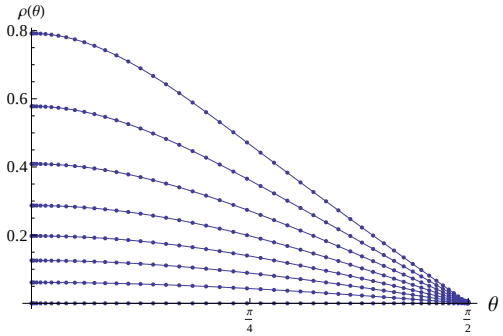

Figure 4.3: The charge density on the AdS boundary for several values of $\mathcal{E} \in [0, 4.4]$ with G_N set to one

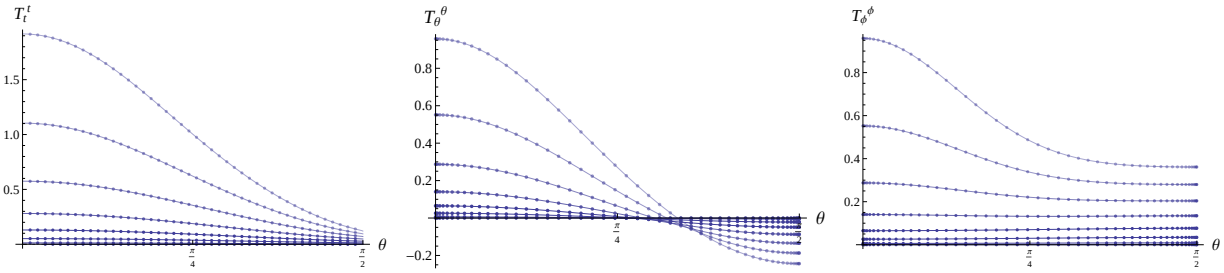

(a) (b) (c)

Figure 4.4: (a) Energy density on the AdS boundary for several values of $\mathcal{E}$; (b)-(c) Spatial components of the boundary stress tensor for several values of $\mathcal{E} \in [0, 4.4]$. In these plots we set $G_N = 1$.

on $\mathcal{E}$, and negative otherwise. That is, near the equator the fluid has negative pressure. The $\phi\phi$ component shows that the pressure along the ϕ direction decreases from the poles to the equator and is independent of ϕ as it should be since there is no net flow of momenta in that direction. All other components of the stress tensor vanish. The non-zero components can be related by an equation describing the conservation of energy and momentum in the presence of a background electric field

$$\nabla_a T^{ab} + j_a F^{ab} = 0\,, \tag{4.17}$$

where $j^a = (\rho, j^i)$ and j^i is the current density on the sphere at the boundary. This equation arises as a consequence of the Ward identities. The only nontrivial component for our ansatz corresponds to $b = \theta$ and leads to the relation

$$\partial_\theta \left(\sin\theta\, T_\theta^\theta\right) - \cos\theta\, T_\phi^\phi = -\mathcal{E}\rho(\theta)\sin^2\theta\,. \tag{4.18}$$

For $\mathcal{E} \neq 0$, this is obeyed by our numerical solutions with a precision of 10^{-8} relative to T_ϕ^ϕ.

Let us now develop some intuition on the behaviour of the AdS soliton in the bulk. We may consider the flux density $\widetilde{\rho}$ through the $\theta = \pi/2$ plane, defined by

$$\frac{1}{4\pi G_N} \star F|_{\theta=\pi/2} = \widetilde{\rho}(r)\sqrt{g_{rr}g_{\phi\phi}}\, dr \wedge d\phi\,. \tag{4.19}$$

The flux density is zero at $r = 1$ and maximal at the AdS center. Figure 4.6a plots this flux density in terms of the proper radial distance from the center of space along the equatorial plane. At $\theta = 0\,, \pi$, this proper distance is given by

$$\mathcal{P}_\theta = \int_0^r \sqrt{g_{rr}(r', \theta)}\, dr'\,. \tag{4.20}$$

As the electric field $\mathcal{E}$ increases we see that the flux is more spread over space. Also, the total value of the flux increases with $\mathcal{E}$, as shown in figure 4.6b. We may also consider the behaviour of the curvature throughout the space. In figure 4.7a we plot the value of the Kretschman scalar invariant $K = R_{\mu\nu\alpha\beta}R^{\mu\nu\alpha\beta}$ in terms of the proper radial distance from the center of space, and observe a similar qualitative behaviour as for the flux density. The growth of the maximal value of the Kretschman scalar with the electric field is also shown in figure 4.7b.

4.3 Polarised black holes in AdS

In this section we consider the geometry that results from placing a black hole in the AdS soliton background. The expectation is that a neutral black hole will polarize, pulling opposite charges to opposite hemispheres and deforming its horizon. We start with the following ansatz for a polarised black hole in AdS

$$\begin{aligned} ds^2 &= \frac{r^2}{(1-r^2)^2}\, A(r,\theta) f(r)\, d\tau^2 \\ &+ \frac{y_0^2}{(1-r^2)^2}\left[4\,\frac{G(r,\theta)}{f(r)}\, dr^2 + C(r,\theta)\big(d\theta + 2rH(r,\theta)dr\big)^2 + B(r,\theta)\sin^2\theta\, d\phi^2\right], \\ \mathcal{A} &= -ir^2 D(r,\theta)\; d\tau\,, \end{aligned} \tag{4.21}$$

where

$$f(r) = \left(1-r^2\right)^2 - \left(1-r^2\right)^3 q_0^2 + y_0^2\left(3-3r^2+r^4\right). \tag{4.22}$$

The radial coordinate r runs from the black hole horizon at $r = 0$ to the AdS boundary at $r = 1$. Setting $A = B = C = G = 1$, $H = 0$ and $D = q_0$ we obtain the Reissner-Nordstrom-AdS black hole of charge q_0, with usual radial coordinate $y = y_0/(1-r^2)$. We are however interested in black holes that are neutral.

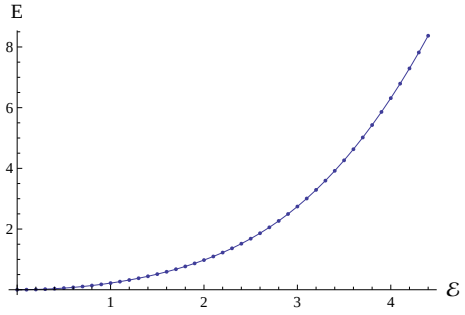

Figure 4.5: Energy of the boundary theory as a function of the electric field $\mathcal{E}$ (setting $G_N = 1$).

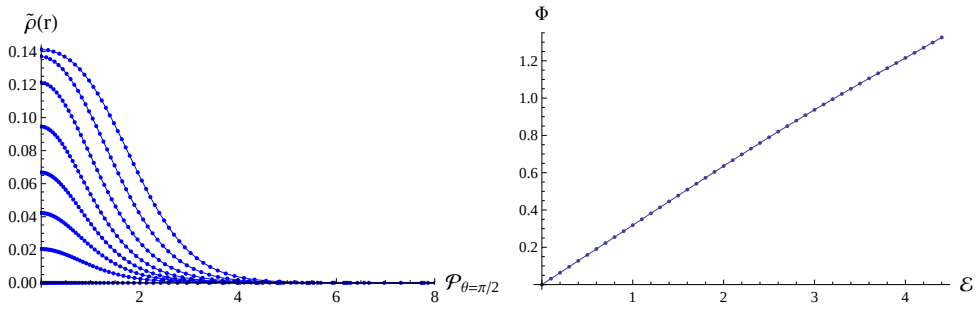

(a) (b)

Figure 4.6: (a) Flux density through the equatorial plan for several values of $\mathcal{E}$ as a function of the proper distance from the center; (b) The total flux through the equator as a function of $\mathcal{E}$ ($G_N = 1$).

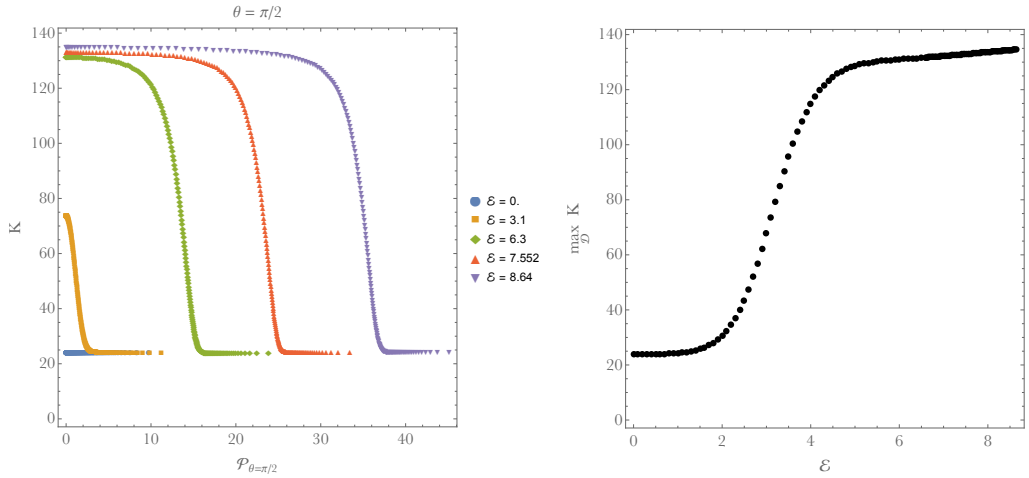

(a) (b)

Figure 4.7: (a) Kretschman scalar invariant at the equator for several values of $\mathcal{E}$ as a function of the proper distance from the center; (b) maximum value of the Kretschman plotted with $\mathcal{E}$.

Let us first pause to understand why we introduced the above constants q_0 and y_0, instead of only y_0. For the boundary conditions that we will impose at $r = 0$ the temperature associated with the periodicity of the thermal circle is $T = (1 - q_0^2 + 3y_0^2)/(4\pi y_0)$. Setting $q_0 = 0$ gives the temperature of an AdS Schwarzschild black hole. If we choose a seed solution with $q_0 = 0$ at some large temperature, then we could find solutions at lower temperatures by decreasing y_0 until we reached the minimum value T_{min} allowed for AdS Schwarzschild. However, we wish to be able to find solutions below this value, if they exist. Introducing q_0 allows us to do this. First we

construct a set of solutions with different values of $\mathcal{E}$ for some temperature above T_{min}. Then, to decrease the temperature and search for solutions below T_{min} for non-zero $\mathcal{E}$, we also need to tune the parameter q_0. A pair (y_0, q_0) is associated to some physical value of the temperature. There is here a degeneracy in the choice of such pairs, that amounts to the idea that different numerical solutions of the unknown functions at the same temperature correspond to the same geometry. We tested this fact by comparing physical quantities like horizon area and curvature invariants of two equivalent pairs. Our choice of introducing the q_0 parameter was simply motivated by the Reissner-Nordstrom-AdS solution for which the temperature can reach zero.

The above ansatz was chosen such that all the functions have vanishing first derivative with respect to r at the horizon. In particular, we see that whatever the value of the function $A(r, \theta)$ at $r = 0$, the temperature of the solution will not be affected, since it is fixed by the parameters y_0 and q_0 in $f(r)$, as described in the previous paragraph. As a consequence of these boundary conditions, all metric functions and the gauge field function $D(r, \theta)$ will be smooth functions of r^2. Given this smoothness at the horizon, the condition $A(0, \theta) = G(0, \theta)$ is fixed by the equation of motion. This guarantees that the geometry closes smoothly at the $r = 0$ axis. For the boundary conditions at the $\theta = 0$ axis and the $\theta = \pi/2$ symmetric point we have chosen an ansatz such that the boundary conditions are the same as for the AdS soliton of the previous section.

Again we are left with a single boundary at $r = 1$. We impose that (4.21) approaches the AdS boundary by setting

$$A(1, \theta) = C(1, \theta) = B(1, \theta) = G(1, \theta) = 1\,, \quad H(1, \theta) = 0\,. \tag{4.23}$$

We also require that the gauge field approaches the dipolar potential, as for the AdS soliton. This will ensure a comparison between two competing solutions with the same asymptotics. As in the previous section, we use the Einstein-deTurck trick with reference metric $A(r, \theta) = C(r, \theta) = B(r, \theta) = G(r, \theta) = 1$ and $H(r, \theta) = 0$ in (4.21).

4.3.1 Results

In figure 4.8 we show some of the functions in the ansatz (4.21) for some value of the electric field and temperature. For a given temperature there will be two solutions. For that reason, we will refer to these solutions as *large* and *small* black holes. As we decrease the temperature in our search for solutions there is a minimum value of the temperature $T_{min}(\mathcal{E})$ below which there is no black

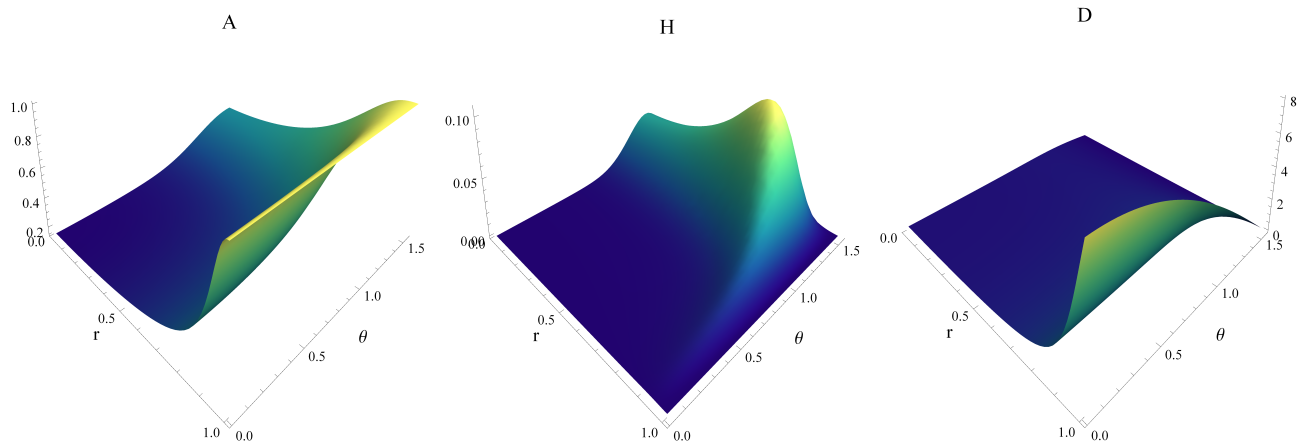

(a) (b) (c)

Figure 4.8: Examples of numerical solutions for A, H, and D for a large polarised black hole for a value of the electric field $\mathcal{E} = 2$ and temperature $T = 1/\pi$. In this case we used a numerical grid of 44×44 points.

hole solution. This is entirely analogous to the pure AdS Schwarzschild black hole case, where now $T_{min}(\mathcal{E})$ is a decreasing function of $\mathcal{E}$.

First we can look at the horizon area, which computes the entropy in the boundary theory. This is just the Hawking-Bekenstein entropy

$$S = \frac{\mathcal{A}}{4G_N} = \frac{\pi y_0^2}{G_N} \int_0^{\frac{\pi}{2}} d\theta \, \sin\theta \sqrt{C(0,\theta)B(0,\theta)} \, . \tag{4.24}$$

Figure 4.9 shows the black hole entropy of the large and small black holes as a function of the temperature for several values of the electric field. The blue curves have higher entropy and therefore correspond to the large black hole branch. These large black holes grow with increasing temperature. Conversely, the small black holes, represented by the red curves, shrink with increasing temperature. We also see that the point where the curves meet corresponds to a minimum temperature $T_{min}(\mathcal{E})$ and that this minimum decreases with increasing $\mathcal{E}$.

The shape of the horizon can be drawn by computing isometric embeddings of the horizon geometry in Euclidean space. In figure 4.10a we plot the embeddings for the large and small black holes in blue and red, respectively. Note that the largest blue curve and the smallest red curve correspond to the same temperature. The curves get increasingly more faint as the temperature is decreased. We see that, as expected from figure 4.9, the large black hole shrinks and the small black hole expands with decreasing temperature until the minimum is reached. Figure 4.10b is a plot of

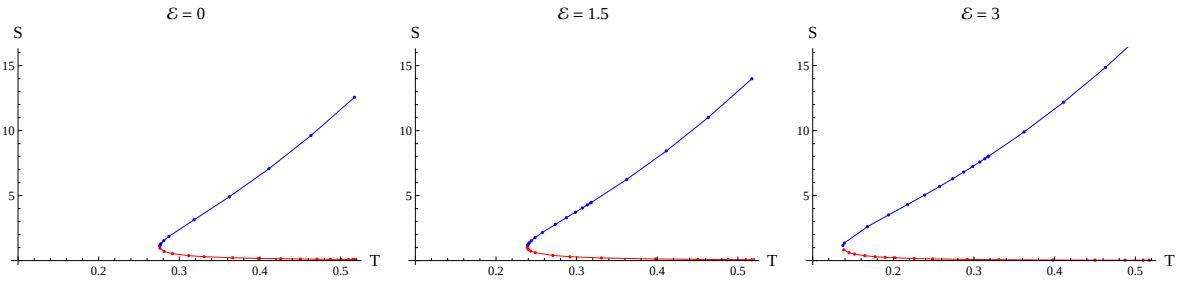

(a) (b) (c)

Figure 4.9: Black hole entropy as function of the temperature for several values of the electric field for $G_N = 1$. The blue curves correspond to the large black hole branch and the red curves to the small black hole branch. These curves meet at the minimum temperature $T_{min}(\mathcal{E})$ below which there are no black hole solutions.

the large black hole embeddings for fixed temperature up to a large value of electric field $\mathcal{E} = 10.5$. Solutions with higher values of $\mathcal{E}$ at this temperature can no longer be isometrically embedded in flat space, since its Gaussian curvature becomes too negative near the equatorial plane[1]. As the electric field is increased, the black hole stretches until the geometry begins to pinch around the equator and the horizon deforms into a peanut shape.

Again we may study the boundary charge density $\rho(\theta)$ defined in (4.7) and (4.12). The charge is distributed along the sphere in a similar way as for the AdS soliton (see figure 4.3). The total boundary charge contained in one hemisphere is shown in figures 4.11a and 4.11b for two values of $\mathcal{E}$. It is also interesting to look at the charge distribution and total charge that has polarised at each hemisphere of the horizon, just by computing the electric flux across the horizon. Figures 4.11c and 4.11d show the total polarised charge in each hemisphere for the same two values of $\mathcal{E}$. We checked that the difference between the charges in one hemisphere at the boundary and the black hole horizon equals the electric flux through the equator, as expected.

Let us now calculate the boundary energy-momentum tensor of the dual to the black hole

[1]This phenomenon also occurs when we look at the isometric embedding of the spatial cross section of the horizon of a rapidly rotating Kerr black hole in three dimensional flat space - see for instance [30].

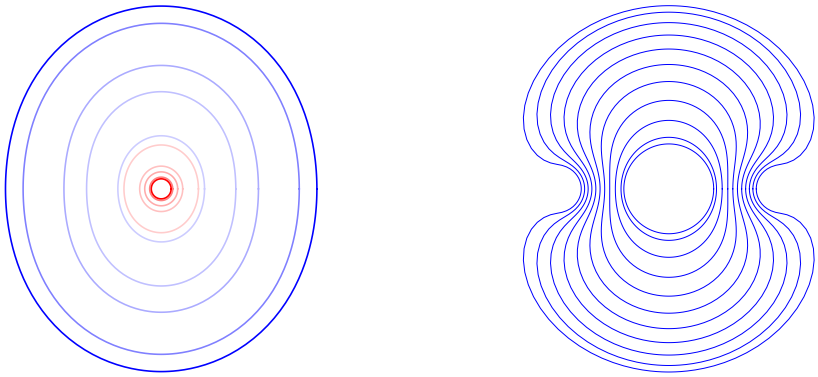

(a) (b)

Figure 4.10: (a) Isometric embeddings of black hole horizons at fixed $\mathcal{E} = 2$. Blue curves represent large black holes and red curves represent small black holes. The largest blue and smallest red curves start at $T = 0.52$ and get fainter as the temperature is decreased. The faintest blue and red lines correspond to $T = 0.21$. (b) Isometric embeddings of constant temperature black holes ($T = 1/\pi$) up to a large value of $\mathcal{E} = 10.5$.

geometry. The non-vanishing elements of the stress tensor are

$$\begin{aligned} T_t^t &= \frac{y_0}{128\pi G_N}\Big(16\left(1+q_0^2+y_0^2\right) - 3y_0^2\alpha_3(\theta)\Big), \\ T_\theta^\theta &= \frac{y_0}{128\pi G_N}\Big(8\left(1+q_0^2+y_0^2\right) - 3y_0^2\big(\alpha_3(\theta)+\beta_3(\theta)\big)\Big), \\ T_\phi^\phi &= \frac{y_0}{128\pi G_N}\Big(8\left(1+q_0^2+y_0^2\right) + 3y_0^2\beta_3(\theta)\Big), \end{aligned} \tag{4.25}$$

where, as before, α_3 and β_3 are the third-order power-law modes associated to the functions A and B, respectively. The profiles are similar to those found for the AdS soliton, with maximum values at the pole and minima at the equator for $\mathcal{E} \neq 0$. Some energy density profiles are shown in figures 4.12a-c for various values of the temperature and electric field magnitude. Like the AdS soliton, the energy density increases with increasing $\mathcal{E}$. For fixed $\mathcal{E}$, it also increases with increasing temperature, as expected. The $\theta\theta$ component is plotted in figure 4.12d-f. It is similar to the AdS soliton case, except that it now becomes negative below a critical value of θ dependent on both $\mathcal{E}$ and T. We have checked that the conservation equation (4.18) has a 1% precision with respect to T_ϕ^ϕ for our numerical solutions. The $\phi\phi$ component, plotted in figure 4.12g-i, has a similar behavior. Again, this measures the pressure along ϕ, that is independent of ϕ, but decreases from the pole to the equator.

Integrating the energy density, we get the total energy measured at infinity, which is plotted in

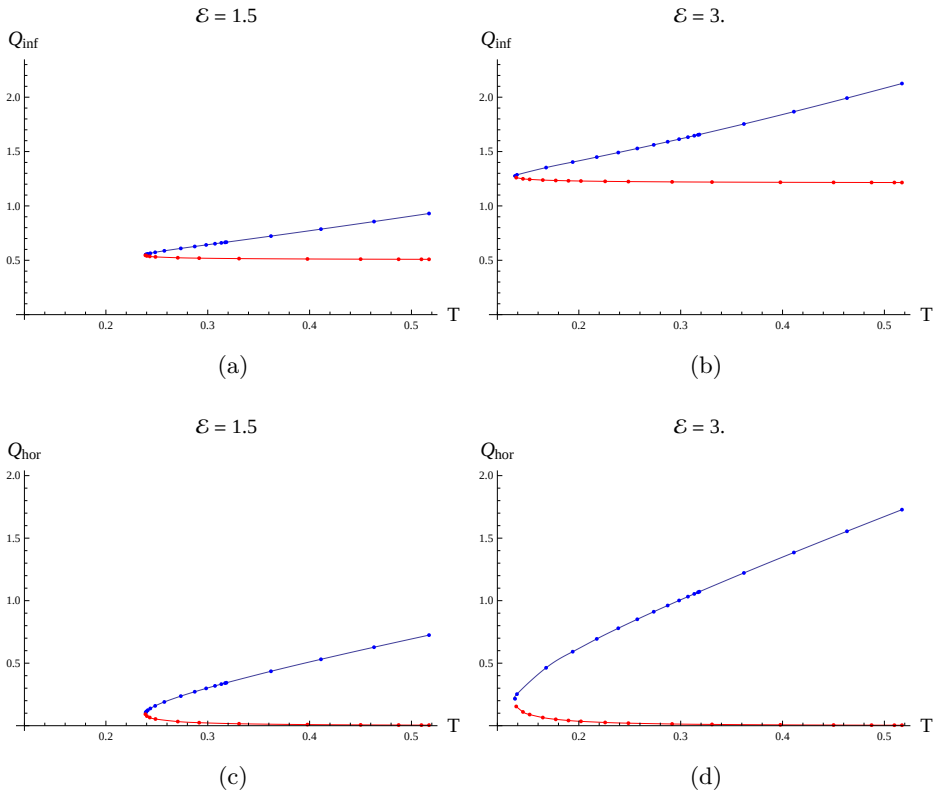

Figure 4.11: (a)-(b) Total charge in one hemisphere at the AdS boundary; (c)-(d) and at the black hole for $G_N = 1$. The blue curves corresponds to large black holes, while the red ones to small black holes.

figure 4.13. The energy of the large black hole increases with temperature while that of the small black hole decreases with temperature. Notice that both the entropy and energy agree with the analytical result of the AdS-Schwarzschild solution when $\mathcal{E} = 0$.

4.4 Smarr formula

A nice check of the numerics is to verify whether the new black hole solutions verify the corresponding Smarr formula. This will relate boundary data with properties of the horizon.

For every killing vector v we can write an antisymmetric conserved tensor

$$(K_v)^{ab} = \nabla^a v^b - 3\omega^{ab} + 2v^{[a}F^{b]c}A_c + 2F^{ab}v^c A_c v^a \,, \tag{4.26}$$

For this we need to define the form ω, given by equation (2.57) in section 4.4. throughout the

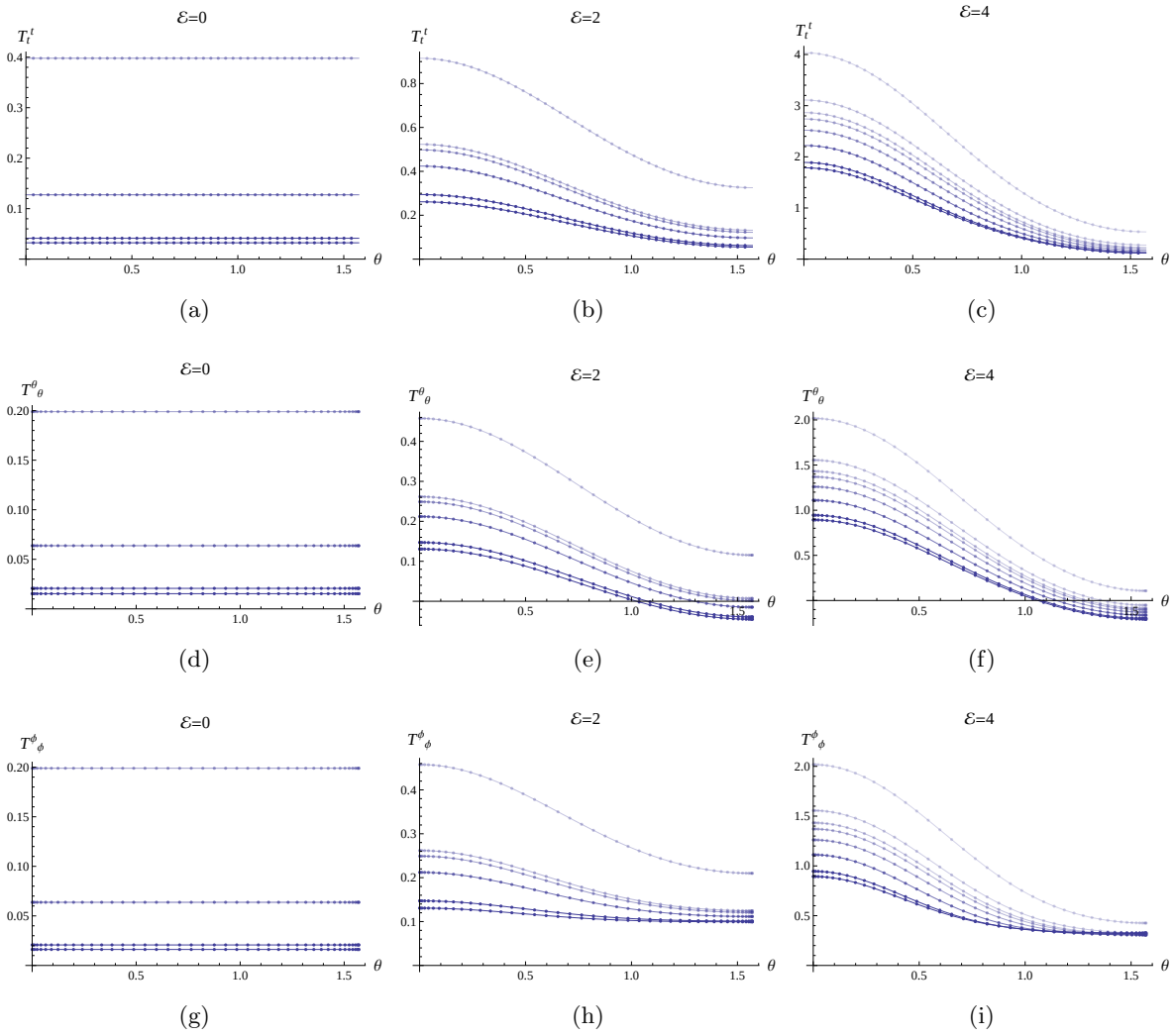

Figure 4.12: (a)-(c) Boundary energy density for several values of $\mathcal{E}$ for the large black hole; (d)-(f) the $\theta\theta$ component and (g)-(i) the $\phi\phi$ component of the boundary stress tensor at the same values of $\mathcal{E}$ and T. Darker curves correspond to higher temperatures. (Setting $G_N = 1$.)

whole space. For the generator of time translations $v = \partial/\partial\tau$, we can choose the only non-vanishing component as

$$\omega^{r\tau}(r,\theta) = \frac{1}{\sqrt{g}}\left(\int_0^r (\sqrt{g} - \sqrt{g_0})\, dr' + \int_0^r \sqrt{g_0}\, dr'\right). \tag{4.27}$$

We have added and subtracted a contribution from an arbitrary metric g_0 that allows us to split up the integral into a finite and divergent piece. This is useful because it isolates the infinite piece that comes from the form ω, which is canceled by the divergence that comes from the other terms in (4.26). As reference metric g_0 we choose the Reissner-Nordstrom-AdS metric written in the

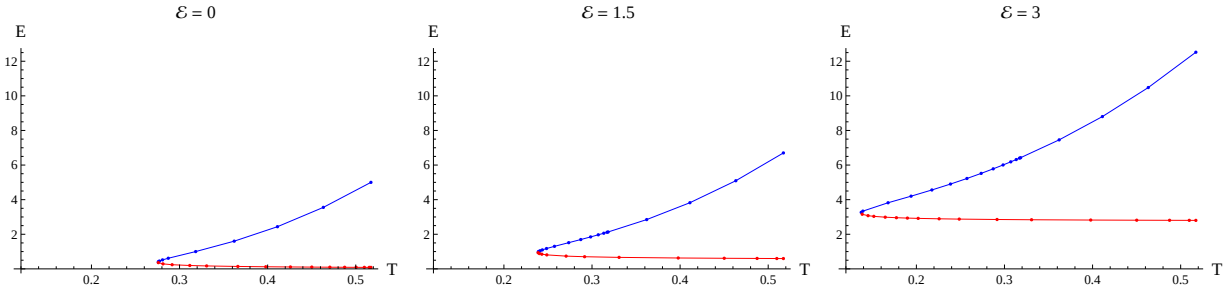

(a) (b) (c)

Figure 4.13: Total energy at the boundary for the dual state of the black hole for $G_N = 1$.

coordinates of (4.21) in terms of the parameters y_0 and q_0 since it has the same asymptotics as our ansatz. We need to integrate the conservation equation $d(\star K_v) = 0$ from the horizon to the AdS boundary to obtain

$$\int_{hor} \star K_v = \int_{bound} \star K_v \,. \tag{4.28}$$

Making the above choice, (4.28) becomes the finite expression

$$TS - \frac{y_0^3}{2G_N} = E - \frac{y_0}{4G_N}\left(1 + y_0^2 + q_0^2\right) - \pi \int_0^\pi d\theta \sin\theta\, \rho(\theta)\Phi(\theta) - \frac{3}{4G_N}\int_0^\pi d\theta \int_0^\infty dr(\sqrt{g} - \sqrt{g_0})\,. \tag{4.29}$$

The left-hand side is the integral taken at the horizon, while the right-hand side is taken at infinity. We computed the difference in Komar integrals at the horizon and infinity relative to the integral at infinity and found that the error is below 1%.

4.5 Thermodynamics

Both the AdS soliton presented in section 5.2 and the black hole of section 6.3 were defined with Euclidean signature. Therefore, they are already in a form that allows us to analyse the thermodynamic properties of this system. For the AdS soliton we may choose freely the periodicity of the time circle, since the solution at fixed electric field is always the same. On the other hand, for a given temperature we need to look for the corresponding large and small black holes that are regular at the *Euclidean horizon*. Our goal in this section is to compare the free energies of these geometries to draw the corresponding phase diagram.

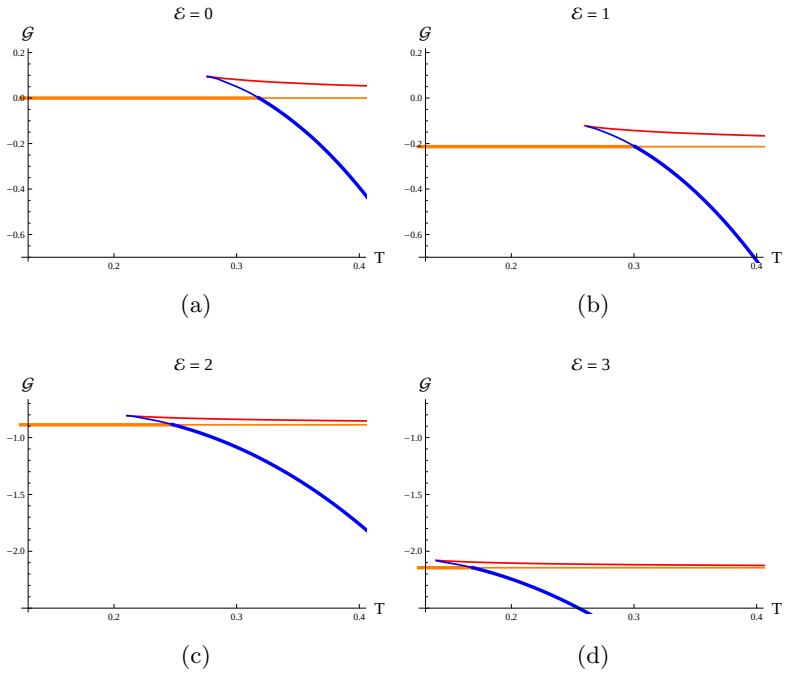

Figure 4.14: Gibbs free energy for the large black hole (blue curve), small black hole (red curve) and AdS soliton (orange line) for several values of the electric field as a function of the temperature. Thicker lines single out the dominant phase. In these plots we set $G_N = 1$.

The free energy associated to a geometry with an electrostatic source $\Phi(\theta)$ at the boundary is

$$\mathcal{G} = E - TS - 2\pi \int_0^\pi d\theta \sin\theta \, \rho(\theta) \, \Phi(\theta) \,, \tag{4.30}$$

where E is the energy, S is the Bekenstein-Hawking entropy and $\rho(\theta)$ is the charge density at the boundary. For the AdS soliton the entropy vanishes since there is no horizon, and the energy and charge density are independent of T. For both the AdS soliton and black hole geometries all functions were determined in the previous sections. Figure 4.14 shows the Gibbs free energy of the large black hole (blue curve), the small black hole (red curve), and AdS soliton (orange line). The curves for the AdS soliton and black hole phases are thicker when they are the dominant phase. The large and small black hole picture is very similar to that of the RN-AdS black holes in a constant potential background in [31, 32]. The small black hole branch always has higher free energy than the large black hole branch and is therefore not thermodynamically favoured. The phase transition between the large black hole and AdS soliton phases occurs when the curves of the two phases cross. We see that for $\mathcal{E} = 0$ the phase transition occurs at $T = 1/\pi$, in agreement with the first order Hawking-Page phase transition of a Schwarzschild black hole in AdS. As the

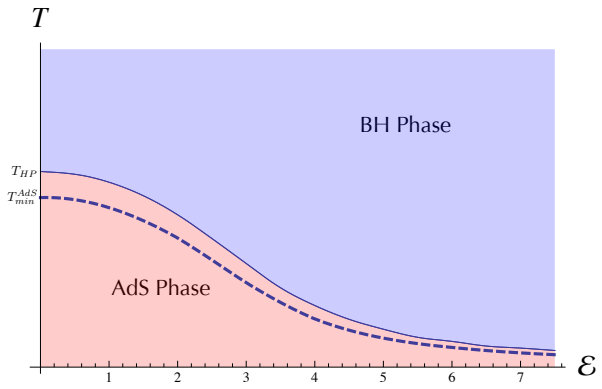

Figure 4.15: Phase diagram with the critical temperature (solid curve) above which the black hole phase is thermodynamically favoured. The minimum temperature for the black holes (dashed curve) is also shown.

electric field increases, the phase transition moves toward lower temperatures. Figure 4.15 shows the phase diagram. The blue region is in the black hole phase while the red region is in the AdS soliton phase. It seems that the critical temperature will tend towards zero as the electric field becomes very large. The lower dashed curve marks the minimum temperature of the black hole solutions, where large and small black holes meet.

To analyze the stability of the black holes, we calculated the specific heat $C = T(dS/dT)$. We find that large black holes are stable, while small black holes are not, as follows from figure 4.9. It is also clear from figure 4.9 that the specific heat will diverge when $T \to T_{min}$.

4.6 Free boson on a sphere with dipolar potential

One very simple toy model to gain intuition about the dual field theory is a free charged scalar field satisfying the Klein-Gordon equation on the two-sphere

$$D_\mu D^\mu \varphi = M^2 \varphi \,, \tag{4.31}$$

where $D_\mu = \nabla_\mu - iC_\mu$. We shall focus on the conformal case that corresponds to $M^2 = \frac{1}{4}$ with units such that the sphere radius is equal to 1. Considering the geometry of the cylinder $S^2 \times \mathbb{R}_t$ and the dipolar potential $C = \mathcal{E} \cos\theta \, dt$, we find

$$\left[-\left(\partial_t - i\mathcal{E}\cos\theta\right)^2 + \nabla^2_{S^2} \right] \varphi = M^2 \varphi \,. \tag{4.32}$$

For $\mathcal{E} = 0$ the eigenstates are simply given by the spherical harmonics $|l, m\rangle$ with wave-functions

$$\langle \theta, \phi | l, m \rangle \propto e^{im\phi} P_l^m(\cos\theta)\,, \tag{4.33}$$

where P_l^m are the associated Legendre polynomials. The spectrum of the Hamiltonian $\widehat{H} = i\partial_t$ is given by

$$\widehat{H}\,|l, m\rangle = \sqrt{M^2 - \nabla_{S^2}^2}\,|l, m\rangle = \sqrt{l(l+1) + M^2}\,|l, m\rangle = \left(l + \frac{1}{2}\right)|l, m\rangle\,, \tag{4.34}$$

in agreement with the scaling dimensions of the local operators $\partial_{\mu_1} \ldots \partial_{\mu_l}\varphi$ that constitute the conformal family of a free scalar field φ in three dimensions. These states have charge 1 and are degenerate with the states of charge -1 associated with $\partial_{\mu_1} \ldots \partial_{\mu_l}\overline{\varphi}$.

After turning on the electric field $\mathcal{E}$, the hamiltonian becomes

$$H = \sqrt{M^2 - \nabla_{S^2}^2} - \mathcal{E}\cos\theta\,, \tag{4.35}$$

which is still diagonal in the azimuthal quantum number m but it becomes an infinite tridiagonal matrix in the quantum number $l \geq |m|$,

$$\langle l', m'|H|l, m\rangle = \delta_{m,m'}\left\{\delta_{l,l'}\left(l + \frac{1}{2}\right) + \mathcal{E}\left[\delta_{l,l'-1}\sqrt{\frac{(l+1-m)(l+1+m)}{(2l+1)(2l+3)}} + (l \leftrightarrow l')\right]\right\}. \tag{4.36}$$

Here we have used the conformal value of the mass $M^2 = 1/4$. The off-diagonal terms of the hamiltonian can be easily computed using normalized wave-functions in position space, which leads to integrals of the form $\int_{-1}^{1} dx P_l^m(x) P_{l'}^m(x) x$. We would like to determine the energy spectrum of this hamiltonian for each m. However, for each m the hamiltonian is an infinite tridiagonal matrix $(H_m)_{ll'}$ with the indices $l, l' = |m|, |m|+1, |m|+2, \ldots$. Our strategy will be to truncate the values of l, l' up to a maximal value L and (numerically) compute the eigenvalues of the resulting finite dimensional matrix. The lowest eigenvalues of the truncated matrices converge exponentially fast to the eigenvalues of the infinite matrix as we increase the cut-off L. The resulting low energy spectrum in the $m = 0$ sector is shown in figure 4.16a. Notice that for $\mathcal{E} > \mathcal{E}_c \approx 1.3868$ the single particle ground state energy becomes negative. The energy decreases because the wave-function concentrates around the pole where the potential is negative. In fact, the single-particle states always come in degenerate pairs labelled by the charge 1 or -1, with wave-functions related by the interchange $\theta \leftrightarrow \pi - \theta$. For $\mathcal{E} > \mathcal{E}_c$ the system is unstable because we can lower the energy without bound by accumulating bosons in the single-particle ground states. The analysis of these conformally coupled, bosonic fields will also be useful in the next chapter.

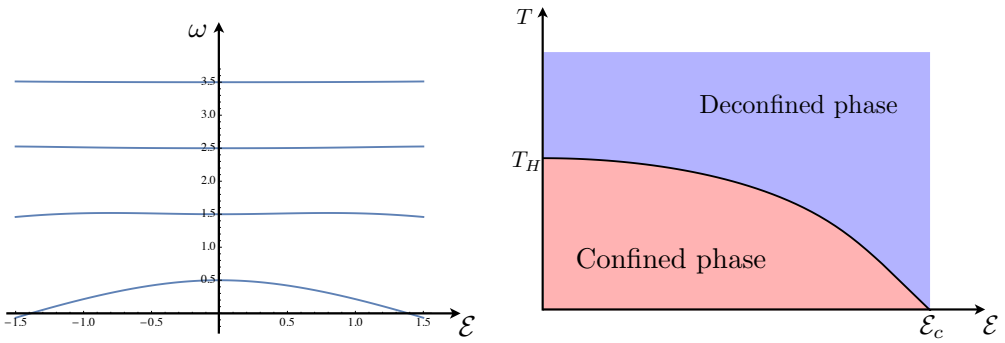

(a) (b)

Figure 4.16: (a) First four energy levels in the $m = 0$ sector as a function of the dipolar potential $\mathcal{E}$. (b) Large N phase diagram of a free adjoint scalar field. The Hagedorn temperature decreases with the dipolar potential $\mathcal{E}$ and goes to zero as $\mathcal{E} \to \mathcal{E}_c$.

Let us now consider the system at finite temperature. We can define the single-particle partition function

$$z(x, \mathcal{E}) = 2 \sum_{m=-\infty}^{\infty} \sum_{k=0}^{\infty} e^{-\beta \omega_{m,k}(\mathcal{E})} , \qquad x \equiv e^{-\beta} , \tag{4.37}$$

where $\omega_{m,k}(\mathcal{E})$ is the energy spectrum of the hamiltonian (5.27) and the factor of 2 accounts for the two possible charge assignments. We would like to consider a $SU(N)$ gauge theory with a scalar field φ in the adjoint representation. Then, the gauge-invariant states can be written as products of traces of products of the elementary fields φ and $\overline{\varphi}$. As explained in [33, 34, 35], in the large N limit and below the Hagedorn temperature, the full partition function is given by

$$\log Z(x) = -\sum_{n=1} \log \left[1 - z_B(x^n) + (-1)^n z_F(x^n) \right] , \tag{4.38}$$

where z_B and z_F are the bosonic and fermionic single-particle partition functions. For simplicity, we will only consider the bosonic contribution $z(x, \mathcal{E})$ of the complex scalar field φ. The Hagedorn temperature is then given by the condition

$$z(x_H, \mathcal{E}) = 1 , \qquad x_H = e^{-\beta_H} . \tag{4.39}$$

We plot the corresponding phase diagram in figure 4.16b. As usual, there is a low temperature confined phase and a high temperature deconfined phase separated by a Hagedorn phase transition. The novelty is that the Hagedorn temperature decreases with the dipolar potential $\mathcal{E}$ and goes to zero as $\mathcal{E} \to \mathcal{E}_c$.

4.7 Discussion

Given the shape of the horizon of the polarised black hole for large dipolar potential, it is natural to wonder if the thermodynamically favourable solution contains two black holes. In order to investigate this question we consider the free energy variation of the system when adding two infinitesimal small black holes of opposite charges. The first step is to determine their equilibrium position. Since the putative black holes are infinitesimal we can work in the probe approximation. Therefore, equilibrium positions are just located at the minima of the potential

$$V = \sqrt{g_{\tau\tau}} - \frac{q}{m} A_\tau \,, \tag{4.40}$$

where q and m are the charge and mass of the black holes. Since these black holes are small, their properties can be described by Reissner-Nordstrom black holes in flat space. These have

$$m = r_+ - r_+^2 2\pi T \,, \qquad q^2 = r_+^2 - r_+^3 4\pi T \,, \qquad s = \pi r_+^2 \,, \tag{4.41}$$

where r_+ is the outer horizon radius and s is the entropy (we are using $G_N = 1$). At finite temperature T, we find $q/m \to 1$ in the probe limit $r_+ \to 0$. We find that timelike static orbits of oppositely charged test particles do exist along the $\theta = 0$ axis for $q = m$ in the AdS soliton background. The potential and position of the corresponding minima are plotted in figure 4.17. The black curve is the location, in terms of proper distance along the axis defined by $\theta = 0, \pi$, of point like charged extremal particles in our perturbative backgrounds is given by (in units of $\ell = 1$)

$$\mathcal{P}^\star_{\theta=0} = \frac{4}{3\pi}\,\mathcal{E} + \frac{\mathcal{E}^3}{14175\pi^3}\left[77760\zeta(3) + 33400 - 9\pi^2(979 + 1152\log 2)\right] + \mathcal{O}(\mathcal{E}^5)\,. \tag{4.42}$$

We see a very good agreement with our numerical results for small $\mathcal{E}$. We may now consider the free energy variation of the solution corresponding to the addition of a probe extremal black hole,

$$\delta\mathcal{G} = m\left(\sqrt{g_{\tau\tau}} - \frac{q}{m}A_\tau\right)_{min} - Ts = r_+ V_{min} + O(r_+^2)\,. \tag{4.43}$$

We conclude that it is not advantageous to add probe black holes if the probe potential at the minimum is positive, which is what we found at least up to $\mathcal{E} \sim 9$. It would be interesting to look for new two black hole solutions, beyond the probe approximation, to complete the phase diagram. This could lead to a maximum value of the electric field above which the AdS soliton is not the favoured low temperature phase.

There are some similarities between the weak coupling phase diagram of figure 4.16b and the gravitational (strong coupling) phase diagram of figure 4.15. The main qualitative difference between weak and strong coupling seems to be the existence, or not, of a maximal dipolar potential

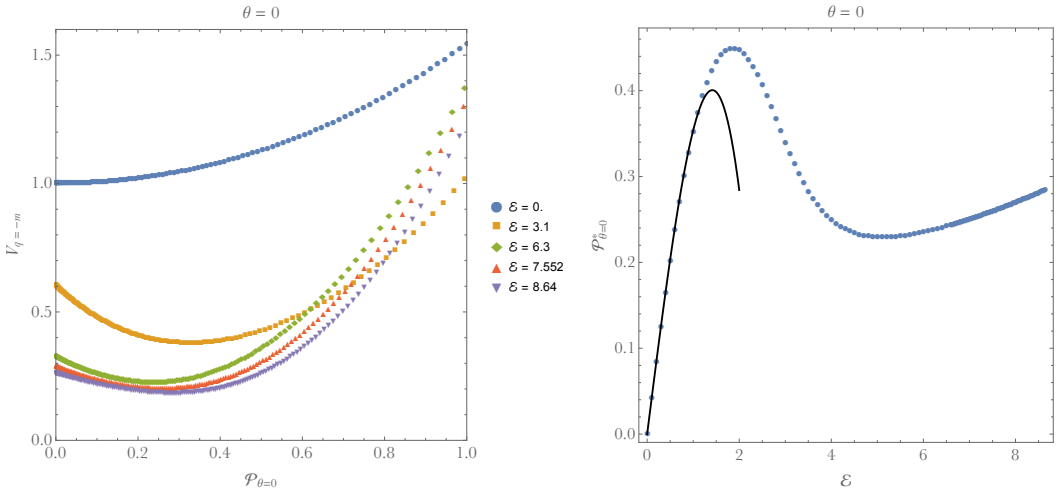

(a) (b)

Figure 4.17: Potential for timelike static orbits of extremal charged particles in the AdS background is plotted in (a) for several values of the electric field. In (b) we plot the location of the extremal charged particles as a function of the electric field. The black curve is the result obtained via perturbation theory analysis, which is detailed in appendix A.

$\mathcal{E}_c$. It is natural to speculate that $\mathcal{E}_c$ increases with the coupling and diverges at strong coupling. However, the difference at strong and weak coupling suggests that we don't know which theory is dual to the gravitational set-up we have just considered. In the next chapter, we look at black hole polarization applied to ABJM theory. This is a concrete realization of the gauge/gravity duality [36]. In this case, one can interpolate between the two phase diagrams by changing the t'Hooft coupling of the theory. Indeed, we will see that the gravity computation in this setup gives rise to a maximum electric field.

Chapter 5

Black Holes in ABJM

In the last chapter, we showed that neutral black holes of spherical topology, placed in four-dimensional Anti-de Sitter space-time, are polarised when subject to an external electric field. At finite temperature, this gravitational system is described by a two-dimensional phase diagram, in terms of its temperature T and electric field parameter $\mathcal{E}$. The system has two phases, a lower temperature phase described by an AdS soliton with a self-gravitating electric field, and a higher temperature phase described by the polarised black hole. The critical temperature decreases with the external electric field. For pure Einstein-Maxwell theory we observed that the external electric field could be made arbitrarily large, with the critical temperature converging to zero in the limit of large electric field.

5.1 Introduction

One of the motivations for the above study was to consider three-dimensional conformal theories on $\mathbb{R}_t \times S^2$, subject to an external electric field source that couples to a global current operator. The two distinct phases are then expected to describe confining and deconfining phases, with a critical temperature that depends on the external electric field. Intuitively we expect the critical temperature to decrease with the external field because of the electric repulsion between the partonic degrees of freedom. The analysis of a free conformally coupled scalar field in the presence of such external electric field supports this intuition and shows the existence of a maximal electric field, above which the vacuum is itself unstable. However, such maximum electric field is not seen in

the gravitational analysis done with pure Einstein-Maxwell theory. This fact is not necessarily contradictory because we do not know if pure Einstein-Maxwell theory is dual to a CFT. The goal of this chapter is to clarify this point by considering a consistent truncation of the gravitational dual of ABJM theory [1]. This truncation includes a current operator that we can turn on in order to deform the ABJM CFT, therefore studying this problem in a precise holographic setup.

This can be done by considering the decoupling limit of M2-branes, which leads to a duality between string theory on $AdS_4 \times S^7/\mathbb{Z}_k$ and three dimensional ABJM theory, a superconformal Chern-Simons matter theory named after the authors of [1]. It contains four complex scalars and four Majorana fermions, as well as Chern-Simons gauge fields that do not carry any degrees of freedom. The ABJM action has an $\mathcal{N} = 6$ supersymmetry and corresponding R-symmetry $SU(4)_R \times U(1)$. The bosons and fermions transform in the fundamental of $SU(4)$ and are charged under the $U(1)$. ABJM has gauge group $U(N)_k \times U(N)_{-k}$ where k is an integer that labels the Chern-Simons level. This level parameter enters the ABJM action in an overall factor of $k/(4\pi)$, suggesting that it may take the place of the coupling constant, which would generally appear in the action as $1/g_{YM}^2$. Indeed, this theory is governed by a 't Hooft coupling $\lambda = N/k$, where N is the number of M2 branes. Perturbation theory is therefore valid when $k \to \infty$, and the theory is strongly coupled when $k = 1$, which corresponds to the theory of N coincident M2 branes in flat space. The geometry of the M2-branes is given by (2.26). Flowing to the low-energy limit in which $U \ll l$ corresponds to the near-horizon geometry

$$ds^2 = l^2 \left(\frac{1}{4} ds^2_{AdS_4} + ds^2_{S^7} \right). \tag{5.1}$$

Distributing the factor of l through to each piece of the metric, we see that the AdS scale $l_{AdS} = l/2$, so the radius of curvature of AdS_4 is half that of the S^7. In planck units, $l = l_p(32\pi^2 Nk)^{1/6}$. This metric exhibits a global $SO(8)$ symmetry. The gravity dual of ABJM can be described by a collection of N M2-branes probing the $\mathbb{C}^4/\mathbb{Z}_k$ singularity of the 8-dimensional space perpendicular to the M2-branes. This breaks the $SO(8)$ symmetry. Such an orbifold rotates the phases of the four complex coordinates z_n of $\mathbb{C}^4$,

$$z_n \to e^{2\pi i/k} z_n, \tag{5.2}$$

preserving an $SU(4) \times U(1)$ isometry instead. This leads to the geometry $AdS_4 \times S^7/\mathbb{Z}_k$. M theory on this background corresponds to ABJM theory in the large N limit. However, notice that $S^7/\mathbb{Z}^k$

metric can be written as an S^1 fibre over the projective space $\mathbb{CP}^3$.

$$l^2 ds^2_{S^7/\mathbb{Z}^k} = l^2 \left(\frac{1}{k} d\tau + \omega\right)^2 + l^2 ds^2_{\mathbb{CP}^3}\,, \qquad d\omega = i \sum_i d\left(\frac{z_i}{r}\right) d\left(\frac{d\overline{z}_i}{r}\right) \tag{5.3}$$

$$ds^2_{\mathbb{CP}^3} = \frac{1}{r^2} \sum_n dz_n d\overline{z}_n - \frac{1}{r^4} \left| \sum_n z_n d\overline{z}^n \right|^2\,, \qquad r^2 \equiv \sum_{n=1}^{4} |z_n|^2$$

where τ is 2π periodic and $d\omega$ is a Kalher form on $\mathbb{CP}^3$. Since $(l/k) \approx (N/k^5)^{1/6}$, the radius of the S^1 becomes negligible in the limit $k^5 \gg N$, and the seven sphere geometry reduces to $l^2 ds^2_{\mathbb{CP}^3}$. In other words, the M-theory circle of compactification becomes small in this limit, when the description is no longer weakly curved. The appropriate dual description for ABJM is then type IIA string theory on $AdS_4 \times \mathbb{CP}^3$.

When is the supergravity approximation valid? In string units, the radius of curvature is given in terms of the 't Hooft coupling $\lambda = N/k$ by

$$R^2_{string} = \frac{l^3}{k} = 2^{5/2} \pi \sqrt{\lambda}. \tag{5.4}$$

Supergravity is valid when $R^2_{string}/l^2_s \gg 1$, or at large 't Hooft coupling.

In what follows, we consider a consistent truncation of eleven-dimension supergravity on $AdS_4 \times S^7/Z_k$. More concretely, we can break the $SU(4) \times U(1)$ R-symmetry to $U(1)^4$. The bosonic sector of this theory is given by the metric, three scalar fields and, as expected, four $U(1)$ gauge fields [37]. A further consistent truncation can be made to reduce the theory to gravity, a gauge field and a single scalar field, with the following action[1]

$$S_{bulk} = \frac{1}{16\pi G_N} \int d^4x \sqrt{g} \left(R - \frac{1}{2} \nabla_\mu \Phi \nabla^\mu \Phi + \frac{2}{l^2} (\cosh \Phi + 2) - \frac{1}{2} e^{\Phi} F^2 \right)\,, \tag{5.5}$$

where $F = dA$ and G_N the Newton constant. For vanishing scalar and gauge field the theory has an AdS_4 vacuum with radius l. This is a simple generalisation of pure Einstein-Maxwell but, as we shall see, the response to an external electric field contains important differences.

This chapter is organised as follows. In section two we construct the AdS soliton in the presence of an external static electric field for the theory with action (5.5). Our analysis is numerical, so we can choose any functional form of the source C_a for the global current operator J_a on the boundary theory (with lower case latin indices running over the boundary coordinates). This simply translates into the choice of the non-normalizable mode of the bulk $U(1)$ gauge field A. The most natural

[1] In the notation of [37] we set $\Phi_1 = \Phi$, $\Phi_2 = \Phi_3 = 0$, $A = A_1 = -A_2$ and $A_3 = A_4 = 0$.

thing to do is to decompose the electrostatic potential $C_t = C_t(\theta, \phi)$ in S^2 scalar harmonics. As in [38], we shall consider for simplicity the AdS soliton for the particular case of a dipolar potential

$$C_t(\theta) = \mathcal{E} \cos\theta \,. \tag{5.6}$$

For this theory we find that indeed there is a maximal allowed electric field. Then, in section three, we find the polarised neutral black hole for this theory subject to the same external electric field. Section four starts with the gravitational thermodynamics, leading to the construction of the phase diagram for the ABJM theory at strong coupling. We then consider the free ABJM theory subject to the external electrostatic potential (5.6). We see that at zero coupling the theory exhibits a behaviour qualitatively similar to the gravity description. We conclude in section five. In the appendix B we present the perturbative analytical result of a small electric field in AdS which matches our numerical result to a very good approximation.

5.2 AdS Soliton

The equations of motion that follow from the action (5.5) are

$$\begin{aligned} &R_{\mu\nu} + \frac{1}{l^2}(\cosh\Phi + 2) g_{\mu\nu} - \frac{1}{2}\nabla_\mu\Phi\nabla_\nu\Phi + e^{\Phi}\left(\frac{1}{4}F^2 g_{\mu\nu} - F_{\mu\alpha}F_{\nu}{}^{\alpha}\right) = 0\,, \\ &d\left(e^{\Phi} \star F\right) = 0\,, \qquad \nabla^2\Phi + \frac{2}{l^2}\sinh\Phi - \frac{1}{2}e^{\Phi}F^2 = 0\,. \end{aligned} \tag{5.7}$$

Notice that once we turn on an external electric field, setting $\Phi = 0$ is not consistent. For the simple form of the source (5.6) at the AdS boundary we can consider the axially-symmetric ansatz (setting the AdS radius $l = 1$)

$$\begin{aligned} ds^2 = &\frac{1}{(1-r^2)^2}\left(A(r,\theta) f(r)\, d\tau^2 + \frac{\left(1+r^2\right)^2 G(r,\theta)}{f(r)}\, dr^2\right) \\ &+ r^2\left(C(r,\theta)\left(d\theta + \frac{1}{r}H(r,\theta)\, dr\right)^2 + B(r,\theta)\sin^2\theta\, d\phi^2\right), \\ A_\tau = &\, ir D(r,\theta)\,, \qquad \Phi(r,\theta) = (1-r^2)\,\varphi(r,\theta)\,, \end{aligned} \tag{5.8}$$

where $f(r) = 1 - r^2 + r^4$ and r is a radial coordinate related to the radial coordinate of global AdS by $y = r/(1-r^2)$ and runs from $r = 0$ at the center of space, to $r = 1$ at the AdS boundary. This is precisely the ansatz 5.8 with the angular coordinate θ instead of x and the addition of a scalar

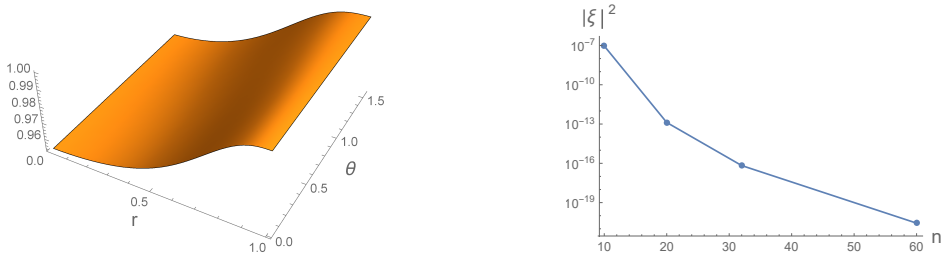

(a) (b)

Figure 5.1: (a) Metric function A for $\mathcal{E} = 1$ and a numerical grid of 60×60 points. (b) A linear-log plot of the deTurck vector norm, a measure of convergence, as a function of the number of gridpoints n.

field. Global AdS now corresponds to $A = G = B = C = 1$ and $H = D = \varphi = 0$. Again, we will turn on the gauge field by a dipolar potential at the boundary.

$$D(1, \theta) = \mathcal{E} \cos\theta \,, \tag{5.9}$$

The boundary conditions of the metric functions are the same as for the previous example without a scalar. The scalar field φ is symmetric about $r = 0$ and has the symmetry properties of a scalar on the S^2. As such, it is symmetric about $\theta = \pi/2$ and $\theta = 0$. With the above ansatz, the scalar field goes to zero at the AdS boundary.

Finally we need to impose the boundary condition to the scalar field Φ. From (5.5) it is simple to see that this field has $m^2 = -2$, corresponding for the ABJM theory to a dual operator of dimension $\Delta = 1$ [39]. We must choose a boundary condition to ensure that the non-normalizable mode corresponding to turning on a source for this operator at the boundary is zero, leaving only its VEV to be determined by the equations of motion. This corresponds to setting the second radial derivative, in Fefferman-Graham coordinates, of the scalar field to zero. In our ansatz, this becomes

$$\varphi(1, \theta) + \partial_r \varphi(r, \theta)\big|_{r=1} = 0 \,. \tag{5.10}$$

We will solve the harmonic Einstein equations of motion for this ansatz using the deTurck trick for gauge fixing the Einstein equations.

5.2.1 Results

In figure 5.1(a) we show the function A of the ansatz (5.8) for a value of the electric field $\mathcal{E} = 1$. A good measure of convergence when solving the Harmonic Einstein equations is the norm of the deTurck vector ξ. This is plotted in figure 5.1(b) as a function of n for $\mathcal{E} = 1$. The results have new features when compared to the scalar-free case described in [38], with the notable difference that we now find a maximum allowed value of the electric field at $\mathcal{E}_c^{Sol} = 2.101$, beyond which this soliton solution does not exist. This maximum value is where two branches of the solution meet. This can be seen by calculating several boundary observables, including the charge density $\rho(\theta)$, which can be written as

$$\frac{1}{4\pi G_N}\left(e^{\Phi} \star F\right)\Big|_{r=1} = \rho(\theta)\, d\Omega_2\,, \tag{5.11}$$

where $d\Omega_2$ is the volume form on the unit S^2. This charge density is plotted in figure 5.2a for several values of the electric field magnitude. The blue curves correspond to the first branch of soliton solutions up to the maximum value $\mathcal{E}_c^{Sol}$, while the purple curves correspond to decreasing the electric field from that maximum. The black curve corresponds to the maximum value of the electric field, and the opacity the curves are is proportional to the value of the electric field. We will use this key in all plots of the AdS soliton that follow. In all cases, the charge density is maximal at the pole and vanishes at the equator, as expected from the choice of boundary condition. The total charge in one hemisphere at infinity is also plotted in figure 5.2b. Here we see a qualitative

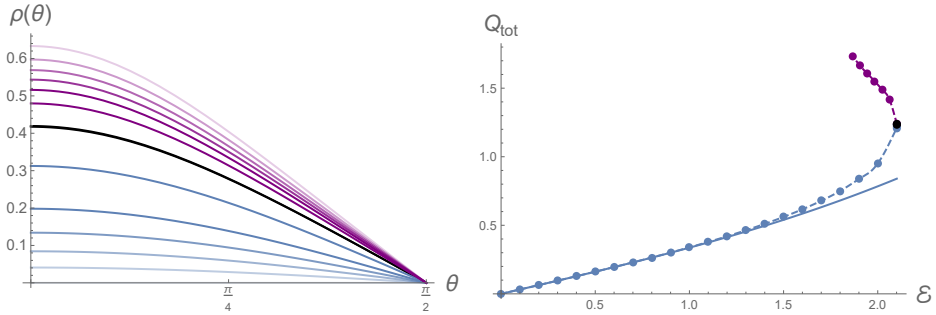

(a) (b)

Figure 5.2: (a) The charge density and (b) the total charge on the AdS boundary for several values of $\mathcal{E} \in \left[0, \mathcal{E}_c^{Sol}\right]$ with G_N set to one. Blue and purple correspond to the two branches of the soliton, with the maximum value of the electric field shown in black. The solid curve in (b) represents the analytical perturbative result in $\mathcal{E}$, as derived in appendix B.

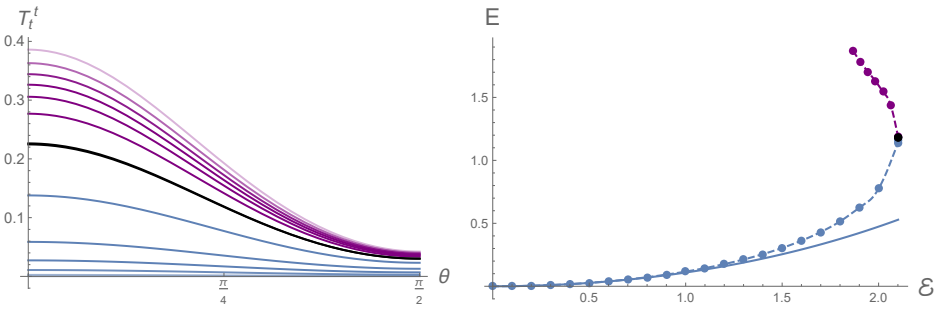

(a) (b)

Figure 5.3: (a) Energy density on the AdS boundary and (b) total energy of the boundary theory as a function of the electric field $\mathcal{E}$ (setting $G_N = 1$). The solid curve in (b) is the analytical result found from perturbation theory around $\mathcal{E} = 0$ from appendix B.

difference between the two branches related to the electric field. The total charge increases with the electric field up to the maximum, then decreases along the second branch of solutions.

We can also compute the stress tensor of the boundary field theory. For this we need to consider the total action $S = S_{bulk} + S_{bdy} + S_{CT}$, where S_{bulk} is given by (5.5) and S_{bdy} is the Gibbons-Hawking-York term and the counter term action is

$$S_{CT} = -\frac{1}{8\pi G_N}\int_{\partial M} d^3x\sqrt{\gamma}\left(1 - \frac{l^2}{12}R + \frac{1}{4}\Phi^2\right). \tag{5.12}$$

The stress tensor derived from the renormalized action with $l = 1$ is

$$T_{\mu\nu} = \frac{2}{\sqrt{\gamma}}\frac{\delta S}{\delta h^{\mu\nu}} = \frac{1}{8\pi G_N}\left(K_{\mu\nu} - K\,\gamma_{\mu\nu} + G_{\mu\nu} - 2\gamma_{\mu\nu} - \frac{1}{4}\Phi^2\gamma_{\mu\nu}\right). \tag{5.13}$$

Expanding the metric functions in a Fefferman-Graham-like expansion at the boundary, we can again write the stress tensor in terms of normalizable modes of the metric functions. The energy density is

$$T_t^t = \frac{3}{256\pi G_N}\left(2\alpha_3 + \phi_0^2\right), \tag{5.14}$$

where ϕ_0 is φ evaluated at the boundary, that is, $\phi_0(\theta) = \varphi(1,\theta)$. This is plotted in figure 5.3a. Like the charge density, T_t^t is maximal at the pole and minimal at the equator. For the first branch of solutions it increases for increasing $\mathcal{E}$, while the other branch has the opposite behavior. In figure 5.3b we plot, as a function of $\mathcal{E}$, the boundary theory total energy

$$E = \int d\Omega_2 T_t^t\,. \tag{5.15}$$

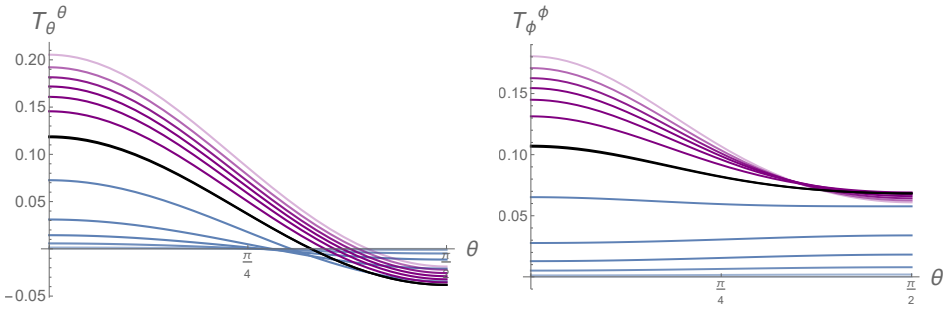

(a) (b)

Figure 5.4: Spatial components of the boundary stress tensor for $\mathcal{E} \in [0, \mathcal{E}_c^{sol}]$. We set $G_N = 1$.

The slope of the energy curve becomes singular at the maximum value of the electric field, where the two branches meet. The spatial components of the stress tensor are

$$\begin{aligned} T_\theta^\theta &= \frac{3}{256\pi G_N}\left(2\chi_3 + \phi_0^2\right), \\ T_\phi^\phi &= \frac{-3}{128\pi G_N}\left(\chi_3 + \alpha_3 + \phi_0^2\right), \end{aligned} \tag{5.16}$$

where $\chi_3(\theta)$ is the third-order radial power-law mode for the metric function $C(r,\theta)$. If we think of the stress tensor as describing a fluid of the boundary theory, the $\theta\theta$ component, plotted in figure 5.4a, shows that the pressure along θ is positive up to a critical point dependent on $\mathcal{E}$ and negative thereafter. Since there is no net flow of momenta in the ϕ direction, the $\phi\phi$ component, which measures the pressure along that direction, is independent of ϕ. This is plotted in figure 5.4b, and decreases from the poles to the equator. These are the only non-zero components of the stress tensor, which is traceless, as can be seen from the expressions written above.

As a consequence of the Ward identities, the equation governing the conservation of energy and momentum in a background electric field is

$$\nabla_a T^{ab} + \frac{1}{2} J_a F^{ab} = 0\,, \tag{5.17}$$

where $J^a = (\rho, J^i)$ and J^i is the current density on the sphere at the boundary. The only nontrivial component in this ansatz corresponds to $b = \theta$ and leads to the expression

$$\partial_\theta\left(\sin\theta\, T_\theta^\theta\right) - \cos\theta\, T_\phi^\phi = -\frac{\mathcal{E}}{2}\rho(\theta)\sin^2\theta\,. \tag{5.18}$$

Our numerical solutions satisfy this equation to within a precision of 10^{-2} relative to T_ϕ^ϕ.

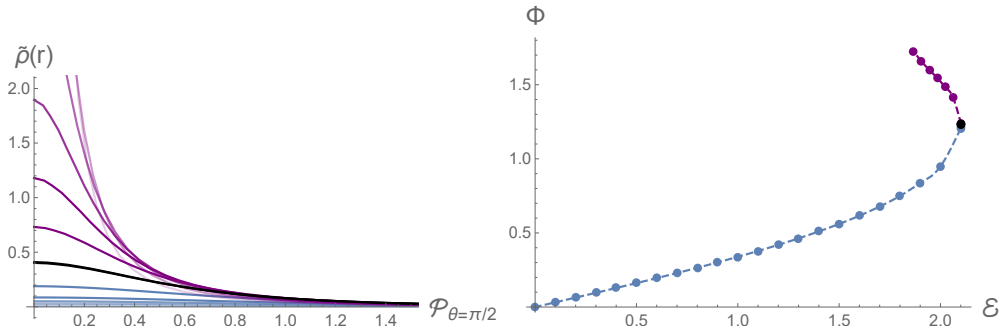

(a) (b)

Figure 5.5: (a) The flux density through the equatorial plane as a function of the proper distance for several values of the electric field. (b) Total flux through the equator.

There are also several bulk observables that will allow us to develop intuition of the AdS geometry. The flux density $\widetilde{\rho}$ through the $\theta = \pi/2$ plane is defined by

$$\frac{1}{4\pi G_N} \star \left(e^{\Phi(r,\theta)} F \right) \Big|_{\theta=\pi/2} = \widetilde{\rho}(r) \sqrt{g_{rr} g_{\phi\phi}}\, dr \wedge d\phi \,. \tag{5.19}$$

This is greatest at the origin and goes to zero at $r = 1$. The flux density in terms of the proper radial distance 4.20 from the AdS center along the equatorial plane is plotted in figure 5.5a. Darker curves correspond to higher values of the electric field. The total flux through the equator is plotted in figure 5.5b. By conservation, the total flux through the equatorial plane should be equal to the total charge at one hemisphere. We have checked that this is true with an error of 10^{-3}. The flux increases up to the maximum electric field and then keeps growing in the other branch of the solution, as the electric field decreases to another critical value.

The value of φ at the AdS center is plotted in figure 5.6a and the metric component $g_{\tau\tau}$ in figure 5.6b. The two branches are marked in blue and purple, respectively, and in both plots these meet at a maximum allowed electric field. The fact that the $g_{\tau\tau}$ metric component tends to zero at some value of $\mathcal{E}$ could mean that a horizon develops at the origin when the electric field for the second soliton branch is reaches a minimum. However, the Kretschman curvature invariant $K = R_{\mu\nu\rho\sigma} R^{\mu\nu\rho\sigma}$ blows up at this value of the electric field, therefore a singularity will form at this point. The Kretschman curvature at the origin is plotted in figure 5.7 as a function of $\mathcal{E}$.

5.3 Black Hole

Next we construct the solution describing a polarized black hole in this background. The Ansatz is the same as in 6.3 with the addition of a scalar field

$$\Phi(r,\theta) = (1-r^2)\varphi(r,\theta) \tag{5.20}$$

as for the AdS soliton. Recall that the radial coordinate r runs from the black hole horizon at $r=0$ to the AdS boundary at $r=1$. In these coordinates, the boundary condition for the scalar field at $r=1$ corresponding to the $\Delta=1$ operator is

$$\partial_r \varphi(r,\theta)\big|_{r=1} = 0\,. \tag{5.21}$$

Again, for the gauge field we require a dipolar potential as for the soliton, imposing condition (5.9). Thus the AdS soliton and black hole solutions have the same asymptotics, and we will have thermodynamically competing solutions.

5.3.1 Results

Figure 5.8(a) shows the ansatz function A for a value of temperature and electric field. A linear-logarithmic plots of the deTurck vector norm as a function of the number of grid points n is plotted in figure 5.8(b).

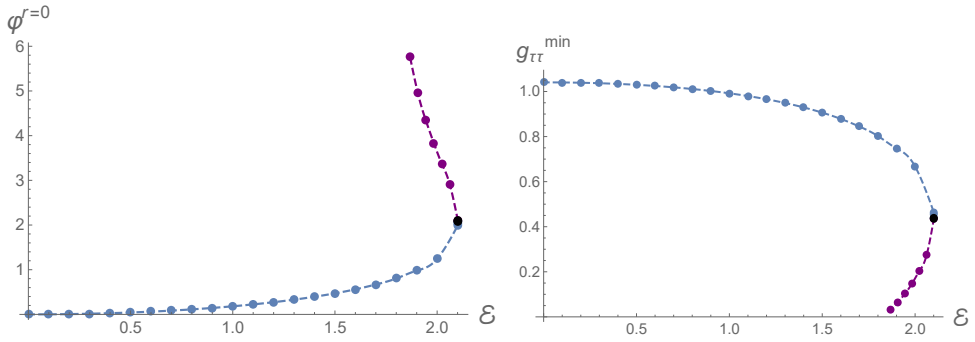

(a) (b)

Figure 5.6: (a) The value of φ at the AdS center and (b) the tt component of the metric up to maximum value of $\mathcal{E}$ for the two branches of the AdS soliton, denoted in blue and purple, respectively.

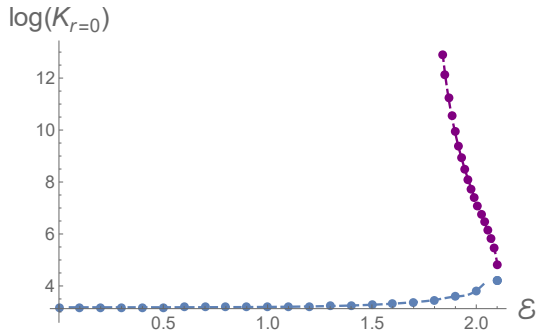

Figure 5.7: A log plot of the Kretschman invariant at the origin $r = 0$.

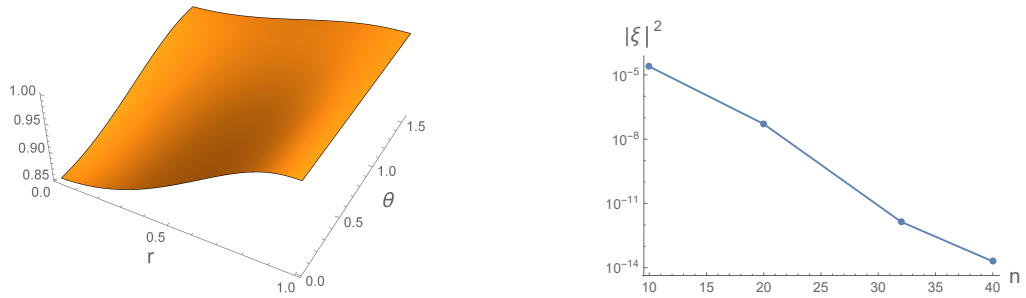

(a) (b)

Figure 5.8: (a) Examples of numerical solutions for the metric function A of a large polarised black hole for an electric field $\mathcal{E} = 1$ and temperature $T = 1/\pi$ for a numerical grid of 40×40 points.(b) Plot of convergence for the polarised black hole for a value of the electric field $\mathcal{E} = 1$ and temperature $T = 1/\pi$.

For a given temperature there will be four branches of solutions. Two are analogous to the so-called large and small black holes of Schwarzscild-AdS without a scalar or a source, so we will refer to these solutions as "L1" and "S1" black holes. These solution are continuously connected to the large and small black holes of Schwarzscild-AdS by turning off the external electric field. In the case of black holes in AdS with an electric field but no scalar, as discussed in [38], the large and small black hole branches connect at a minimum value of the temperature that depends on the electric field, which can be made arbitrarily large. No solutions exist at temperatures below these minimum values. The same behaviour occurs in the presence of the scalar fields, however now there is a maximum value allowed for the electric field on the AdS black hole geometry that changes itself with temperature. This gives another degenerate point at which the large and small black holes branch again. We will call these branches the "L2" and "S2" black holes.

Figure 5.9 shows the area of the horizon by way of the Bekenstein-Hawking entropy

$$S = \frac{\mathcal{A}}{4G_N} = \frac{\pi y_0^2}{G_N} \int_0^{\frac{\pi}{2}} d\theta \, \sin\theta \sqrt{C(0,\theta)B(0,\theta)}\,, \tag{5.22}$$

of the four black hole branches as a function of the electric field, for three values of the temperature that decreases in the plots from left to right. In this plot and those that follow, the blue, red, gray, and orange curves correspond to the L1, S1, L2, and S2 branches, respectively. The maximum value of $\mathcal{E}$ increases as the temperature increases. For low enough temperatures, below the minimal value allowed for AdS-Schwarzschild black holes, black holes only exist above a minimal value of $\mathcal{E}$.

Before looking at plots of other observables, it is useful to spend some time discussing the space of solutions. In figure 5.10, we plot the extremal values of $\mathcal{E}, T$ for the L1, L2, S1, and S2 black hole branches drawn as blue, gray, red, and orange curves, respectively. We see that each curve has a minimum and maximum value of the electric field that depends on the temperature. For small $\mathcal{E}$, the L1 and S1 black holes have the same minima, as we expect from AdS-Schwarzschild. Around $\mathcal{E} = 2$, there are four black hole solutions. The electric field minima for the S2 and L2 fall along the same curve, with any discrepancies in this plot arising from the numerical difficulty in finding S2 black hole solutions for a certain range in temperatures. The plot also shows that the maxima for the L1 and L2, as well as S1 and S2, branches follow the same respective curves. Notice that below a certain temperature we do not find any black holes solution, irrespectively of the value of the electric field.

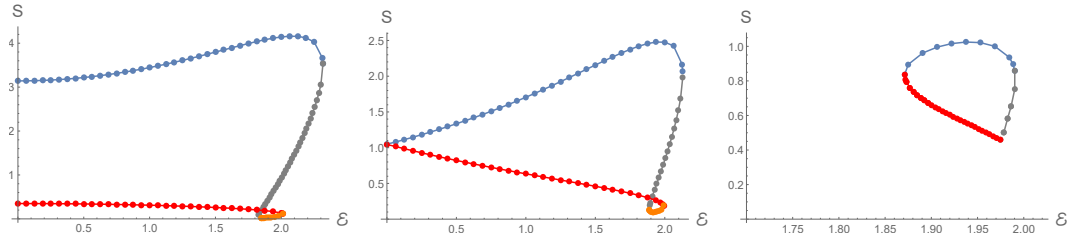

(a) (b) (c)

Figure 5.9: Black hole entropy as function of the electric field for $T = 1/\pi$, $T = 0.275665$ and $T = 0.24179$ ($G_N = 1$). Plot (b) is for a temperature slightly above the minimal value allowed for AdS-Schwarzschild black holes, where the large and small black hole branches meet. Below this temperature neutral black holes only exist for a non-zero electric field.

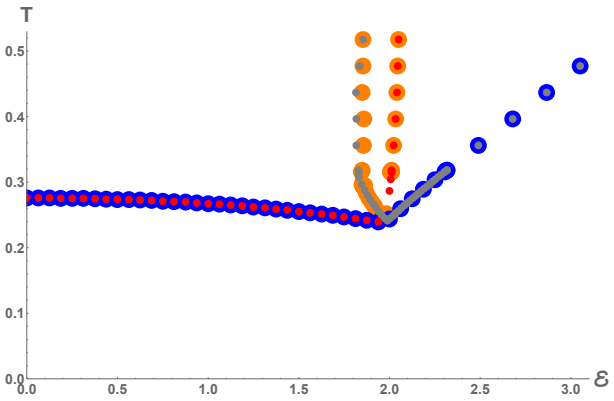

Figure 5.10: The minimum temperatures of the L1 (blue), S1 (red), L2 (gray), and S2 (orange) curves as a function of $\mathcal{E}$.

By computing isometric embeddings of the horizon geometry in Euclidean space, we can monitor the shape of the horizon. These are plotted in figure 5.11 for the four black hole branches at a fixed temperature of $T = 1/\pi$. In (a), the L1 and L2 black holes are plotted in blue and gray, respectively. In (b), the S1 curve is red and the S2 curve orange. More transparent curves correspond to larger values of the electric field with the faintest curves of L1 and L2 or S1 and S2 corresponding to the same value of $\mathcal{E}$. We can see that the black holes have the same shape when these branches meet at the extremal values of the electric field. These plots can be summarized by looking at the ratio of the horizon circumference at the equator to that of a meridian, as shown in figure 5.12. The L1 and S1 black holes start as round spheres at $\mathcal{E} = 0$, after which the L1 black hole deforms much

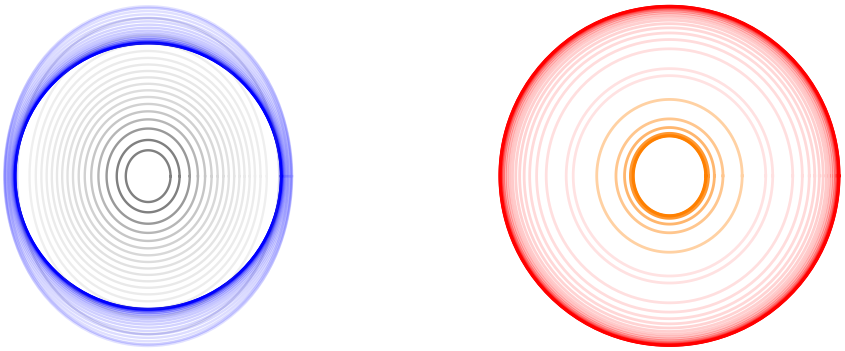

(a) (b)

Figure 5.11: Isometric embeddings of black hole horizons at fixed $T = 1/\pi$. The curves for the L1, L2, S1, and S2 black holes are blue, gray, red, and orange, respectively.

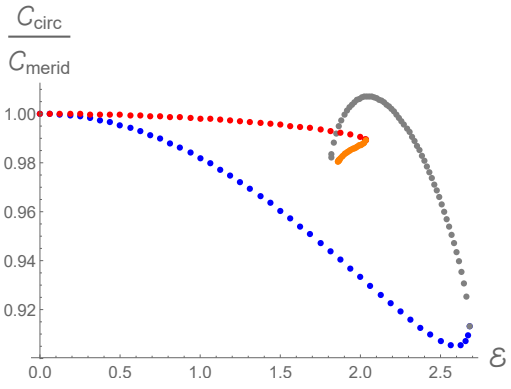

(a)

Figure 5.12: The ratio of the circumferences at the horizon equator and a meridian at fixed $T = .396$.

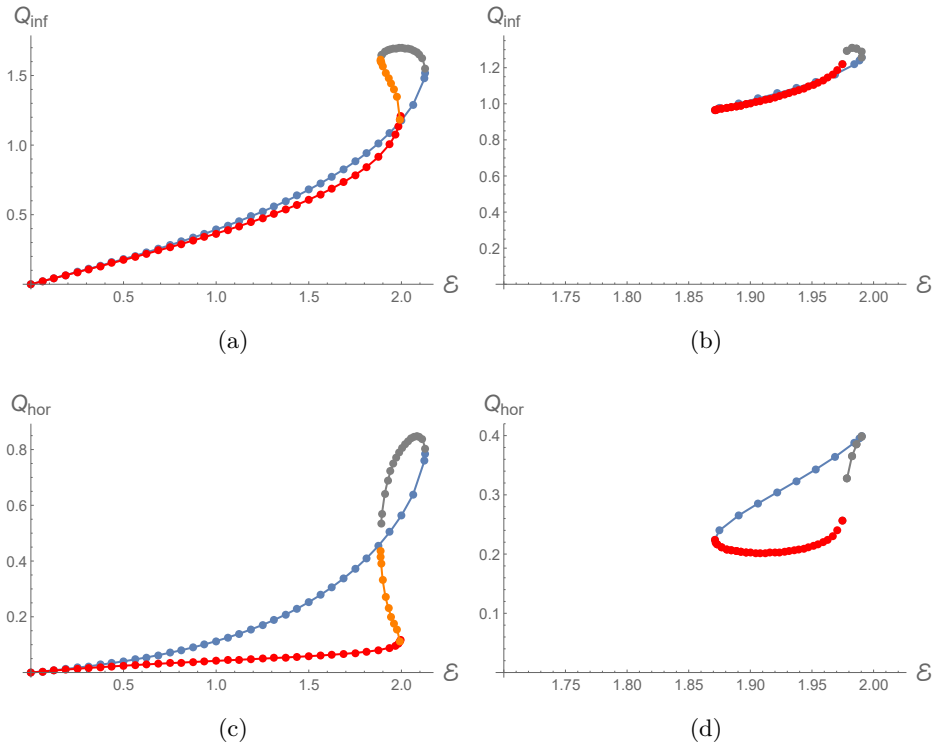

(a) (b)

(c) (d)

Figure 5.13: (a)-(b) Total charge in one hemisphere at the AdS boundary; (c)-(d) and at the black hole for $G_N = 1$. The first column is at $T = 0.275665$ and the second at $T = 0.24179$.

more than the S1 black hole. The L1 and L2 curves meet at the maximum value of $\mathcal{E}$, and the L2 black hole also deforms much more than the S2 curve.

As the electric field is increased, the black holes becomes slightly deformed but do not pinch at the equator as in [38]. This is one of the main qualitative differences from coupling the polarized

black holes to a scalar field.

In contrast to the AdS soliton, the black hole has two surfaces which accumulate charge: the boundary and the horizon. We can therefore look at the total charge contained in one hemisphere, by integrating the electric flux through each of these surfaces as defined in (5.11). Figures 5.13a and 5.13b show the total boundary charge for two values of the temperature, while figures 5.13c and 5.13d show the total charge in one hemisphere of the black hole horizon for the same two values of temperature. In this case, conservation of charge requires that the difference between the hemispherical charges at the boundary and horizon is equal to the electric flux (5.19) through the equator. We checked that this is true to within 10^{-4}.

The value of the scalar field at the pole of the horizon is shown in figure 5.14. It shows that while the value doesn't change much with temperature, the maximum electric field allowed at that temperature for the large black hole branch, which is the right-most curve on the plot, does.

The non-vanishing components of the boundary energy-momentum tensor of the dual to the black hole geometry are

$$\begin{aligned} T^{\tau}_{\tau} &= \frac{-y_0}{256\pi G_N}\left(16(1+Q^2+y_0^2)-y_0^2\left(6\alpha_3-3\phi_0^2\right)\right), \\ T^{\theta}_{\theta} &= \frac{y_0}{256\pi G_N}\left(16(1+Q^2+y_0^2)+y_0^2\left(6\chi_3-3\phi_0^2\right)\right), \\ T^{\phi}_{\phi} &= \frac{y_0}{128\pi G_N}\left(8(1+Q^2+y_0^2)-3y_0^2\left(\alpha_3+\chi_3-\phi_0^2\right)\right), \end{aligned} \tag{5.23}$$

where, as before, α_i, χ_i, and ϕ_i are the i-th order power-law modes associated to the functions A, C, and φ, respectively. Angular profiles for each component are plotted in figure 5.15 for the large black hole at several values of electric field magnitude and temperature. Above $\mathcal{E}=0$, the energy

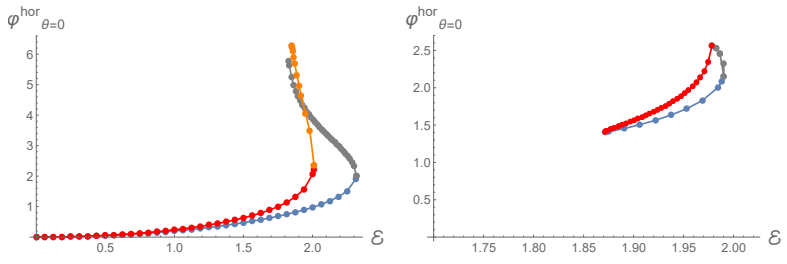

(a) (b)

Figure 5.14: The value of the scalar field at the horizon for $T = 1/\pi$ and $T = 0.24179$, from left to right.

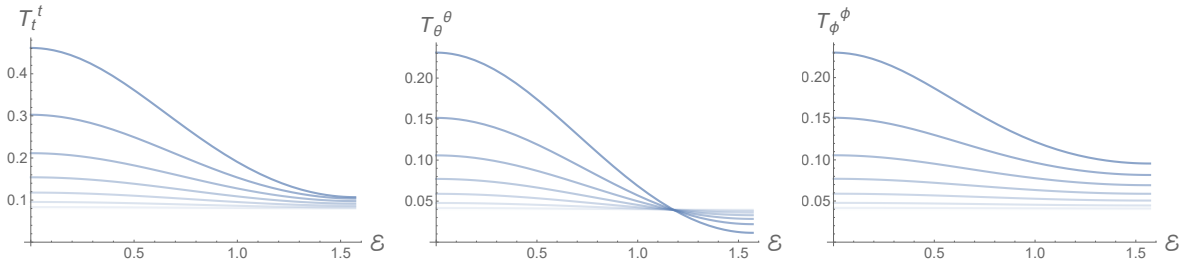

(a) (b) (c)

Figure 5.15: (a) Boundary energy density, (b) the $\theta\theta$ component and (c) the $\phi\phi$ component of the boundary stress tensor at $T = 1/\pi$. Fainter curves correspond to lower values of the electric field. (Setting $G_N = 1$.)

density and spatial components of the stress tensor are all maximal at the pole and minimal at the equator, as for the AdS soliton. The only qualitative difference is that the $T_{\theta\theta}$ component does not becomes negative for the large black hole. This means that there is no expansion in the fluid on the boundary around the equator, as for the AdS soliton case and the polarized black holes described in [38]. We also checked that our numerical solutions obey the conservation equation (5.18) with a 1% precision with respect to T^ϕ_ϕ.

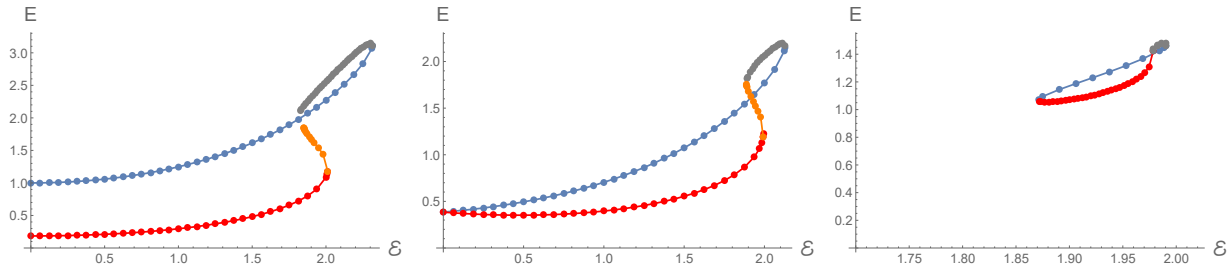

(a) (b) (c)

Figure 5.16: Total energy at the boundary for the dual state of the black hole for $G_N = 1$ at $T = 1/\pi$, $T = 0.275665$ and $T = 0.24179$ from left to right.

By integrating the energy density we obtain the total energy measured at infinity. This is plotted in figure 5.16.

5.4 Thermodynamics

Defined with Euclidean signature, the AdS soliton and black hole geometries of the previous two sections are already primed to study the thermodynamic properties of the boundary theory. The black hole geometries correspond to phases that depend on electric field magnitude, and on temperature that fixes the periodicity of the thermal circle, so that the solutions are regular at the Euclidean horizon. The soliton solution exists for any temperature and depends only on $\mathcal{E}$. These phases are in thermodynamic competition with each other, and by comparing their free energies we will be able to draw the corresponding phase diagram.

The Gibbs free energy associated to a geometry with a dipolar electrostatic source at the boundary is

$$\mathcal{G} = E - TS - \pi \int_0^\pi d\theta \sin\theta \, \rho(\theta) \, \mathcal{E} \cos\theta \,, \tag{5.24}$$

where E is the energy, S is the Bekenstein-Hawking entropy and $\rho(\theta)$ is the charge density at the boundary. For the AdS soliton solutions without horizon, the entropy term vanishes and the free energy is independent of the temperature. The free energy is shown in figure 5.17. The L1, L2, S1, and S2 black holes are depicted by blue, gray, red, and orange curves, respectively. The two soliton branches are shown by black and purple dotted lines. It is clear from these plots that the L1 and black soliton branches are the two with lowest free energy and are therefore the only two that matter for the phase diagram. We will therefore restrict our attention to these phases.

Below the maximum value of the electric field for the soliton $\mathcal{E}_c^{Sol}$, the phase transition occurs when the blue and black curves of figure 5.17 cross. This begins with the Hawking-Page phase transition at $T = 1/\pi$ for $\mathcal{E} = 0$ and $T_c(\mathcal{E})$ decreases with $\mathcal{E}$ until $\mathcal{E} = \mathcal{E}_c^{Sol}$. Beyond this value, the L1 black hole is the black hole phase with lowest free energy, and no soliton solution exists. These results are summarised in the phase diagram of figure 5.18. The blue region corresponds to the black hole phase while the red region corresponds to the AdS soliton phase. The solid blue line marks the phase transition up to $\mathcal{E}_c^{Sol}$, shown here as a vertical gray line. The blue dashed curve shows the minimum temperature for the L1 black hole as a function of the electric field. The black hole phase technically exists and is thermodynamically stable for $T > T_{min}$, even for $\mathcal{E}$ greater than the maximum value for the soliton. The situation is very similar to the case of charged black holes dual to SYM with an R-charge chemical potential [40]. We expect that the black holes are metastable for $\mathcal{E} > \mathcal{E}_c^{Sol}$ and that strictly speaking the canonical ensemble is only well defined for

$\mathcal{E} < \mathcal{E}_c^{Sol}$. This phase diagram is qualitatively similar to those produced in [41] for the case of spherically symmetric Einstein-Maxwell-dilaton gravity in global AdS.

In order to verify our numerical solutions, we can derive a first law of thermodynamics that encodes the conservation of energy of the black hole and soliton systems. For the soliton, the energy responds to small changes in $\mathcal{E}$. We have

$$\delta_{\mathcal{E}} E - \pi\, \mathcal{E} \int_0^{\pi} d\theta \sin\theta\, \cos\theta\, \delta_{\mathcal{E}} \rho(\theta) = 0\,. \tag{5.25}$$

This is satisfied to 10^{-2} on our numerical solutions and analytically to fourth order in $\mathcal{E}$. For

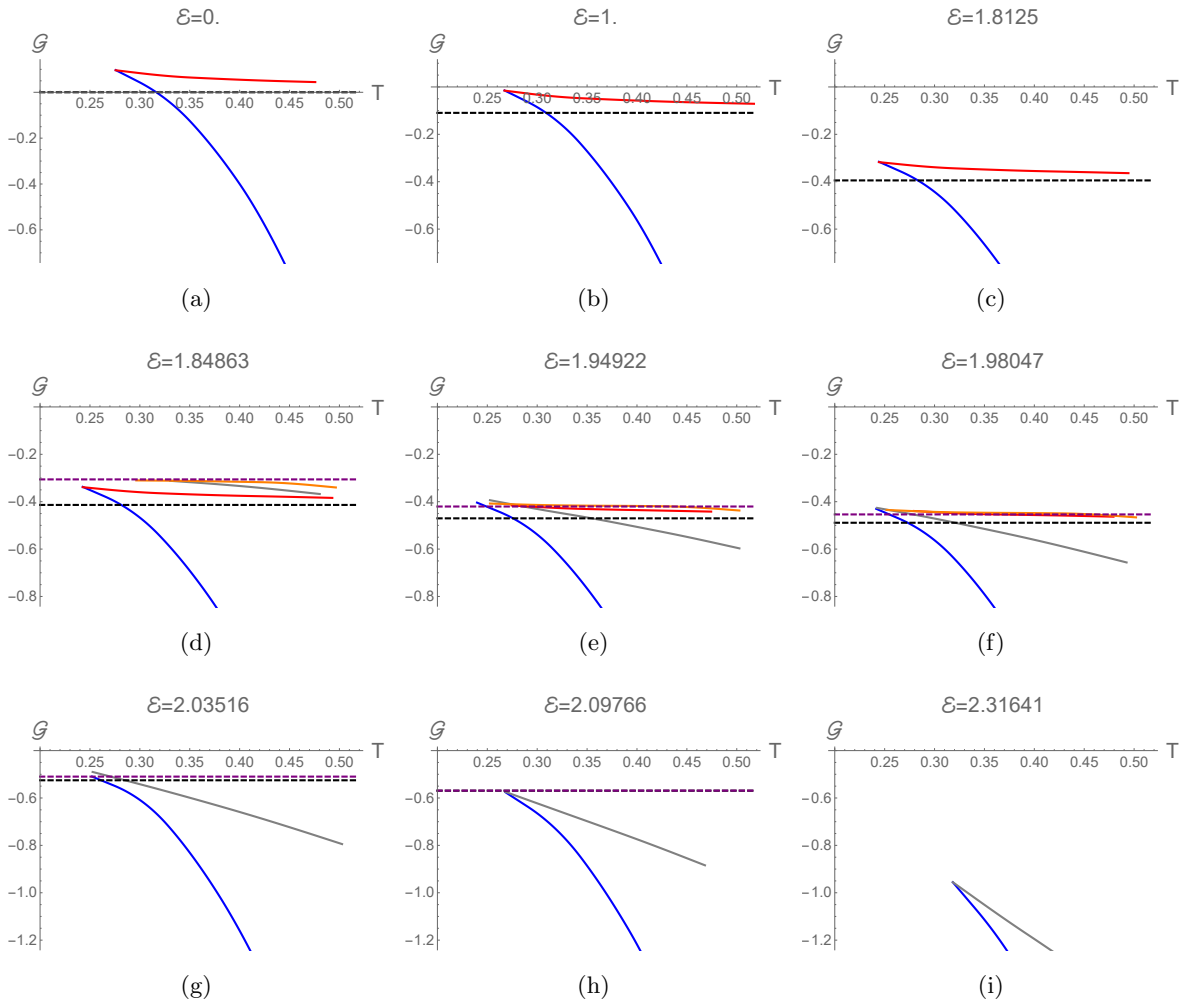

Figure 5.17: Gibbs free energy for L1, L2, S1, and S2 black hole branches (blue, gray, red, and orange curves), and AdS soliton (black and purple dashed line) for several values of the electric field as a function of the temperature. In these plots we set $G_N = 1$.

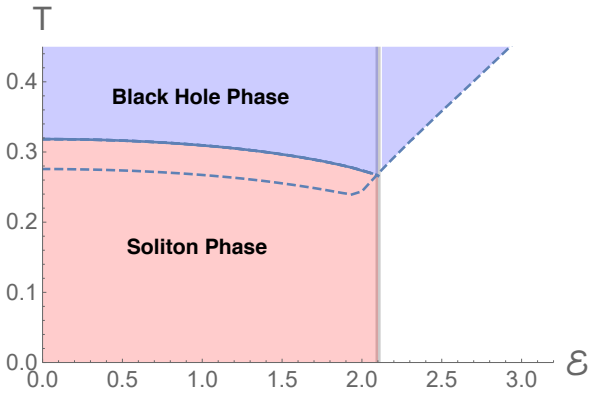

Figure 5.18: Phase diagram with the critical temperature (solid blue curve) above which the black hole phase is thermodynamically favoured. The dashed line shows the minimum temperature of the L1 black hole, and the vertical gray line marks the maximum electric field for the soliton.

the black hole, the energy at infinity, entropy, and charge density all respond to variation in the temperature. At fixed electric field, the first law for the black hole can be written

$$\delta_T E - T\delta_T S - \pi\,\mathcal{E}\int_0^\pi d\theta \sin\theta\,\cos\theta\,\delta_T\rho(\theta) = 0\,. \tag{5.26}$$

This is also satisfied to 10^{-2} on our numerical solutions.

5.4.1 Free ABJM with external electric field

The ABJM theory has global $SU(4)\times U(1)$ R-symmetry, which is dual to a local symmetry in the gravity description. The truncation of this gravity theory to $U(1)^4$ considers the three $U(1)$'s inside the $SU(4)$. In particular, the $U(1)$ gauge field that we turned on in the bulk is dual to a global current associated to one of the $U(1)$'s of the $SU(4)$ R-symmetry. To understand the effect of turning on a source for this $U(1)$ global current, recall that the ABJM theory has four complex scalars and four Majorana spinors, which transform in the fundamental of the $SU(4)$ R-symmetry. Our choice of $U(1)$ corresponds to the generator $Q = \mathrm{diag}(1,-1,0,0)$ of $SU(4)$. Thus we have one scalar and one fermion with charge $+1$, one scalar and one fermion with charge -1, two neutral scalars and two neutral fermions. We conclude that, at zero coupling and finite external source, the problem of computing the partition functions reduces to that of analysing one complex scalar field and one Majorana fermion with conformal coupling on $\mathbb{R}\times S^2$, minimally coupled to

the external electric field. The full partition function can then be computed by considering the others scalars and fermions that do not couple to the electric field and by considering that all fields are in the fundamental times anti-fundamental of the gauge symmetry $U(N) \times U(N)$. Then, the gauge-invariant states can be written as products of traces of products of pairs of elementary fields.

The single particle states of a charged scalar on the two-sphere in the presence of the dipolar electrostatic potential were computed in section 4.6. Using a basis of spherical harmonics the hamiltonian is diagonal in the azimuthal quantum number m but it becomes an infinite tridiagonal matrix in the quantum number $l \geq |m|$,

$$\langle l', m'|H|l, m\rangle = \delta_{m,m'} \left\{ \delta_{l,l'} \left(l + \frac{1}{2} \right) + \mathcal{E} \left[\delta_{l,l'-1} \sqrt{\frac{(l+1-m)(l+1+m)}{(2l+1)(2l+3)}} + (l \leftrightarrow l') \right] \right\}. \quad (5.27)$$

We shall now study the case of a free charged fermion on a two sphere with a dipolar potential, following the logic of [42]. The Dirac equation reads

$$\left(i\widehat{\nabla} - M \right) \psi = \left(i e_a^\alpha \gamma^a \Big(D_\alpha + \frac{i}{4} \omega_\alpha^{ij} \sigma_{ij} \Big) - M \right) \psi = 0 \,, \quad (5.28)$$

where $e_a^\alpha = \mathrm{Diag}\,(1, 1, 1/\sin\theta)$ is the zweibein on the two-sphere and ω is the spin connection. Here the covariant derivative includes the gauge field as $D_\alpha = \partial_\alpha - iC_\alpha$. The irreducible representation of Majorana spinors in $SO(1,2)$ is two-dimensional, so the γ-matrices reduce to Pauli matrices. With Lorentzian $(-,+,+)$ signature, we choose ($\{\gamma^a, \gamma^b\} = 2\eta^{ab}$)

$$\gamma^0 = i\sigma_3 \,, \quad \gamma^1 = \sigma_1 \,, \quad \gamma^2 = \sigma_2 \,, \quad (5.29)$$

$$\sigma_{ab} = -\frac{i}{2} \Big[\gamma^a, \gamma^b \Big] \,, \quad (5.30)$$

and we use latin indices in the tangent space.

Next we consider the particular case of an external electric field for which $C = \mathcal{E} \cos\theta dt$. In this case the Dirac operator becomes

$$\widehat{\nabla} = \gamma^0 \left(\partial_t - i\mathcal{E} \cos\theta \right) + \gamma^1 \left(\partial_\theta + \frac{\cos\theta}{2\sin\theta} \right) + \frac{\gamma^2}{\sin\theta} \, \partial_\phi \,. \quad (5.31)$$

Doing the usual Fourier decomposition of the spinor components

$$\psi = e^{-i(\omega t - m\phi)} \begin{pmatrix} \psi_+ \\ \psi_- \end{pmatrix} , \quad (5.32)$$

for a half integer m and where $\psi_\pm$ are functions of θ, the Dirac equation (5.28) becomes

$$\big(M \mp i(\omega + \mathcal{E} \cos\theta) \big) \psi_\pm = i \left(\partial_\theta + \frac{\cos\theta \pm 2m}{2\sin\theta} \right) \psi_\mp \,. \quad (5.33)$$

As usual, it is convenient to square the Dirac equation by multiplying (5.28) by $(i\widehat{\nabla} + M)$. This looks like a Klein Gordon equation $(\widehat{\nabla}^2 + M^2)\psi = 0$, with

$$\widehat{\nabla}^2 = (\omega + \mathcal{E}\cos\theta)^2 + i\gamma^2\mathcal{E}\sin\theta + \frac{1}{\sin\theta}\left(\partial_\theta \sin\theta \partial_\theta\right) - \frac{1}{4} - \frac{1}{4\sin^2\theta}\left(1 + 4m^2 + i\gamma^0 4m\cos\theta\right). \quad (5.34)$$

Notice that the second term in this operator has a γ^2 matrix and therefore is not diagonal.

Let us first consider the case of zero electric field. In this case the Klein-Gordon equation is diagonal. In terms of the coordinate $x = \cos\theta$, the functions $\psi_\pm(x)$ satisfy the differential equation

$$\left(\partial_x\left((1-x^2)\partial_x\right) - \frac{1}{4(1-x^2)}\left(1 + 4m^2 \mp 4mx\right) + \omega^2 + M^2 - \frac{1}{4}\right)\psi_\pm(x) = 0\,. \quad (5.35)$$

Notice that the equations for ψ_+ and ψ_- can be interchanged by sending $x \to -x$, and that equation (5.35) is singular at the poles $x = \pm 1$. After the redefinition

$$\psi_\pm = (1 \mp x)^{\frac{\alpha}{2}}(1 \pm x)^{\frac{\beta}{2}} Y_\pm\,, \quad (5.36)$$

with α and β greater than zero for regularity, the equation can be written in hypergeometric form

$$(1-x^2)Y_\pm'' + \big(\pm\,\mathrm{sgn}(m) - 2(1+|m|)x\big)Y_\pm' + l(l+2|m|+1)Y_\pm = 0\,, \quad (5.37)$$

for $\alpha = |m - 1/2|$, $\beta = |m + 1/2|$, and $\omega^2 + M^2 = (l + |m| + 1/2)^2$. Again, we will use the conformal value for the fermion mass, which is $M = 0$. The latter constraint on ω ensures the square integrability of solutions on the interval $x \in [-1, 1]$. Solutions to this equation are Jacobi polynomials of order $l \geq 0$

$$Y_+ = a_{l,m} P_l^{(\alpha,\beta)}(x)\,, \quad (5.38)$$

$$Y_- = b_{l,m} P_l^{(\beta,\alpha)}(x)\,, \quad (5.39)$$

where the coefficients $a_{l,m}$ and $b_{l,m}$ are related by the Dirac equation and fixed by the normalisation condition

$$\int_0^{2\pi} d\phi \int_{-1}^{1} dx\, \psi^\dagger\psi = 1\,. \quad (5.40)$$

This gives

$$b_{l,m} = -\mathrm{sgn}(m)\, a_{l,m} \quad |a_{l,m}| = \frac{\sqrt{l!\,\Gamma(l+2|m|+1)}}{2^{|m|+1}\sqrt{\pi}\,\Gamma\left(l+|m|+\frac{1}{2}\right)}. \quad (5.41)$$

We can now consider the Hamiltonian

$$\widehat{H} = i\partial_t = -\mathcal{E}x + i\gamma^0\widehat{\nabla}_{S^2} \quad (5.42)$$

where $\widehat{\nabla}_{S^2}$ is the Dirac operator on the two-sphere. The eigenvalues for this operator were found above, and are given by $\omega_{l,m} = l + |m| + 1/2$, with $l = 0, 1, 2, \ldots$ and $m \in \mathbb{Z} + 1/2$. On a energy eigenstate for zero electric field $\psi_{l,m}$, the Hamiltonian acts

$$\widehat{H}\psi_{l,m} = -\mathcal{E}x\,\psi_{l,m} + \omega_{l,m}\psi_{l,m}\,. \tag{5.43}$$

We can compute the matrix elements of $\widehat{H}$ in this basis

$$\langle l', m'|\widehat{H}|l, m\rangle = \int_0^{2\pi} d\phi \int_{-1}^{1} dx\, \psi^\dagger_{l',m'} \widehat{H}\psi_{l,m} \tag{5.44}$$

$$= \delta_{m,m'}\left[\omega_{l,m}\delta_{l,l'} - 2\pi\mathcal{E}\left(\frac{2^{2|m|}\Gamma\left(l+|m|+\frac{1}{2}\right)\Gamma\left(l+|m|+\frac{3}{2}\right)}{l!(2\,|m|+l)!(|m|+l+1)}\,\delta_{l',l+1}\right.\right. \tag{5.45}$$

$$\left.\left. + \frac{2^{2|m|}\Gamma\left(l+|m|-\frac{1}{2}\right)\Gamma\left(l+|m|+\frac{1}{2}\right)}{(l-1)!(2\,|m|+l-1)!(|m|+l)}\delta_{l',l-1}\right) a_{l,m}a_{l',m}\right], \tag{5.46}$$

which simplifies to

$$\langle l', m'|\widehat{H}|l, m\rangle = \delta_{m,m'}\left\{\delta_{l,l'}\left(l+|m|+\frac{1}{2}\right) - \mathcal{E}\left[\delta_{l,l'-1}\,\frac{\sqrt{(l+1)(l+2|m|+1)}}{2(l+|m|+1)} + (l \leftrightarrow l')\right]\right\}.$$

We denote the eigenvalues of this hamiltonian by $\omega^F_{m,k}(\mathcal{E})$ with $m \in \mathbb{Z}+1/2$ and $k = 1, 2, \ldots$. The resulting low energy spectra of the free boson for $m = 0$ and free fermion for $m = 1/2$ are shown in figure 5.19. Notice that in the bosonic sector, for $\mathcal{E} > \mathcal{E}^B_c \approx 1.3868$ the single particle ground state energy becomes negative, while for the fermion sector, this critical value is $\mathcal{E}^F_c \approx 2.5183$.

We can now compute the single-particle boson and fermion partition functions. At finite temperature, these are defined by

$$z_B(x,\mathcal{E}) = \sum_{m\in\mathbb{Z}}\sum_{k=1}^{\infty} e^{-\beta\omega^B_{m,k}(\mathcal{E})}\,, \qquad z_F(x,\mathcal{E}) = \sum_{m\in\mathbb{Z}+\frac{1}{2}}\sum_{k=1}^{\infty} e^{-\beta\omega^F_{m,k}(\mathcal{E})}\,, \qquad x \equiv e^{-\beta}\,. \tag{5.47}$$

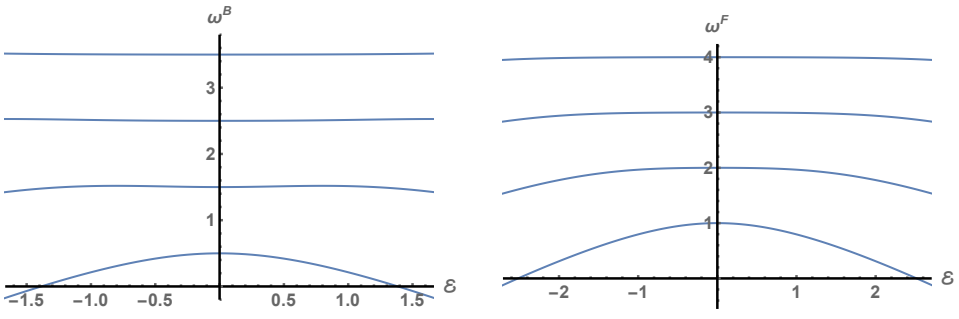

(a) (b)

Figure 5.19: The first four energy levels for (a) the $m = 0$ sector of the free boson, and (b) the $m = 1/2$ sector of the free fermion, as a function of the dipolar potential $\mathcal{E}$.

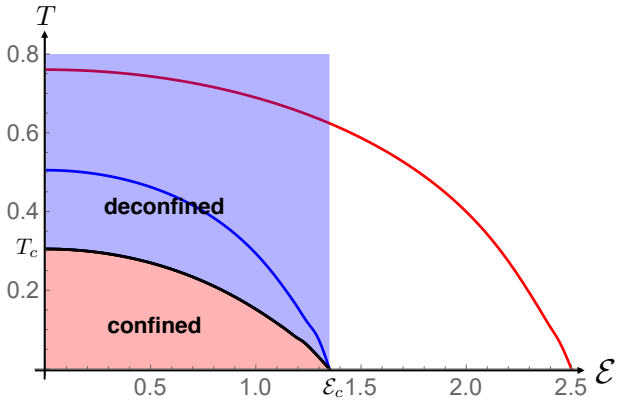

(a)

Figure 5.20: Large N phase diagram for a free adjoint scalar (blue), fermion (red), and combined theory (black). The black curve marks a confinement/deconfinement phase transition. The Hagedorn temperature decreases with $\mathcal{E}$ and goes to zero as $\mathcal{E} \to \mathcal{E}_c$.

Following [33, 34, 35, 43] and using the relevant charges for our case, the Hagedorn temperature is determined by the condition

$$2z_B(x_H, \mathcal{E}) + 2z_F(x_H, \mathcal{E}) + 2z_B(x_H, 0) + 2z_F(x_H, 0) = 1\,, \qquad x_H = e^{-\beta_H}\,, \tag{5.48}$$

where we used the fact that the single particle partition functions are even functions of $\mathcal{E}$.

In 5.20, we plot the Hagedorn temperature as a function of the electric field for a boson (blue), a fermion (red) and the full theory with both a boson and fermion (black). The black curve marks a confinement/deconfinement phase transition. As expected, there is a low temperature confined phase and a high temperature deconfined phase separated by a Hagedorn phase transition that starts at $T_c \approx 0.304836$ at $\mathcal{E} = 0$ and goes to zero as $\mathcal{E} \to \mathcal{E}_c^B$, meaning that the addition of fermions does not change the value of the maximum electric field. For $\mathcal{E} > \mathcal{E}_c^B$ the canonical ensemble does not exist.

5.5 Discussion

We have shown that there exist asymptotically AdS geometries coupled to a neutral scalar that are polarised by a dipolar electric field. There are two soliton and four black hole phases for a range

of electric field values that depend on the temperature.

It is interesting to ask if oppositely charged pairs of probe particles could exist in these polarised backgrounds. Such particles would sit in timelike static orbits at equilibrium positions located at the minima of the potential

$$V = \sqrt{g_{\tau\tau}} - \frac{q}{m} A_\tau \,. \tag{5.49}$$

Note that the extremal limit of a black hole in flat space corresponds to $\lambda = |q/m| = \sqrt{2}$. Therefore, small probe black holes correspond to particles with $\lambda < \sqrt{2}$. In Figure 5.21 we plot the proper radius $\mathcal{P}^*_{\theta=0}$, along the $\theta = 0$ pole, corresponding to stable orbits of charged massive particles in the soliton background, as a function of the electric field. These are shown for λ less than and equal to $\sqrt{2}$. The solid blue curve is the analytic result found by the expansion to third order in $\mathcal{E}$ presented in Appendix A. A contribution to the free energy for such point particles is

$$\delta\mathcal{G} = m V_{min} \,. \tag{5.50}$$

So adding charged particles becomes thermodynamically favorable for $V_{min} < 0$. These exist for certain values of $\mathcal{E}$ and λ as shown in figure 5.22 for the black hole and for the soliton. For the black hole, we plot this for three values of the temperature T. As the black hole temperature is increased, the boundary of these regions move toward smaller values of λ until it crosses the vertical gray line corresponding to $\lambda = \sqrt{2}$, indicating that there exist probe black holes that form stable orbits in these polarized backgrounds. However, we suspect these to be metastable above $\mathcal{E}_c^{Sol}$, drawn as a horizontal gray line. A stable, thermodynamically preferable black hole would lie in the gray region. It is possible that these exist for sufficiently high temperatures, but we do not expect

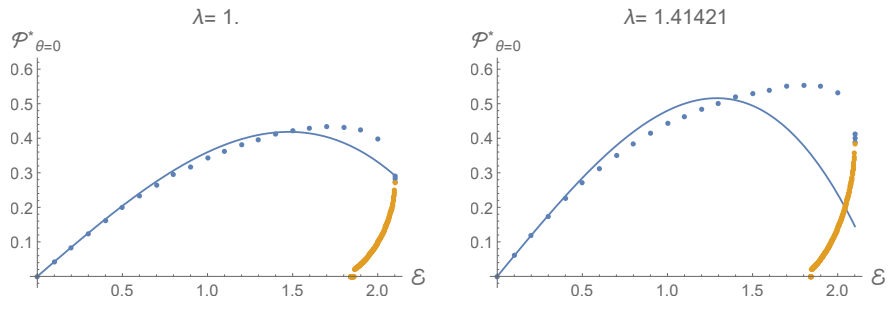

(a) (b)

Figure 5.21: Timelike static orbits of charged particles for two values of $\lambda = q/m$ as a function of the electric field.

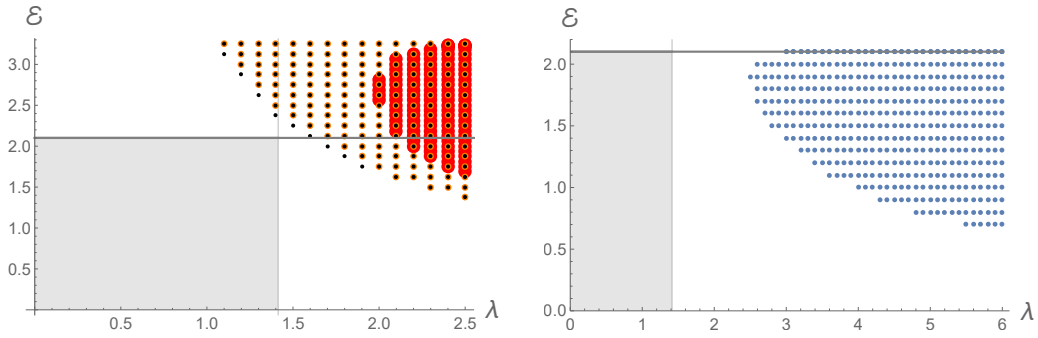

(a) (b)

Figure 5.22: Stable orbits of pointlike charged particles for (a) the black hole for $T = 0.517254$ (red), $T = 1.91981$ (orange), and $T = 9.55129$ (gray) and (b) the soliton. A stable pair of particles that decrease the free energy of the black hole solution would fall in the gray region.

this to be the case. In the polarized soliton backgrounds, no such black hole orbits can exist.

The solutions we have constructed in this chapter contain only one of the neutral scalar fields of ABJM. In general, ABJM contains other fields, including massive charged scalars.[2] Since the work of [44, 45, 46, 47, 48] we know that small and near extremal RN black holes in AdS can become unstable to perturbations governed by charged scalar fields. Motivated by these two facts, we decided to investigate whether charged scalar fields $\widetilde{\phi}$ that are minimally coupled to gravity can become unstable. As such, we considered the following

$$\mathcal{D}^a \mathcal{D}_a \widetilde{\phi} = 0 \,, \tag{5.51}$$

with $\mathcal{D} = \nabla - i\, q\, A$. Since our background admits a Killing vector field $\partial/\partial t$ we can Fourier decompose our perturbations with respect to t

$$\widetilde{\phi}(t, r, \theta) = e^{i\omega t} \phi(r, \theta) \,. \tag{5.52}$$

Modes with $\mathrm{Im}(\omega) < 0$ grow exponentially with time and are unstable, while modes with $\mathrm{Re}(\omega) > 0$ are stable. In this thesis we are not interested in the growth rate of these novel hairy solutions, instead we are interested to know where they connect in the moduli space with the ones we constructed. As such, we can set $\omega = 0$, and search directly for zero-modes. These turn out to obey a

[2] The mass and the charge of these scalars is not arbitrary, instead they are both function of the quantum numbers of the fields with respect to the round $\mathbb{CP}^3$. Furthermore, they can appear from a lower dimensional point of view as a set of complicated coupled equations which only effectively decouple close to the boundary. We will bypass this, and consider a massless charged scalar field as a proxy for the more complicated cases.

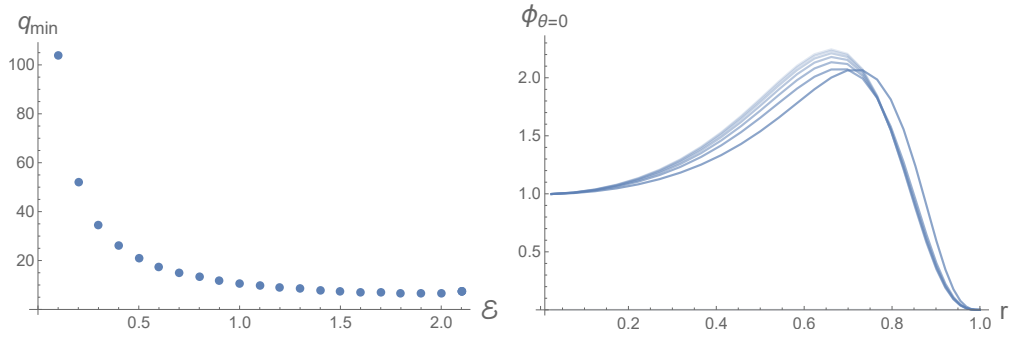

(a) (b)

Figure 5.23: Instability onset for a charged scalar in a polarized soliton background. The plot on the left shows the critical value of q at which the instability occurs as a function of the electric field. The plot on the right shows the scalar field profile at the pole as a function of the coordinate r for a range of electric field values.

rather simple equation of the form

$$\nabla^2\phi = q^2 A_t^2 \phi\,, \tag{5.53}$$

where the metric connection and gauge field A_t are the polarized black hole or soliton geometries constructed above. We solve this generalized eigenvalue problem numerically for ϕ and q.

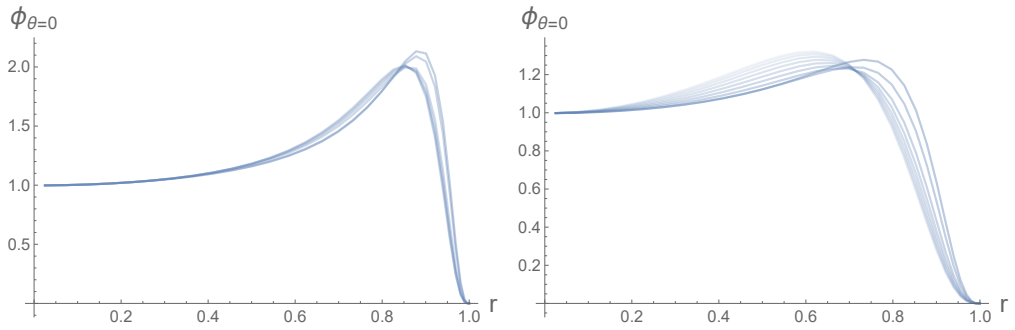

(a) (b)

Figure 5.24: Instability onset for a charged scalar in a polarized black hole background with a temperature $T = 1/\pi$ for a range of electric field values. The curves get taller and fainter as the electric field decreases. The left and right plots show the scalar field profiles at the pole as a function of r for the small and large black holes, respectively.

In figure 5.23, we plot the smallest eigenvalue q corresponding to the minimum value at which an instability occurs in the soliton background as a function of the electric field. We also plot

the associated scalar field profiles at the pole as a function of the radial coordinate for several values of the electric field. Similar scalar field profiles are plotted for the small and large black hole backgrounds in figure 5.24 for a fixed temperature of $1/\pi$. In all backgrounds, the scalar field curves get taller and fainter as the electric field is decreased. We can see from these plots that there exist unstable modes at any value of the electric field. We also find such modes in the black hole background, for all values of temperature and electric field accessible to our solutions. To understand the relevance of these results for ABJM, one would have to determine the mass and charge of the scalar fields in ABJM, and see if they appear as minimally coupled fields from a 4D perspective. If a massless scalar field is found with sufficiently large $q > q_{\min}$, our results suggest that such a configuration will be unstable beyond a certain value of $\mathcal{E}(q_{\min})$.

The zero coupling phase diagram is very similar to the case of SYM with R-charge chemical potentials [49]. This analogy suggests that at weak coupling and high temperature a region of metastability also appears in our system for $\mathcal{E} > \mathcal{E}_c^B$. This would be qualitatively similar to the strong coupling phase diagram shown in figure 5.18. However, since the spectrum depends on the coupling, $\mathcal{E}_c^B$ does not equal $\mathcal{E}_c^{Sol}$.

Chapter 6

Supergravity Dual to the BMN Matrix Model

The gauge/gravity duality is a powerful predictive tool. Given a relatively simple geometry, we can learn about a strongly-coupled field theory without having to treat the problem directly. It is, however, a conjecture, and we should take the rare opportunity to provide evidence of its prowess whenever possible. We now move to an example of the gauge/gravity duality that can be analysed at strong coupling on both sides of the correspondence.

6.1 Introduction

Some quantum mechanical systems admit a parametric limit in which they are well described by a classical gravitational theory. Such systems are examples of quantum theories of gravity. It is not easy to find a system with this property but the gauge/gravity duality offers several cases [50, 51].

Perhaps the most striking example is $(0+1)$-dimensional $SU(N)$ Super Yang-Mills (SYM) theory. This theory contains a finite number of bosonic and fermionic degrees of freedom which are naturally organized in N by N traceless hermitian matrices X^i and Ψ^α, respectively. This model is often termed BFSS [3], with action given by

$$S_{D0} = \frac{N}{2\lambda}\int dt\,\mathrm{Tr}\left[(D_tX^i)^2 + \Psi^\alpha D_t\Psi^\alpha + \frac{1}{2}\left[X^i,X^j\right]^2 + i\Psi^\alpha\gamma^j_{\alpha\beta}[\Psi^\beta,X^j]\right], \tag{6.1}$$

where $D_t = \partial_t - i[A,\ ]$ is the covariant derivative and summation over spatial indices $i,j = 1,\ldots,9$

and spinor indices $\alpha, \beta = 1, \ldots, 16$ is implicit. The X_i are nine scalar matrices in the adjoint representation of the gauge group SU(N) with anti-Hermitian generators T^a. Ψ are Majorana fermions also in the adjoint representation. The N diagonal components of these matrices correspond to the positions of the N D0-branes and the off-diagonal components represent string interactions between them. By dimensional analysis, one concludes that the 't Hooft coupling λ has units of energy cubed. Therefore, the thermodynamics of this system is controlled by two dimensionless parameters: N and $\tau = T/\lambda^{\frac{1}{3}}$, where T is the temperature. According to the gauge/gravity duality, at large N and small dimensionless temperature τ this theory is dual to 11-dimensional supergravity in the following black hole geometry.

$$ds^2 = \frac{dr^2}{f(r)} + r^2 d\Omega_8^2 + \frac{R^7}{r^7} dz^2 + f(r) dt \left(2dz - \frac{r_0^7}{R^7} dt \right), \tag{6.2}$$

where

$$f(r) = 1 - \left(\frac{r_0}{r} \right)^7, \qquad \left(\frac{R}{\ell_s} \right)^7 = 60\pi^3 g_s N, \qquad \left(\frac{r_0}{\ell_s} \right)^5 = \frac{120\pi^2}{49} (2\pi g_s N)^{\frac{5}{3}} \tau^2, \tag{6.3}$$

with ℓ_s the string length and $g_s = 4\pi^2 \ell_s^3 \lambda / N$ the string coupling. This follows from the decoupling limit of N coincident D0-branes in type IIA supergravity [51], which leads to a charged spherically symmetric black hole in ten dimensions. It is sometimes more convenient to work with the solution uplifted to eleven dimensions, where it is purely geometric and describes a black string with horizon topology $S^1 \times S^8$. In our conventions, the 11-dimensional Newton constant is given by $16\pi G_N = (2\pi)^8 g_s^3 \ell_s^9$ and the periodic coordinate z obeys $z \sim z + 2\pi g_s \ell_s$. The type IIA and 11D SUGRA solutions are, however, equivalent descriptions of the same gravitational set-up. The 10-dimensional geometry can be found via Kaluza-Klein compactification of the 11-dimensional metric. In doing so, we couple the 10-dimensional geometry to a 1-form gauge field and a dilaton field. The thermodynamics of a generic Dp-brane from the type IIA perspective was derived in section 2.3.

This D0-brane description leads to the following prediction for the large N and low temperature expansion of the free energy[1]

$$\frac{F}{\lambda^{\frac{1}{3}} N^2} = \left[c_1 \tau^{\frac{14}{5}} + c_2 \tau^{\frac{23}{5}} + \ldots \right] + \frac{1}{N^2} \left[c_3 \tau^{\frac{2}{5}} + c_4 \tau^{\frac{11}{5}} + \ldots \right] + \ldots, \tag{6.4}$$

[1]We are assuming $\tau \gg N^{-\frac{5}{9}}$. For lower temperatures, the black string suffers from the Gregory-Laflamme instability and the stable black hole should have S^9 horizon topology. For even lower temperatures $\tau \sim N^{-\frac{5}{6}}$, the curvature at the horizon of (6.2) reaches the Planck scale.

where the c_i are numerical coefficients. The leading term follows from the classical black hole thermodynamics of (6.2), which gives $c_1 = -\frac{1}{21}\left(\frac{120\pi^2}{49}\right)^{7/5}$. The coefficient c_2 is not known analytically because it follows from unknown α'^3 corrections to type IIA effective action [4]. The $1/N^2$ terms correspond to quantum corrections associated to string loops in the 10 dimensional picture. Notably, the coefficient c_3 has been computed recently using the quartic curvature corrections to 11D supergravity [52]. It is an outstanding challenge to reproduce analitically these predictions directly from the matrix quantum mechanics (6.1). In fact, the state of the art is a scaling hypothesis for the several terms of the moduli effective action that correctly predicts the leading low-temperature dependence $\tau^{\frac{14}{5}}$ but it is unable to fix the coefficient c_1 and any of the subleading terms [53, 54]. The mean field approximation of [55, 56, 57] claimed partial success in reproducing the gravity prediction but their numerical method breaks down for sufficiently low temperature [58].

In a remarkable series of papers [59, 60, 61, 4, 62, 63, 5], the authors performed Monte-Carlo simulations of the matrix quantum mechanics (6.1) at finite temperature. In [4], they studied the planar limit ($N \to \infty$) at low temperature and obtained the first two terms in equation (6.4). Their results agree with all available analytical results from the gravity dual and provide a prediction for c_2. More recently [5], a study of $1/N^2$ effects confirmed the gravitational prediction for the coefficient c_3. This is among the most impressive tests of the gauge/gravity duality we are aware of. Notice that this includes quantum gravity loop effects and probes the regime of chaotic dynamics where supersymmetry is completely broken and integrability is absent. In the next section, we present a massive deformation of the D0-brane matrix quantum mechanics and its corresponding black hole geometry. The deformed theory can also be simulated on a computer using Monte Carlo techniques and will provide a novel test of the gauge/ gravity duality.

We will study the thermodynamics of a massive deformation of the matrix quantum mechanics (6.1). This model goes by the name BMN after the authors of [6]. It has been argued that there exists an equivalence between the Discrete Light Cone Quantization (DLCQ) of M-theory and the large N limit of a configuration of D0-branes described by matrix quantum mechanics. The BMN matrix model corresponds to a particular Discrete Light Cone Quantization (DLCQ) in a maximally supersymmetric plane wave background. For that reason, it is often called the Plane Wave Matrix Model, or PWMM. Its action reads

$$S = S_{D0} - \frac{N}{2\lambda}\int dt\, \mathrm{Tr}\left[\frac{\mu^2}{3^2}(X^i)^2 + \frac{\mu^2}{6^2}(X^a)^2 + \frac{\mu}{4}\Psi^\alpha\left(\gamma^{123}\right)_{\alpha\beta}\Psi^\beta + i\frac{2\mu}{3}\epsilon_{ijk}X^iX^jX^k\right], \qquad (6.5)$$

where the indices i, j, k run over $1, 2, 3$ and the index a runs over $4, \ldots, 9$. The matrix γ^{123} is equal to $\frac{1}{6}\epsilon_{ijk}\gamma^i\gamma^j\gamma^k$, with ϵ_{ijk} the standard 3 dimensional ϵ-tensor. This means that the mass parameter μ breaks the $SO(9)$ global symmetry of (6.1) down to $SO(6) \times SO(3)$. The deformation also retains maximal supersymmetry [6].

The BMN model has three significant advantages over the BFSS model. The first is that it has a discrete energy spectrum and a well defined canonical ensemble. Notice that, strictly speaking, the canonical ensemble of the matrix quantum mechanics (6.1) does not exist. [2] The reason for this is that the eigenvalues of commuting matrices X^i can be made arbitrarily large without energy cost. On the gravity side, this means that the black holes can be unstable since the D0-branes can Hawking radiate away from them. In fact, the Monte-Carlo simulations only work because there is a meta-stable thermal equilibrium with a decay rate that is very small at large N. The mass and Meyers terms in the BMN action discretize the vacua by removing the flat directions of the BFSS matrix model that are at the root of this problem. The D0-brane wavefunctions, instead of being evenly distributed throughout space, are localized in fuzzy spheres. The second advantage is that the BMN model has a dimensionless coupling constant $g \equiv \lambda/\mu^3$ that, together with the dimensionless temperature T/μ, parametrize a two-dimensional phase diagram. This means that we can use the dual gravitational description at large N and strong coupling $g \gg 1$, to predict many observables as functions of the dimensionless temperature T/μ. Finally, the third advantage is that the BMN model is expected to have a phase transition whose critical temperature should be easy to measure in Monte-Carlo simulations. [3]

In figure 4.15 we depict the phase diagram of the theory in the planar limit $N \to \infty$. In the weak coupling regime $g \ll 1$, the dynamics of the system can be studied using perturbation theory. One starts by expanding the fields around one of the minima of the potential

$$\frac{N}{2\lambda}\,\mathrm{Tr}\left[\frac{\mu^2}{6^2}(X^a)^2 - \frac{1}{2}\left[X^a, X^b\right]^2 - \frac{1}{2}\left([X^i, X^j] - i\frac{\mu}{3}\epsilon_{ijk}X^k\right)^2\right]. \tag{6.6}$$

Since this is a sum of squares, the minima are given by $X^a = 0$ and $X^i = \frac{1}{3}\mu\, J^i$, with J^i a N-dimensional representation of $SU(2)$ (in other words $[J^i, J^j] = i\epsilon_{ijk}J^k$). This means that the minima are in one-to-one correspondence with integer partitions of N because we can form an $N \times N$ block diagonal matrix by adding many blocks with $SU(2)$ irreducible representations. In

[2] In [62], it was shown explicitly that the free energy of BFSS has an infrared divergent contribution at order N. The same paper suggested the study of the BMN model as a way to tame this problem.

[3] This is qualitatively similar to the case of 2D SYM compactified on a circle [64].

the large N limit, tunnelling between different vacua is suppressed and it is possible to study the thermodynamics associated to each minimum [65].[4] In this thesis, we will focus on the trivial vacuum $X^a = X^i = 0$. The excitations above this vacuum are gapped and weakly coupled if $g \ll 1$. For energies much greater than μ and much smaller than μN^2 the density of states grows exponentially with energy. This leads to a Hagedorn phase transition at $T = \frac{\mu}{12 \log 3}$ for $g = 0$. At weak coupling g, this becomes a first order phase transition whose critical temperature can be computed in perturbation theory [66, 67]

$$T_c(g) = \frac{\mu}{12 \log 3} \left[1 + \frac{2^6 \cdot 5}{3} g - \left(\frac{23 \cdot 19927}{2^2 \cdot 3} + \frac{1765769}{2^4 \cdot 3^2} \log 3 \right) g^2 + \mathcal{O}(g^3) \right] . \tag{6.7}$$

We call the high temperature phase the deconfined phase because the free energy scales as N^2. For $T < T_c$ the system is in the confined phase where the free energy scales as N^0.

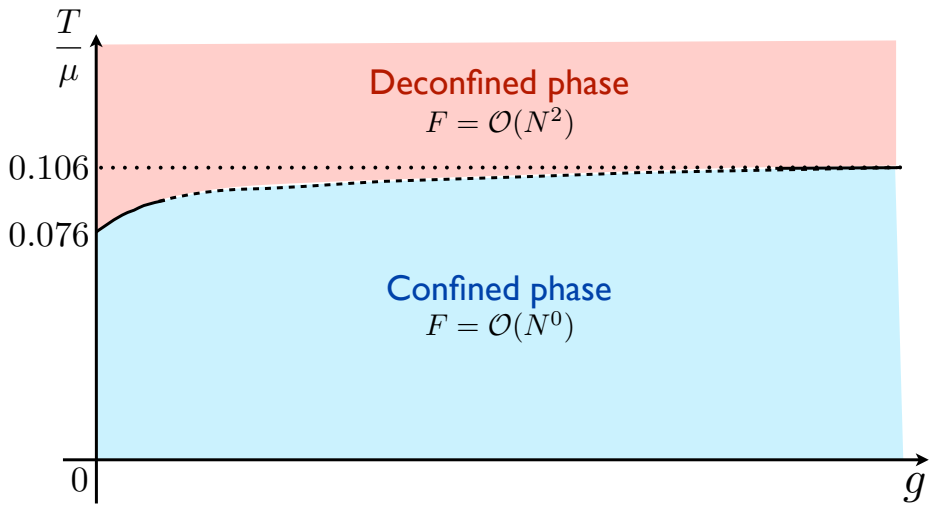

Figure 6.1: The phase diagram of the PWMM. At high temperature, the system is in a deconfined phase where the free energy scales like N^2. As we lower the temperature, the system undergoes a first order phase transition to a confined phase where the free energy scales as N^0. The critical temperature T_c depends on the dimensionless coupling g and it can be computed in perturbation theory for $g \ll 1$. In this thesis we determine T_c at strong coupling from the study of the black hole dual to the deconfined phase of the PWMM.

The main goal of the present work is to determine the fate of this phase transition at strong

[4] More precisely, this works for vacua that are associated with a reducible representation of $SU(2)$ that contains many copies (of order N) of a few irreducible representations of fixed dimension. If the dimensions of the irreducible representations scale with N and there are a fixed number of them (membrane states) then the free energy is of order 1 and there is no phase transition. In fact, the fluctuations around these vacua become free in the 't Hooft limit [66].

coupling $g \gg 1$. It is instructive to compare figure 4.15 with the phase diagram of $\mathcal{N} = 4$ SYM on S^3. In this comparison $1/\mu$ plays the role of the radius of S^3 and g plays the role of the 4-dimensional 't Hooft coupling.[5] The 4-dimensional theory also has a first order phase transition that starts with a Hagedorn transition of the free theory [69]. At strong coupling, this transition corresponds to the Hawking-Page transition in the dual AdS_5 gravitational description [70, 71]. We will argue that the PWMM has a very similar phase diagram. In particular, we will find a Hawking-Page like phase transition in the dual gravitational description of the PWMM and predict the strong coupling limit of the critical temperature,

$$\lim_{g\to\infty} \frac{T_c(g)}{\mu} = 0.105905(57)\,. \tag{6.8}$$

It would be remarkable to confirm this prediction with Monte-Carlo simulations of the PWMM at strong coupling, accessible with the methods of [59, 60, 61, 4, 5]. A current simulation is underway and we hope will give promising evidence of our strong-coupling result.

The dual geometries to each vacuum of the PWMM were constructed in [8, 9]. These SUSY vacuum geometries, including the one dual to the trivial vacuum, are surprisingly complicated [72]. Nevertheless, they share an important feature in that they asymptote to the plane wave solution of M-theory

$$ds^2 = dx^i dx^i + dx^a dx^a + 2dtdz - \left(\frac{\mu^2}{3^2}x^i x^i + \frac{\mu^2}{6^2}x^a x^a\right) dt^2\,, \qquad dC = \mu\, dt \wedge dx^1 \wedge dx^2 \wedge dx^3\,. \tag{6.9}$$

Fortunately, we will not need the detailed form of these vacuum geometries. Our strategy will be to start from very high temperature ($T \gg \mu$) and gradually decrease it. This means that our starting solution is the uplifted 11D SUGRA solution (6.2) for which the 4-form field strength vanishes. This geometry has the same $SO(9)$ symmetry of the trivial vacuum $X^a = X^i = 0$. We will then continuously deform this solution by turning on a non-normalizable mode of dC that corresponds to the relevant deformation that takes the BFSS to the BMN model. This deformation breaks the $SO(9)$ symmetry of (6.2) to $SO(6) \times SO(3)$, making the field equations analytically intractable. In the next section, we explain how this is done in detail, including the numerical methods to solve the relevant Einstein equations. In section 6.4, we determine the free energy of the black hole constructed in section 6.3 and the strong coupling limit of the critical temperature $T_c(g)$. We also calculate thermal expectation values of several operators in the high temperature deconfined phase. We conclude in section 6.5 with a discussion and comments about open questions.

[5] In fact, the action (6.5) can be obtained from the action of SYM on S^3 by truncating the 4-dimensional fields to their zero modes (more precisely, projecting to $SU(2)_L$ invariant modes) [68].

6.2 Vacuum geometries

The supergravity solutions dual to each of the BMN vacua were constructed in [8, 9]. They are given by

$$\begin{aligned} ds^2 &= \left(\frac{\dot{V}\Delta}{2V''}\right)^{\frac{1}{3}} \left[-\frac{4\ddot{V}}{\ddot{V}-2\dot{V}}dt^2 + \frac{-2V''}{\dot{V}}(d\rho^2+dz^2) + 4d\Omega_5^2 + 2\frac{V''\dot{V}}{\Delta}d\Omega_2^2\right] \\ &\quad + \left(\frac{4}{-V''\dot{V}^2\Delta^2}\right)^{\frac{1}{3}} \left(dx_{11} - \frac{2\dot{V}'\dot{V}}{\ddot{V}-2\dot{V}}dt\right)^2 \\ A_3 &= -4\frac{\dot{V}^2V''}{\Delta}dt\wedge d^2\Omega_2 + 2\left(\frac{\dot{V}\dot{V}'}{\Delta}+z\right)dx_{11}\wedge d^2\Omega_2 \ , \end{aligned} \tag{6.10}$$

where $\Delta = (\ddot{V}-2\dot{V})V'' - (\dot{V}')^2$, the dot indicates derivative with respect to $\log\rho$ and the prime indicates derivative with respect to z. Because of the broken $SO(9)$ symmetry, it is useful to consider the radial coordinate r as well as the radius of the 5-sphere ρ and the radius on the 2-sphere z. It was shown in [9] that the equations of motion in this ansatz reduces to a 3-dimensional Laplace's equation in cylindrical coordinates

$$\frac{1}{\rho}\partial_\rho(\rho\partial_\rho V) + \partial_z^2 V = 0 \ . \tag{6.11}$$

In [8], they showed that the fuzzy-sphere vacua correspond to a collection of D0-branes localized around the origin of a 6-dimensional subspace or a 3-dimensional subspace due to the massive deformations in these directions. To see this, they started from the near horizon geometry dual to the BFSS matrix model. They then found that the D0-branes polarize into D2 or NS5 branes by turning on the 3 or 6-form fluxes that couple to them. It was then found in [9] that these vacua could be described by a certain configuration of axially-symmetric charged conducting discs and a fixed background potential. The boundary conditions and potential source specifies the configuration and therefore singles out a specific classical vacuum and potential $V(\rho,z)$ which gives the corresponding supergravity solution. At the boundary, each configuration has an infinite conducting disk at $z=0$ on which the potential vanishes, giving the condition $V(z=0)=0$. In addition, V is constrained by its asymptotic behavior $V \approx \rho^2 z - \frac{2}{3}z^3$.

Based on this ansatz, we see that the S^5 shrinks to nothing on the $\rho=0$ axis of symmetry. Non-contractible 6-spheres then occur when the sphere wraps around a charged plate in the z-direction that has N_2 units of charge, therefore asking us to consider a configuration of N_2 D2-branes. Similarly, the S^2 shrinks away on any of the conducting plates. Non-vanishing 3-spheres are then

those that begin and end on different plates separated by a distance proportional to the NS charge N_5, suggesting a configuration of N_5 NS5-branes. The total charge is then given by

$$N = \sum N_{2,i} N_{5,i} \tag{6.12}$$

where i is a sum over the paths that give non-contractible S^3's and S^6's. In the field-theory language, N_5 tells us to which irreducible representation of SU(2) our configuration corresponds and N_2 tells us how many times that representation is repeated. Later on in the thesis, we will see that there is some ambiguity in turning on the fluxes that deform the hot D0-brane geometry. We will use the intuition gained in this section to argue the correct boundary condition for the gauge fields that correspond to the supergravity solution we want to find.

6.3 Deformed Black Hole

Let us start by fixing our conventions for the bosonic piece of the 11-dimensional SUGRA action

$$I = \frac{1}{16\pi G_N} \int \left(\widetilde{\eta}\mathcal{R} + \frac{1}{2} dC \wedge \star dC - \frac{1}{6} C \wedge dC \wedge dC \right), \tag{6.13}$$

where $\widetilde{\eta}$ is the space-time volume form, $\mathcal{R}$ is the Ricci scalar and C is a 3-form gauge potential. The corresponding equations of motion are

$$\begin{aligned} d\left(\star dC\right) + \tfrac{1}{2} dC \wedge dC &= 0 \\ R_{\mu\nu} = \tfrac{1}{12} \left((dC)_{\mu\alpha\beta\gamma} (dC)_{\nu}^{\alpha\beta\gamma} - g_{\mu\nu} (dC)^2 \right). & \end{aligned} \tag{6.14}$$

Any stationary solution compatible with the $SO(6) \times SO(3)$ global symmetry and invariant under translations along the eleventh direction can be written as

$$\begin{aligned} ds^2 =& - A \, \frac{(1-y^7)}{y^7} d\eta^2 + T_4 \, y^7 \left[d\zeta + \Omega \, \frac{(1-y^7) d\eta}{y^7} \right]^2 \\ &+ \frac{1}{y^2} \left[B \, \frac{(dy + F dx)^2}{(1-y^7) y^2} + T_1 \, \frac{4 dx^2}{2 - x^2} + T_2 \, x^2 (2 - x^2) d\Omega_2^2 + T_3 \, (1 - x^2)^2 d\Omega_5^2 \right], \\ C =& \left(M \, d\eta + L \, d\zeta \right) \wedge d\Omega_2 \, , \end{aligned} \tag{6.15}$$

where $\zeta \sim \zeta + 2\pi$ is the periodicity of the 11-dimensional circle and the functions A, B, F, Ω, T_1, T_2, T_3, T_4, M, L depend on the radial coordinate $0 \leq y < 1$ and on the angular coordinate $0 \leq x \leq 1$. We shall see that $y = 1$ corresponds to the black hole horizon and $y = 0$ to the asymptotic region,

which matches the plane wave geometry (6.9). The angular coordinate x was introduced to break the $SO(9)$ symmetry of an eight sphere to $SO(6) \times SO(3)$. We can think of $x = 0$ as the S^5 *equator* and $x = 1$ as the S^2 *pole*, of the 8-dimensional surface $d\eta = d\zeta = dy = 0$. This form of the solution is tailored to the numerical methods we will use. In particular, all quantities are dimensionless and the domain of the unknown functions is the unit square. The physical solution can then be obtained by using the scalings of the 11D SUGRA action under the following transformations

$$\begin{aligned} & g_{ab} \to \lambda^2 g_{ab}\,, \quad C_{abc} \to \lambda^3 C_{abc} \qquad \Rightarrow \quad I \to \lambda^9 I\,, \\ & \zeta \sim \zeta + 2\pi \;\to\; \zeta \sim \zeta + 2\pi\lambda' \qquad \Rightarrow \quad I \to \lambda' I\,, \end{aligned} \tag{6.16}$$

More concretely, the physical solution will be obtained from (6.15) by multiplying the metric by r_0^2 and the 3-form C by r_0^3, and by changing the period of the non-contractible M-theory circle according to

$$\zeta \sim \zeta + 2\pi \left(\frac{R}{r_0}\right)^{\frac{7}{2}} \frac{g_s \ell_s}{r_0}\,. \tag{6.17}$$

Both operations are symmetries of the equations of motion, but change the value of the on-shell action to

$$I = \frac{r_0^9}{16\pi G_N} \left(\frac{R}{r_0}\right)^{\frac{7}{2}} \frac{g_s \ell_s}{r_0}\, \widehat{I} = \frac{15}{28} \left(\frac{15}{14^2\pi^8}\right)^{\frac{2}{5}} N^2 \tau^{\frac{9}{5}}\, \widehat{I}\,, \tag{6.18}$$

where we defined the dimensionless action $\widehat{I}$ to be the 11D SUGRA action (6.13) evaluated on the Ansatz (6.15) and stripped of the overall factor of $1/(16\pi G_N)$.

In the last equality of (6.18), we used the relations (6.3) between the gravitational parameters and the variables of the dual matrix quantum mechanics. When computing the action of a solution, care must be taken by adding boundary terms that renormalise the on-shell action. In what follows we shall assume that such counter-terms preserve both of the scaling operations described above. Similarly, the *physical* Bekenstein-Hawking entropy becomes

$$S = \frac{r_0^9}{4G_N} \left(\frac{R}{r_0}\right)^{\frac{7}{2}} \frac{g_s \ell_s}{r_0}\, \widehat{S} = \frac{15\pi}{7} \left(\frac{15}{14^2\pi^8}\right)^{\frac{2}{5}} N^2 \tau^{\frac{9}{5}} \widehat{S}\,, \tag{6.19}$$

where $\widehat{S}$ is the dimensionless horizon area computed with the metric (6.15), explicitly given by

$$\widehat{S} = \int_{\mathcal{H}} d^9x \sqrt{h} = 16\pi^5 \int_0^1 dx\, x^2 (1-x^2)^5 \left[(2-x^2) T_1(1,x) T_2^2(1,x) T_3^5(1,x) T_4(1,x)\right]^{\frac{1}{2}}\,, \tag{6.20}$$

where h is the determinant of the induced metric on the horizon, which has $S^8 \times S^1$ topology.

To see how this works in practice for a simple case, consider the exact solution given by $A = B = \Omega = T_1 = T_2 = T_3 = T_4 = 1$ and $F = M = L = 0$. Changing coordinates,

$$y = \frac{r_0}{r}\,, \qquad \eta = \left(\frac{r_0}{R}\right)^{\frac{7}{2}} \frac{t}{r_0}\,, \qquad \zeta = \left(\frac{R}{r_0}\right)^{\frac{7}{2}} \frac{z}{r_0}\,, \tag{6.21}$$

and multiplying the metric (6.15) by r_0^2 one recovers the 11-dimensional uplift of the non-extremal D0-brane solution (6.2). Notice that after the Wick rotation $\eta \to i\eta$, the Euclidean time circle of (6.15) must have period $4\pi/7$ in order to avoid a conical singularity. Using (6.21) this fixes the periodicity of the dimensionfull Euclidean time, which is consistent with the relations (6.3) between the temperature and the parameter r_0. Moreover, using the dimensionless area of the horizon $\widehat{S} = 2\pi\,\mathrm{Vol}(S^8)$, we obtain[6]

$$S = \frac{2}{15}\left(\frac{120\pi^2}{49}\right)^{\frac{7}{5}} N^2 \tau^{\frac{9}{5}}\,. \tag{6.22}$$

This exact solution describes the high temperature limit $T/\mu \to \infty$ of the PWMM. To lower the temperature, we need to appropriately turn on the 3-form potential C. This is implemented in the Ansatz (6.15) by requiring the function $M = M(x, y)$ to have the following asymptotic behaviour

$$M \approx \widehat{\mu}\,\frac{x^3(2-x^2)^{\frac{3}{2}}}{y^3}\,, \qquad y \to 0\,. \tag{6.23}$$

To find out the physical meaning of the parameter $\widehat{\mu}$, we compute the asymptotic behaviour of the physical field strength dC, determined after multiplying by r_0^3 and changing coordinates as in (6.21),

$$dC \approx \frac{12\pi}{7}\,\widehat{\mu}\,T\,dt \wedge d(rx\sqrt{2-x^2}) \wedge r^2x^2(2-x^2)d\Omega_2\,. \tag{6.24}$$

Identifying $rx\sqrt{2-x^2}$ as the radial coordinate on the 3-plane that contains the 2-sphere, and comparing with the M-theory plane wave solution (6.9), we conclude that

$$\widehat{\mu} = \frac{7}{12\pi}\frac{\mu}{T}\,. \tag{6.25}$$

In section 6.3.2 below, we will explain the precise boundary conditions that uniquely fix the solution. However, the intuition is clear: we require regularity at the axes of symmetry $x = 0$, $x = 1$ and $y = 1$. In particular, the Euclidean period of the η coordinate is always $4\pi/7$ because we impose $A = B$ at the horizon $y = 1$.[7] At infinity ($y \to 0$), we impose that $A, B, \Omega, T_1, T_2, T_3, T_4 \to 1$, that

[6] Notice that this is compatible with the first term of (6.4) and the first law of thermodynamics $\frac{\partial F}{\partial T} = -S$.

[7] Recall that in Euclidean signature the horizon is the fixed point of time translation symmetry.

$F, L \to 0$, and (6.23). In this way, we obtain a one parameter family of (dimensionless) solutions parametrized by $\widehat{\mu}$. The physical entropy of the system, for example, is then computed using (6.19). Notice that this agrees precisely with the free energy scaling predicted in [53] from the assumption that the tree level and 1-loop contributions for the moduli effective action are of the same order in the strongly coupled regime. It is also clear that thermal expectation values that are non-zero at $\mu = 0$ (*i.e.* in the non-extremal D0-brane) get multiplied by a function of $\widehat{\mu}$, again in agreement with [53].

6.3.1 Harmonic Einstein equations

In both the line element and gauge field ansätze (6.15), we have partially gauge fixed coordinate invariance and completely gauge fixed the gauge redundancy associated with $C \to C + \mathrm{d}\Lambda$, where Λ is a two-form[8]. However, the line element (6.15) still exhibits *full* diffeomorphism invariance for arbitrary reparametrizations of x and y, which we will fix using the DeTurck method.

The 11-dimensional Einstein's equations in the trace reversed form are

$$\widetilde{E}_{ab} \equiv R_{ab} - \frac{1}{12}\left(G_{acde}G_b{}^{cde} - \frac{g_{ab}}{12}G^{cdef}G_{cdef}\right) = 0\,, \tag{6.26}$$

where $G = dC$ is the field strength.

The reference metric we have chosen for the deTurck method is just given by the line element (6.15) with $A = B = T_1 = T_2 = T_3 = T_4 = \Omega = 1$ and $F = 0$. One can show that the resulting system of equations obtained via $E_{ab} \equiv \widetilde{E}_{ab} - \nabla_{(a}\xi_{b)} = 0$ and $d\star dC = 0$ is of the form $\gamma^{ab}\partial_a\partial_b Q_i + F_i(\partial_a Q_k, Q_k) = 0$, where F_i is a complicated function of $\{Q_i\} = \{A, B, F, T_1, T_2, T_3, T_4, \Omega, M, L\}$ and their first derivatives along x and y, and γ^{ab} is a two-dimensional positive symmetric matrix (γ^{ab} is the inverse of the metric tensor (6.15) restricted to a x, y plane with all the other coordinates fixed). This means that, under the appropriate boundary conditions, which we shall discuss below, $E_{ab} = 0$ forms a system of Elliptic partial differential equations consistent with $\xi = 0$.

[8] From the perspective of the gravitational system, the functions M and L behave as scalar fields under arbitrary reparametrizations of x and y, meaning that no gauge fixing procedure is necessary for these matter fields.

6.3.2 Boundary conditions

Our solution naturally lives on a square grid, with $x = 0$ denoting the fixed points of the $SO(3)$ symmetry, $x = 1$ the fixed points of the $SO(6)$, $y = 1$ denoting the horizon location and $y = 0$ the conformal boundary. In an abuse of language, we shall refer to $x = 0$ as the S^5 *equator*, and $x = 1$ as the S^2 *pole*, of the 8-dimensional surface $d\eta = d\zeta = dy = 0$.

We will be interested in measuring certain quantities near the conformal boundary located at $y = 0$. The leading order term in the metric near the boundary is just that of the D0-brane, since the matrix model massive deformation is irrelevant in the UV. Thus we will have

$$\begin{aligned} &A(x,y) = B(x,y) = \Omega(x,y) = T_1(x,y) = T_2(x,y) = T_3(x,y) = T_4(x,y) = 1 + O(y)\,, \\ &F(x,y) = O(y)\,. \end{aligned} \tag{6.27}$$

This guarantees that, asymptotically, the 8-dimensional surface $d\eta = d\zeta = dy = 0$ becomes a round S^8 and that the total D0-brane charge is fixed. The leading term for the functions M and L is fixed by requiring that the non-normalizable mode dual to the massive deformation of the matrix model is turned on. At leading order in y it suffices to consider linear perturbations of the 3-form potential C, which then fix the leading behaviour in y of the functions M and L. These perturbations are naturally expanded in a basis of harmonics of the asymptotic S^8. For the particular Ansatz (6.15) for the 3-form potential,

$$C = (M\, d\eta + L\, d\zeta) \wedge d\Omega_2\,, \tag{6.28}$$

the decomposition in S^8 harmonics only includes the harmonic 2-forms

$$\omega_l = \mathbb{H}_l(x) d\Omega_2\,, \tag{6.29}$$

with l odd and

$$\mathbb{H}_l(x) = x^3\big(2-x^2\big)^{3/2}\ {}_2F_1\left(\frac{1}{2}-\frac{l}{2}, 4+\frac{l}{2}, \frac{5}{2}, x^2\left(2-x^2\right)\right), \tag{6.30}$$

where ${}_2F_1$ is a hypergeometric function. These harmonic 2-forms ω_l satisfy

$$\star_8\, d(\star_8 d\omega) = -\lambda_l \omega\,, \qquad \lambda_l = (l+2)(l+5)\,, \tag{6.31}$$

where $\star_8$ is the Hodge dual on S^8. Note that for odd l, ω_l is invariant under the action of the $SO(6) \times SO(3)$ subgroup of the $SO(9)$ isometry of the S^8. Finally, analysing the perturbations of the 3-form potential C, one concludes that the required non-normalizable mode has non-vanishing

functions M and L, and can be written in terms of the harmonic form ω_l with $l = 1$. Asymptotically, this fixes their leading behaviour to be given by

$$M(x,y) = \widehat{\mu} y^{-3} \mathbb{H}_1(x) + O(y^{-2}) \,, \qquad L(x,y) = \frac{3}{2} \widehat{\mu} y^4 \mathbb{H}_1(x) + O(y^5) \,. \tag{6.32}$$

To better understand the boundary conditions at the conformal boundary we actually need to consider in more detail the asymptotic expansion of the fields. We now turn to this problem.

Asymptotic expansion at conformal boundary

In general, each function will have an asymptotic expansion in powers of y. For example,

$$A(x,y) = \sum_n A_n(x) y^n \,. \tag{6.33}$$

The equations of motion yield second order coupled differential equations in the variable x for all the coefficient functions like $A_n(x)$. These can be easily solved assuming that only smooth solutions on the S^8 of the boundary are allowed, that is to say, all the coefficient functions admit an expansion in harmonics on the S^8 of the boundary. These harmonics can be of scalar, vector or tensor type and must be invariant under the unbroken $SO(3) \times SO(6)$ symmetry.

Let us first consider the functions M and L that are associated to the 2-forms on S^8 introduced above. The expansion in powers of y can be seen to arise from the normalizable and non-normalizable modes that are excited, plus their back-reaction. At the linear level there are two independent field perturbations associated to M and L, which are called v_1 and v_2 in the perturbation analysis of [73]. We can drop the perturbation v_2 because we impose that its non-normalizable modes vanish, and its normalizable modes start at a power of y beyond what we consider in this thesis. Thus, we have

$$\begin{aligned} y^3 M(x,y) &= \sum_{\substack{l \geq 1 \\ odd}} \left(\alpha_l f_l^{(M)}(y) + \widetilde{\alpha}_l \widetilde{f}_l^{(M)}(y) \right) \mathbb{H}_l(x) \; + \; \text{back-reaction} \,, \\ y^{-4} L(x,y) &= \sum_{\substack{l \geq 1 \\ odd}} \left(\alpha_l f_l^{(L)}(y) + \widetilde{\alpha}_l \widetilde{f}_l^{(L)}(y) \right) \mathbb{H}_l(x) \; + \; \text{back-reaction} \,, \end{aligned} \tag{6.34}$$

where we denote non-normalizable modes with a tilde and normalizable without. These non-normalizable modes behave near the boundary as $\widetilde{f}_l^{(M)}(y) \sim \widetilde{f}_l^{(L)}(y) \sim y^{1-l}$. We set them all to zero but the mode $l = 1$. This is the content of the boundary condition (6.32), which sets

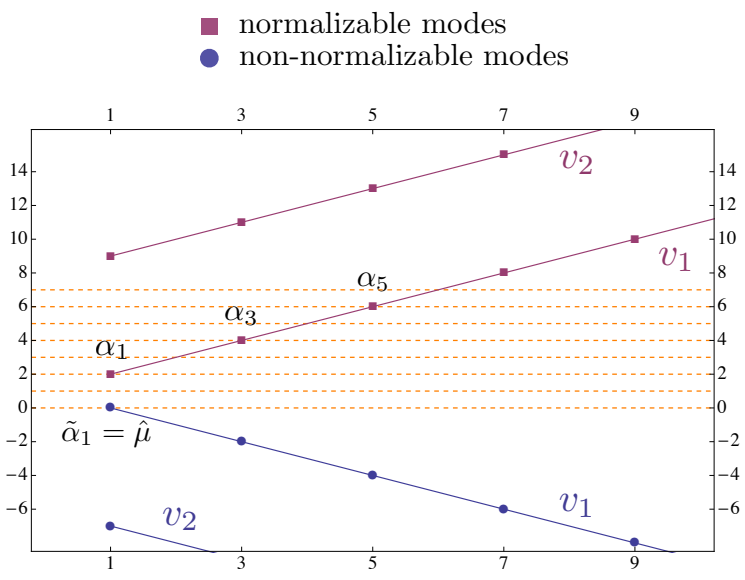

Figure 6.2: The modes of the 2-form perturbation v_1 have a leading behaviour near the boundary of the form y^{1-l} for non-normalizable modes and y^{1+l} for normalizable. The figure shows the power of y as a function of spin l. It also includes the powers for the other perturbation v_2. The dashed lines cover the region considered in this manuscript, up to order y^7.

$\widetilde{\alpha}_1 = \widehat{\mu}$, and defines the type of relevant deformation we decided to turn on. Of course we are not free to set the normalizable modes to zero. Their form can only be obtained once the solution is known everywhere, *i.e.* once regularity deep in the bulk and at the axis is imposed. These modes behave as $f_l^{(M)}(y) \sim f_l^{(L)}(y) \sim y^{1+l}$, near the boundary. Notice that the normalizable modes of the perturbations v_2, which we dropped in (6.34), have $f_l(y) \sim y^{8+l}$. Figure 6.2 summarizes these facts. In (6.34), we called back-reaction to all terms that are non-linear in the modes. At each order in the expansion at $y = 0$, these can also be expanded in harmonic 2-forms on S^8. In this thesis, we consider the first 8 terms in the expansion,

$$
\begin{aligned}
y^3 M(x,y) = {} & \widehat{\mu}\left(1 - \frac{9}{7}y^7\right)\mathbb{H}_1(x) \\
& - \frac{3}{176}\widehat{\mu}^3 y^5\big(43\mathbb{H}_1(x) - 65\mathbb{H}_3(x)\big) - \frac{3}{616}\alpha_1\widehat{\mu}^2 y^7\big(97\mathbb{H}_1(x) - 350\mathbb{H}_3(x)\big) - \frac{3}{4}\widehat{\mu}(\delta+2\gamma)y^7\mathbb{H}_1(x) \\
& - \frac{3}{50336}\beta_2\widehat{\mu}^3 y^7\big(4811\mathbb{H}_1(x) - 33488\mathbb{H}_3(x) + 71148\mathbb{H}_5(x)\big) + O(y^8)\,.
\end{aligned}
\tag{6.35}
$$

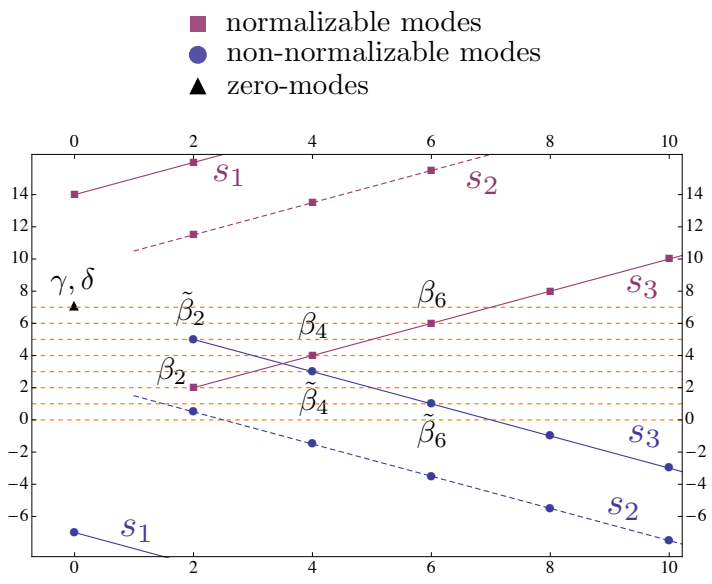

Figure 6.3: Leading power of y near the boundary of non-normalizable and normalizable modes of the scalar perturbation s_3. Behaviour of the zero-modes is also included, as well as that of the scalar perturbations s_1 and s_2. The latter is dashed because it vanishes in the static case here considered. Dashed horizontal lines cover the region considered in this thesis.

$$
\begin{aligned}
y^{-4}L(x,y) = {} & \widehat{\mu}\left(\frac{3}{2}+\frac{6}{35}\,y^7\right)\mathbb{H}_1(x)+\alpha_1 y^2\mathbb{H}_1(x)+\alpha_3 y^4\mathbb{H}_3(x)+\alpha_5 y^6\mathbb{H}_5(x) \\
& -\frac{315}{44}\beta_2\widehat{\mu}y^2\mathbb{H}_3(x)+\frac{1617}{80}\beta_4\widehat{\mu}y^4\mathbb{H}_5(x)+\frac{\widehat{\mu}^3y^5}{880}\big(1575\mathbb{H}_3(x)-464\mathbb{H}_1(x)\big)-\frac{27027}{608}\beta_6\widehat{\mu}y^6\mathbb{H}_7(x) \\
& -\frac{3\widehat{\mu}y^7}{80080}\big(26598\alpha_1\widehat{\mu}+47327\beta_2\widehat{\mu}^2+52624\gamma-4576\delta\big)\mathbb{H}_1(x)+\frac{7\widehat{\mu}^2y^7}{1056}\big(528\alpha_1+1165\beta_2\widehat{\mu}\big)\mathbb{H}_3(x) \\
& -\frac{39053}{2496}\beta_2\widehat{\mu}^3y^7\mathbb{H}_5(x)+O(y^8)\,.
\end{aligned}
\tag{6.36}
$$

where the coefficients β_i, δ and γ appear in the expansion of scalar perturbations that we discuss in a moment. Note that the first line in the expansions (6.35) and (6.36) contains the terms linear in the modes, while the remaining terms arise from the back reaction of the fields.

The modes of the 2-form perturbation v_1 have a leading behaviour near the boundary of the form y^{1-l} for non-normalizable modes and y^{1+l} for normalizable modes. Figure 6.2 shows the power of y as a function of the spin l. It also includes the powers for the other perturbation v_2. The dashed horizontal lines cover the region considered in this manuscript, up to order y^7.

There are five S^8 scalars in our Ansatz. They are the functions A, B, T_4, Ω and the trace of

the S^8 metric fluctuations that we define by

$$Q = \frac{T_2 + 2T_3 + 5T_4}{8}\,. \tag{6.37}$$

As in the previous case these fields can be expressed in terms of non-normalizable and normalizable modes, as well as the back reaction of all modes. In general, at the linear level there are three independent scalar perturbations, called s_1, s_2 and s_3 in [73]. The perturbation s_2 vanishes for our Ansatz (this follows because our geometry is static after reducing to type IIA supergravity). We also drop the perturbation s_1 because our boundary condition impose the vanishing of its non-normalizable modes and its normalizable modes only start at order y^{14} in the expansion near the boundary. Thus, for the purposes of this thesis, we have

$$A(x,y) = \sum_{\substack{l\geq 2\\ even}} \left(\beta_l f_l^{(A)}(y) + \widetilde{\beta}_l \widetilde{f}_l^{(A)}(y)\right)\mathbb{S}_l(x) \,+\, \text{zero-modes} \,+\, \text{back-reaction}\,, \tag{6.38}$$

and similarly for B, T_4, Ω and Q. The functions $\mathbb{S}_l$ are S^8 scalar harmonics, that are $SO(3)\times SO(6)$ invariant, and have the form

$$\mathbb{S}_l(x) = \frac{\mathrm{P}^2_{3+l}\left(x\sqrt{2-x^2}\right)}{15x\sqrt{2-x^2}(1-x^2)^2}\,, \tag{6.39}$$

with l even and P^m_n the associated Legendre polynomial of degree n and azimuthal number m. These functions are the usual eigenfunctions of the Laplace operator on S^8 with

$$\star_8\, d(\star_8 d\mathbb{S}_l) = -\lambda_l \mathbb{S}_l\,, \qquad \lambda_l = l(l+7)\,. \tag{6.40}$$

We also impose that the non-normalizable modes of the perturbation s_3 vanish. As shown in figure 6.3 this includes the three modes $\widetilde{\beta}_2$, $\widetilde{\beta}_4$, and $\widetilde{\beta}_6$ that appear in the expansion near the boundary at order y^5, y^3, and y, respectively. The leading behaviour of the normalisable modes is also shown in the figure. The scalar perturbations also contain two zero-modes that we denote by γ and δ. These modes appear first at order y^7 and are constant on the S^8. We call them zero-modes because they are not the zero frequency limit of any time dependent perturbation. Up to order y^7 the scalar perturbations have the form

$$\begin{aligned}
A(x,y) = {} & 1 - \beta_2 y^2 \mathbb{S}_2(x) - \beta_4 y^4 \mathbb{S}_4(x) - \beta_6 y^6 \mathbb{S}_6(x) - y^7\left(\delta + \frac{5}{2}\gamma\right)\mathbb{S}_0(x) \\
& + \frac{7}{143}\beta_2^2 y^4\big(91\mathbb{S}_0(x) + 22\mathbb{S}_2(x) + 30\mathbb{S}_4(x)\big) + \frac{1}{560}\widehat{\mu}^2 y^5\big(50\mathbb{S}_2(x) - 21\mathbb{S}_0(x)\big) \\
& + \frac{14}{1105}\beta_2\beta_4 y^6\big(612\mathbb{S}_2(x) + 220\mathbb{S}_4(x) + 273\mathbb{S}_6(x)\big) + \frac{1}{840}\alpha_1\widehat{\mu} y^7\big(495\mathbb{S}_0(x) + 104\mathbb{S}_2(x)\big) \\
& + \frac{1}{205920}\beta_2\widehat{\mu}^2 y^7\big(-232245\mathbb{S}_0(x) + 51582\mathbb{S}_2(x) + 13600\mathbb{S}_4(x)\big) \\
& - \frac{49}{2431}\beta_2^3 y^6\big(238\mathbb{S}_0(x) + 561\mathbb{S}_2(x) + 180\mathbb{S}_4(x) + 126\mathbb{S}_6(x)\big) + O(y^8)\,,
\end{aligned} \tag{6.41}$$

$$B(x,y) = 1 + \delta y^7 \mathbb{S}_0(x) \tag{6.42}$$
$$+ \frac{1}{2}\widehat{\mu}^2 y^5 \mathbb{S}_0(x) - \frac{16}{147}\alpha_1 \widehat{\mu} y^7 \mathbb{S}_2(x) - \frac{5}{3003}\beta_2 \widehat{\mu}^2 y^7 \big(82\mathbb{S}_2(x) + 35\mathbb{S}_4(x)\big) + O(y^8)\,,$$
$$T_4(x,y) = 1 + \beta_2 y^2 \mathbb{S}_2(x) + \beta_4 y^4 \mathbb{S}_4(x) + \beta_6 y^6 \mathbb{S}_6(x) - \frac{7}{2}\gamma y^7 \mathbb{S}_0(x) \tag{6.43}$$
$$- \frac{1}{112}\widehat{\mu}^2 y^5 \big(7\mathbb{S}_0(x) + 18\mathbb{S}_2(x)\big) - \frac{1}{840}\alpha_1 \widehat{\mu} y^7 \big(315\mathbb{S}_0(x) + 184\mathbb{S}_2(x)\big)$$
$$- \frac{1}{41184}\beta_2 \widehat{\mu}^2 y^7 \big(819\mathbb{S}_0(x) + 24978\mathbb{S}_2(x) + 22160\mathbb{S}_4(x)\big) + O(y^8)\,,$$
$$\Omega(x,y) = 1 - \beta_2 y^2 \mathbb{S}_2(x) - \beta_4 y^4 \mathbb{S}_4(x) - \beta_6 y^6 \mathbb{S}_6(x) + \frac{9}{14}\left(\gamma - \delta\right) y^7 \mathbb{S}_0(x) \tag{6.44}$$
$$+ \frac{7}{143}\beta_2^2 y^4 \big(91\mathbb{S}_0(x) + 22\mathbb{S}_2(x) + 30\mathbb{S}_4(x)\big) + \frac{1}{560}\widehat{\mu}^2 y^5 \big(50\mathbb{S}_2(x) - 133\mathbb{S}_0(x)\big)$$
$$- \frac{49}{2431}\beta_2^3 y^6 \big(238\mathbb{S}_0(x) + 561\mathbb{S}_2(x) + 180\mathbb{S}_4(x) + 126\mathbb{S}_6(x)\big)$$
$$+ \frac{14}{1105}\beta_2\beta_4 y^6 \big(612\mathbb{S}_2(x) + 220\mathbb{S}_4(x) + 273\mathbb{S}_6(x)\big) + \frac{3}{280}\alpha_1 \widehat{\mu} y^7 \big(35\mathbb{S}_0(x) + 16\mathbb{S}_2(x)\big)$$
$$+ \frac{1}{205920}\beta_2 \widehat{\mu}^2 y^7 \big(-257985\mathbb{S}_0(x) + 39726\mathbb{S}_2(x) + 13600\mathbb{S}_4(x)\big) + O(y^8)\,,$$
$$Q(x,y) = 1 + \gamma y^7 \mathbb{S}_0(x) \tag{6.45}$$
$$- \frac{1}{16}\widehat{\mu}^2 y^5 \mathbb{S}_0(x) + \frac{2}{147}\alpha_1 \widehat{\mu} y^7 \mathbb{S}_2(x) + \frac{1}{48048}\beta_2 \widehat{\mu}^2 y^7 \big(4054\mathbb{S}_2(x) + 665\mathbb{S}_4(x)\big) + O(y^8)\,.$$

Next let us consider tensor perturbations. These arise from the fields T_1, T_2 and T_3, which we can write as

$$T_1 \frac{4dx^2}{2-x^2} + T_2\, x^2(2-x^2)d\Omega_2^2 + T_3(1-x^2)^2 d\Omega_5^2 \equiv Q d\Omega_8^2 + T_{ij} d\theta^i d\theta^j\,, \tag{6.46}$$

where θ^i denotes coordinates on S^8 and the symmetric tensor T_{ij} is traceless with respect to the S^8 metric h_{ij}, i.e.

$$h^{ij}T_{ij} = 0\,, \qquad d\Omega_8^2 = h_{ij}d\theta^i d\theta^j\,. \tag{6.47}$$

The trace part of these tensor perturbations is given by the function Q already considered in the scalar perturbations above. The modes that appear in the symmetric traceless tensor T_{ij} can be divided in their divergence and divergence-less parts. The divergence part is obtained by acting on the scalar harmonics with the differential operator

$$\triangle_{ij} = \nabla_i \nabla_j - \frac{1}{8}h_{ij}\Delta\,, \tag{6.48}$$

where $\Delta = \nabla^i \nabla_i$ is the S^8 Laplacian. These are, however, the same modes described above for scalar perturbations. In fact, their appearance in the tensor perturbations can be gauge away by imposing the gauge condition $\nabla^i T_{ij} = 0$. However, here they will be present in the tensor

perturbations, since we do not have such freedom, because in the DeTurck method a given gauge choice is imposed on us.[9] The divergence-less part of these tensor perturbations comes again with non-normalizable and normalizable modes. We drop the non-normalizable modes and, for present purposes, we can neglect the normalizable modes because at linear level they appear first at order y^9. Working up to order y^7, the expansion of tensor perturbations reads

$$T_{ij}(x,y) = -\frac{1}{2352}\widehat{\mu}^2 y^5\big(16\Delta_{ij}\mathbb{S}_2(x) - 945(\mathbb{T}_2)_{ij}(x)\big) + \frac{15}{28}\alpha_1\widehat{\mu}y^7(\mathbb{T}_2)_{ij}(x) \tag{6.49}$$
$$-\frac{1}{144144}\beta_2\widehat{\mu}^2 y^7\big(968\Delta_{ij}\mathbb{S}_2(x) - 110\Delta_{ij}\mathbb{S}_4(x) - 24675(\mathbb{T}_2)_{ij}(x) + 187110(\mathbb{T}_4)_{ij}(x)\big) + O(y^8)\,,$$

where the $(\mathbb{T}_l)_{ij}$ are S^8 harmonic tensors that satisfy

$$h^{ij}(\mathbb{T}_l)_{ij} = 0\,, \qquad \nabla^i(\mathbb{T}_l)_{ij} = 0\,,$$
$$\Delta(\mathbb{T}_l)_{ij} = -\lambda_l(\mathbb{T}_l)_{ij}\,, \qquad \lambda_l = l(l+7) - 2\,, \tag{6.50}$$

with $l \geq 2$ and with l even to guarantee invariance under the $SO(3)\times SO(6)$ subgroup. Explicitly these harmonics are given by

$$(\mathbb{T}_l)_{ij}d\theta^i d\theta^j = \mathbb{R}_l(x)\,\frac{4dx^2}{2-x^2} + \mathbb{U}_l(x)\,x^2(2-x^2)d\Omega_2^2 + \mathbb{V}_l(x)(1-x^2)^2 d\Omega_5^2\,, \tag{6.51}$$

where

$$\mathbb{R}_l(x) = {}_2F_1\left(1-\frac{l}{2},\frac{9+l}{2},\frac{5}{2},x^2\left(2-x^2\right)\right), \tag{6.52}$$

$$\mathbb{U}_l(x) = \left(1-8x^2+4x^4\right)\mathbb{R}_l(x)$$
$$-\frac{(l-2)(l+9)}{10}x^2\left(2-x^2\right)\left(1-x^2\right)^2\,{}_2F_1\left(2-\frac{l}{2},\frac{11+l}{2},\frac{7}{2},x^2\left(2-x^2\right)\right), \tag{6.53}$$

$$\mathbb{V}_l(x) = -\frac{1}{5}\big(\mathbb{R}_l(x) + 2\mathbb{U}_l(x)\big)\,. \tag{6.54}$$

Notice that, although an independent tensorial normalizable mode of spin l appears first at order y^{7+l}, these tensor perturbations already make their appearance at lower orders through the back-reaction.

Finally let us consider vector perturbations. For our Ansatz, F is the single $SO(9)$ vector. It turns out that there are no divergence-less vectors on S^8 that are $SO(3)\times SO(6)$ invariant. Thus the expansion of this field will only contain derivatives of the scalar perturbations, which is indeed

[9] Thus, a gauge transformation is necessary to make the precise map between our expansion and that of [73].

confirmed by the expansion

$$y^{-1}F(x,y) = \frac{1}{42}\widehat{\mu}^2 y^5 \partial_x \mathbb{S}_2(x) + \frac{3}{98}\alpha_1 \widehat{\mu} y^7 \partial_x \mathbb{S}_2(x) - \frac{1}{144144}\beta_2 \widehat{\mu}^2 y^7 \big(6862\partial_x \mathbb{S}_2(x) - 1155\partial_x \mathbb{S}_4(x)\big) + O(y^8)\,. \tag{6.55}$$

All constants in the above expansions that remain to be determined correspond to expectation values of dual operators in the matrix model. Up to order y^7 in the above expansions, these are the constants α_1, α_3, α_5 and β_2, β_4, β_6 and γ, δ. More normalizable modes show up at higher order, but we decided to only present results for these.

For a more accurate numerical extraction of the remaining normalizable modes, we do a final change of variables that will ease the numerical procedure, namely we define

$$\begin{aligned} &A = 1 + y^2 Q_1\,, \quad B = 1 + y^5 Q_2\,, \quad F = 2y^6\sqrt{1-y}\left[\frac{\widehat{\mu}^2}{84}\partial_x \mathbb{S}_2(x) + y\, Q_3\right]\,, \\ &T_1 = 1 + y^5 Q_4\,, \quad T_2 = 1 + y^5 Q_5\,, \qquad T_3 = 1 + y^5 Q_6\,, \quad T_4 = 1 + y^2 Q_7\,, \quad \Omega = 1 + y^2 Q_8\,, \\ &M = (1-y)y^{-3}\,\mathbb{H}_1(x)\left[\widehat{\mu}\,\frac{1-y^7}{1-y} + y^5 Q_9\right]\,, \qquad L = \frac{3}{2}y^4\,\mathbb{H}_1(x)\left[\widehat{\mu} + y^2 Q_{10}\right]\,. \end{aligned} \tag{6.56}$$

Our numerical procedure aims to solve for all ten $Q_i(x,y)$. We impose the following Neumann and Dirichlet boundary conditions at $y = 0$

$$\begin{aligned} &\partial_y Q_1 = \partial_y Q_{10} = Q_7 + Q_1 = Q_8 - Q_1 = 0\,, \qquad Q_2 = \frac{\widehat{\mu}^2}{2}\,, \\ &Q_3 = \frac{\widehat{\mu}^2}{168}\partial_x \mathbb{S}_2(x)\,, \qquad Q_9 = \frac{3}{176}\widehat{\mu}^3\left(65\frac{\mathbb{H}_3(x)}{\mathbb{H}_1(x)} - 43\right)\,, \\ &Q_4\frac{4dx^2}{2-x^2} + Q_5 x^2(2-x^2)d\Omega_2^2 + Q_6(1-x^2)^2 d\Omega_5^2 = \frac{\widehat{\mu}^2}{2351}\big(945(\mathbb{T}_2)_{ij}(x) - 16\Delta_{ij}\mathbb{S}_2(x)\big)d\theta^i d\theta^j\,. \end{aligned} \tag{6.57}$$

These boundary conditions guarantee that all non-normalizable modes (except $\widehat{\mu}$) are set to zero. In particular, the mode $\widetilde{\beta}_2$ is the hardest to exclude because it only appears at order y^5 in the asymptotic expansion. For example, a non-zero $\widetilde{\beta}_2$ would give rise to

$$Q_2(x,y) = \frac{\widehat{\mu}^2}{2} + \widetilde{\beta}_2 \mathbb{S}_2(x) + O(y)\,. \tag{6.58}$$

Therefore, the boundary conditions (6.57) force $\widetilde{\beta}_2 = 0$.

Symmetry axes

The boundary conditions at the equator $x = 0$ are just those obtained via smoothness of the solutions. This implies that all Q_i should be even functions of x, except Q_3, which should be odd

under $x \to -x$. Moreover, we must have $Q_4 = Q_5$ at $x = 0$ to avoid a conical deficit. In practice, we just impose

$$Q_4(0,y) = Q_5(0,y)\ , \qquad Q_3(0,y) = 0\ , \qquad \partial_x Q_i(x,y)|_{x=0} = 0\,, \quad i = 1,2,5,\ldots,10\,. \tag{6.59}$$

Similarly, at the $x = 1$ pole, we require that F is odd and

$$A,\ B,\ T_4,\ \Omega,\ M,\ L,\ \frac{T_1}{2-x^2},\ (2-x^2)T_2,\ (1+x)^2 T_3 \tag{6.60}$$

are even under reflection around $x = 1$. Moreover, we avoid conical deficits by imposing

$$Q_4(1,y) = Q_6(1,y)\,. \tag{6.61}$$

These conditions imply $\xi^x = 0$ at $x = 0$ and $x = 1$.

At the horizon, which in the Euclidean setting is also a symmetry axis, regularity is easier to impose after changing to a new radial coordinate via $1 - y = (1 - \widetilde{y})^2$. In the $\widetilde{y}$ coordinate, the conditions for regularity are that F is odd and all other functions are even under reflection around $\widetilde{y} = 1$. Moreover, we impose $A = B$ at $\widetilde{y} = 1$ to avoid conical deficits with the periodicity $\Delta\eta = 4\pi/7$. In practice, we use the boundary conditions

$$Q_1(x,\widetilde{y}=1) = Q_2(x,\widetilde{y}=1)\ , \qquad \partial_{\widetilde{y}} Q_i(x,\widetilde{y})\big|_{\widetilde{y}=1} = 0\,, \quad i = 2,3,\ldots,10\,. \tag{6.62}$$

These boundary conditions imply $\xi^{\widetilde{y}} = 0$.

It is a relatively easy exercise to show that the boundary conditions detailed above, together with the Einstein-DeTurck equations, form a well posed Elliptic problem [74, 75]. Furthermore, at the fictitious boundaries $x = 0$, $x = 1$, and $\widetilde{y} = 1$, the boundary conditions induced on ξ are the relevant ones to admit $\xi = 0$, *i.e.* Einstein solutions, everywhere in the bulk [25]. We are thus ready to present our results and to detail the numerical method we used to solve the Harmonic Einstein equations.

6.3.3 Smarr formulae

A conserved two form of the solution (6.15) is

$$(K_v)^{ab} = \nabla^a v^b + \frac{1}{4} G^{abcd} v^e C_{cde} + \frac{1}{18} v^{[a} G^{b]cde} C_{cde}\ . \tag{6.63}$$

Conservation of this tensor follows from the equations of motion (6.26), $\nabla^a G_{abcd} = 0$, and from the identities

$$\mathcal{L}_v g = \mathcal{L}_v C = \mathcal{L}_v G = 0 \ , \qquad \nabla_b \nabla^b v_a = -R_{ab} v^b \ . \tag{6.64}$$

We can now relate observables at the horizon to those at the boundary for this ansatz by using the machinery developed in section 4.4. Choosing $v = \frac{\partial}{\partial \eta}$ to be the generator of time translations, the resulting expression is

$$\frac{7}{2}\widehat{S} = \frac{8\pi^5}{3465}\left(924 + 2640\gamma + 594\delta - 220\alpha_1\widehat{\mu} + 119\beta_2\widehat{\mu}^2\right) . \tag{6.65}$$

To compute $I_v(1)$ we used the fact that the horizon is a Killing horizon of $\frac{\partial}{\partial \eta}$ with surface gravity equal to $\frac{7}{2}$. To compute $I_v(0)$ we used the asymptotic expansion of the fields.

Choosing instead $v = \frac{\partial}{\partial \zeta}$ to be the generator of translations along the M-theory circle, we obtain

$$1 = \frac{105}{64\pi^5}\int_{\mathcal{H}} d^9x\sqrt{h}\left(\frac{T_4(1,x)\Omega(1,x)}{A(1,x)} - \frac{L(1,x)\partial_y M(1,x)}{7x^4(2-x^2)^2 A(1,x)T_2^2(1,x)}\right) , \tag{6.66}$$

where the integration measure, given in (6.20), is defined by the horizon metric. This integral measures the momentum along the M-theory circle (or D0-brane charge in the type IIA picture) which is constant as we vary $\widehat{\mu}$. We can think of the first term in (6.66) as the momentum carried by the black string, and the second term, which is also positive, is the momentum carried by the matter fields outside the horizon. In Fig. 6.4 we plot the momentum carried by the black string. As $\widehat{\mu}$ increases the momentum carried by the fields outside the horizon increases.

It is also useful to integrate the $d(\star K_v)$ over the 10-dimensional surface of constant ζ. By a similar argument as the one above, we conclude that the following integral is independent of y

$$\widetilde{I}_v(y) = \int_{\widetilde{\Gamma}(y)} \star K_v \ , \tag{6.67}$$

where $\widetilde{\Gamma}(y)$ is the 9-dimensional surface of constant y and ζ. Choosing $v = \frac{\partial}{\partial \zeta}$ we obtain $\widetilde{I}_v(1) = 0$ from the behaviour of the solution at the horizon. Thus, using the behaviour as $y \to 0$, we deduce the following identity

$$\gamma + \frac{5}{44}\delta - \frac{1}{132}\alpha_1\widehat{\mu} - \frac{287}{5808}\beta_2\widehat{\mu}^2 = 0 \, , \tag{6.68}$$

relating the parameters of the asymptotic expansion of the fields.

For $v = \frac{\partial}{\partial \eta}$ we also obtain $\widetilde{I}_v(1) = 0$. However, $\widetilde{I}_v(0)$ depends on higher orders of y in the asymptotic expansion of the fields than those considered above.

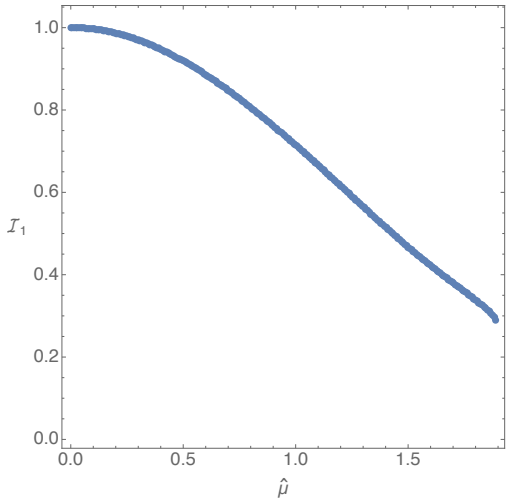

Figure 6.4: Momentum along the M-theory circle carried by the black string (first term in right hand side of (6.66)). As $\widehat{\mu}$ increases, the black string and the fields outside the horizon carry less and more momentum, respectively, keeping the total momentum of the geometry fixed.

6.3.4 Numerical Solution

We used a standard pseudospectral collocation in x and $\widetilde{y}$, and solved the resulting system of non-linear algebraic equations with a damped Newton-Raphson method. The dependence in x and $\widetilde{y}$ of all the functions was represented using tensor products of two Chebyshev collocation grids, each of which living on the unit interval $(0, 1)$. Our integration domain is thus a square $(x, \widetilde{y}) \in (0, 1) \times (0, 1)$.

In expanding the functions Q_i around the relevant boundaries, we have found no sign of non-smoothness. This means that a priori we expect the convergence of our method to be exponential in the number of grid points $\mathcal{N}$ and that no patching procedure is required. The only delicate numerical problem associated with these equations is that we need to accurately extract third and fourth derivatives off of the conformal boundary, in order to read the several constants corresponding to normalizable modes. For this reason, we decided to work with octuple precision and no less than 51 grid points on each integration domain. In addition, due to the very bad condition numbers of the matrices we have to invert, we found useful to use up to twelve patches close to the boundary (depending on the values of $\widehat{\mu}$ and how steep our functions behave). These are conforming patches, which are patches that only coincide along a line, and have no overlapping regions. Since we are interested in accurately extracting asymptotic quantities, our patches coincide with lines of constant

$\widetilde{y}$ and cluster close to $\widetilde{y} = 0$.

In order to monitor the convergence of our numerical method, we monitored $\chi = \|\xi^a\|_\infty$ as a function of the number of grid points $\mathcal{N}$, as well as

$$\Delta_{\mathcal{N}} = \left| 1 - \frac{\widehat{S}_{\mathcal{N}}}{\widehat{S}_{\mathcal{N}+1}} \right| , \tag{6.69}$$

where $\widehat{S}_{\mathcal{N}}$ denotes the entropy computed with $\mathcal{N}$ grid points in both directions. Both plots are displayed in Fig. 6.5, where a linear-logarithmic scale is used and we set $\widehat{\mu} = 1$. The results are consistent with exponential convergence, as dictated by pseudospectral collocation methods.

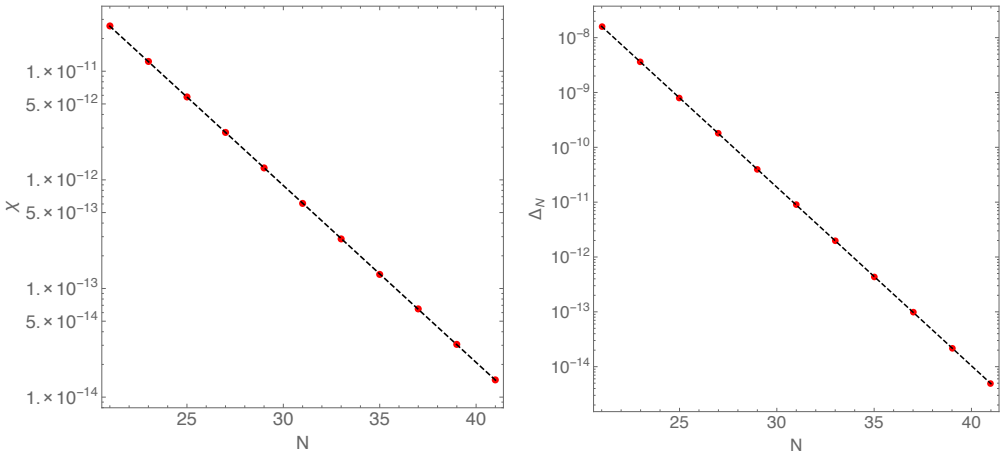

(a) Plot of χ, as a function of $\mathcal{N}$.

(b) Plot of $\Delta_{\mathcal{N}}$, as a function of $\mathcal{N}$.

Figure 6.5: Convergence plots for fixed $\widehat{\mu} = 1$.

A perhaps more striking test of our numerics comes from the identity (6.68). We have checked that this relation is obeyed by our numerical data, never exhibiting a violation above $10^{-6}\%$. Similarly, we checked that the Smarr formulas (**??**) and (6.66) are verified by our numerical solutions with an accuracy of $10^{-6}\%$. The Smarr formulae provide a very non-trivial validation of our numerical results because they relate quantities measured at the horizon ($y = 1$) to quantities measured at infinity ($y = 0$). This gives us full confidence that our numerical procedure is accurate enough for the physics we want to extract.

In Fig. 6.6 we plot a typical run of our numerical method. It shows the behavior of Q_1, Q_9 and Q_{10} as a function of x and y. Note that these are all gauge invariant. From these plots we can easily see why we needed octuple precision, namely there is a large hierarchy between the functions.

For instance, Q_9 evaluated on the horizon appears to be larger than all the remaining functions. This problem becomes worse as we increase $\widehat{\mu}$.

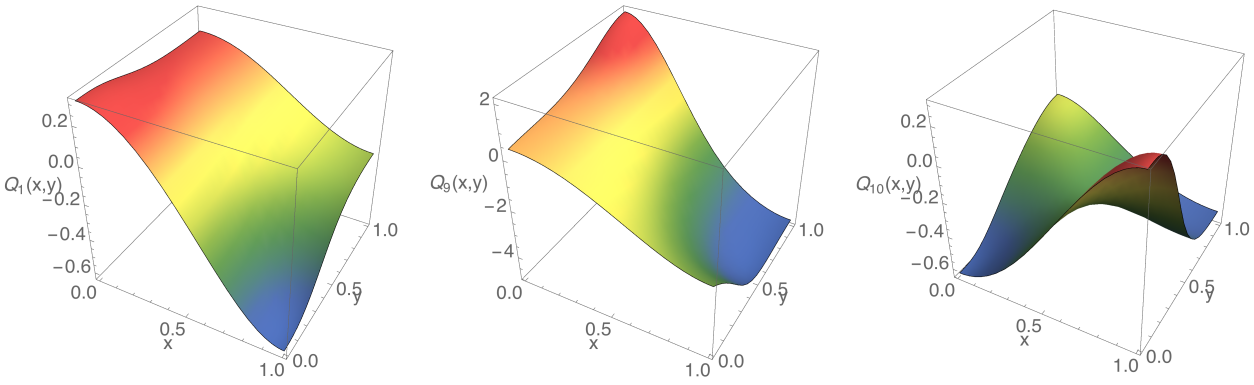

Figure 6.6: From left to right: three-dimensional plots of Q_1, Q_9 and Q_{10} as a function of x and y for fixed $\widehat{\mu} = 1$.

We now turn to more physical quantities. In particular, we would like to see how the horizon shape is changing as we change $\widehat{\mu}$. It is clear that the geometry will slowly move from having a round S^8 with $SO(9)$ symmetry to a deformed S^8 with a manifest $SO(3) \times SO(6)$. To explicitly quantify how deformed the horizon is from full spherical symmetry, we measure the radius of the S^2 at the pole and the radius of the S^5 at the equator. If the ratio between these quantities is very small, the horizon is highly distorted from spherical symmetry. We plot this quantity in Fig. 6.7a.

The fact that this ratio reaches such small values might be worrying and suggestive of a Gregory-Laflamme type instability along the S^5 directions. In order to settle this, one would need to perturb this solution, and check its dynamical stability. We are currently undertaking this study, but have no results to report. Finally, we can also plot the normalized area of the horizon as a function of $\widehat{\mu}$, which we will need to reconstruct the free energy. This is done in Fig. 6.7b, where we see the horizon area decreasing with increasing $\widehat{\mu}$.

We finalize this section by presenting, in Fig. 6.8, the several extracted expectation values as a function of $\widehat{\mu}$. We obtain these expectation values by computing the first few y-derivatives at $y = 0$ of the functions $Q_i(x, y)$ and fitting them to the asymptotic expansions discussed in section 6.3.2. The predictions determined by perturbations around the $\widehat{\mu} = 0$ background are shown in this figure as dashed red lines. Any Monte Carlo simulation of the PWMM (6.5) should hope to reproduce

these results.

6.4 Thermodynamics

Our numerical solution, expressed in terms of the functions in the Ansatz (6.15), depends on a single dimensionless parameter $\widehat{\mu}$ that determines the asymptotic behaviour of the 3-form potential C through the boundary condition (6.23). Thus, the corresponding on-shell dimensionless action $\widehat{I}$ and entropy $\widehat{S}$, respectively defined in (6.18) and (6.19), are functions of this single parameter. The boundary conditions imposed at the horizon fixed the periodicity of the Euclidean time circle to $4\pi/7$, independently of $\widehat{\mu}$.

Next, to obtain physical solutions from the above single-parameter family of solutions, we scaled the metric by r_0^2 and the 3-form C by r_0^3, and changed the period of the M-theory circle according to (6.17). The new family of solutions, parametrized by $\widehat{\mu}$ and r_0, has the same leading asymptotics of the non-extremal D0-brane solution (6.2) with an additional 3-form potential C with asymptotic behaviour (6.24). It is then convenient to parametrize this new family of solutions by the temperature T and the mass deformation μ, which are related to the original single parameter by $\widehat{\mu} = \frac{7}{12\pi}\frac{\mu}{T}$ as derived in (6.25). Moreover, the on-shell action and entropy of the two-parameter

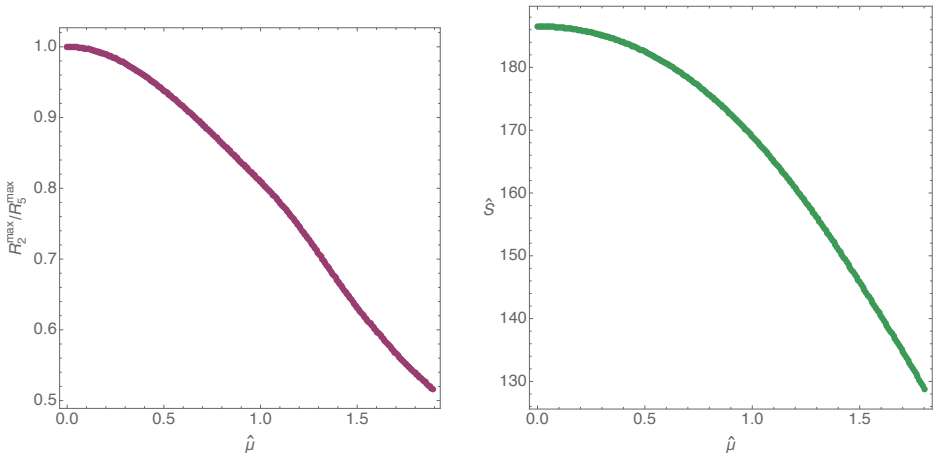

(a) Ratio of the maximum size of the S^2, over(b) Normalized horizon area as a function of the maximum size of the S^5, as a function of$\widehat{\mu}$.

$\widehat{\mu}$.

Figure 6.7: Extracted physical quantities plotted as a function of $\widehat{\mu}$.

and single-parameter families of solutions are simply related by (6.18) and (6.19), which we can rewrite in the form

$$F(T,\mu) = -c_0\, T^{\frac{14}{5}}\, \widehat{I}(\widehat{\mu})\,, \qquad S(T,\mu) = c_0\, \frac{14}{5}\, T^{\frac{9}{5}}\, \widehat{S}(\widehat{\mu})\,, \tag{6.70}$$

for a known (dimensionfull) constant c_0. In the particular case of zero mass deformation $\mu = 0$ we recover the scaling with temperature as predicted directly from the matrix quantum mechanics in [53, 54]. It is then clear that both the free energy and entropy are restricted to satisfy

$$\frac{F(T,\mu)}{F(T,0)} = \frac{\widehat{I}(\widehat{\mu})}{\widehat{I}(0)} \equiv f(\widehat{\mu})\,, \qquad \frac{S(T,\mu)}{S(T,0)} = \frac{\widehat{S}(\widehat{\mu})}{\widehat{S}(0)} \equiv s(\widehat{\mu})\,, \tag{6.71}$$

where, by definition, $f(0) = s(0) = 1$.

The behaviour of the free energy and entropy (6.71), together with the scaling of the free energy as $T^{\frac{14}{5}}$ at zero mass deformation $\widehat{\mu}$, can be used in the first law

$$\left(\frac{\partial F}{\partial T}\right)_{\mu} = -S\,, \tag{6.72}$$

to relate the functions $f(\widehat{\mu})$ and $s(\widehat{\mu})$. This leads to the following equation

$$\left(1 - \frac{5}{14}\,\widehat{\mu}\,\frac{\partial}{\partial \widehat{\mu}}\right) f(\widehat{\mu}) = s(\widehat{\mu})\,, \tag{6.73}$$

which can easily be integrated

$$f(\widehat{\mu}) = -\frac{14}{5}\,\widehat{\mu}^{\frac{14}{5}}\left[C + \int^{\widehat{\mu}} dx\, x^{-\frac{19}{5}}\, s(x)\right], \tag{6.74}$$

where we wrote explicitly the integration constant C. Notice that the boundary condition $f(0) = 1$ does not determine the constant C. However, assuming that both $s(\widehat{\mu})$ and $f(\widehat{\mu})$ are analytic around $\widehat{\mu} = 0$, and therefore have a regular Taylor series expansion, removes all ambiguity,

$$s(\widehat{\mu}) = \sum_{n=0}^{\infty} s_n\, \widehat{\mu}^n \qquad \Rightarrow \qquad f(\widehat{\mu}) = \sum_{n=0}^{\infty} \frac{14 s_n}{14 - 5n}\, \widehat{\mu}^n\,. \tag{6.75}$$

Since from computing the horizon area we know the function $s(\widehat{\mu})$ numerically, we can do a polynomial fit to determine the first coefficients s_n, and then use it to plot $f(\widehat{\mu})$ in Fig. 6.9. The most important feature of this plot is that f vanishes for $\widehat{\mu} = \widehat{\mu}_c \approx 1.7532672$. This means that, for $\widehat{\mu} > \widehat{\mu}_c$, the free energy of the deconfined phase of the PWMM is positive and of order N^2. Therefore, the confined phase that has a free energy of order N^0 will be smaller and dominate the

thermal ensemble. In other words, the critical temperature for the phase transition is [10]

$$\frac{T_c}{\mu} = \frac{7}{12\pi\widehat{\mu}_c} = 0.105905(57)\,. \tag{6.76}$$

Let us now consider thermodynamical stability. The specific heat of the system is given by

$$c = T\left(\frac{\partial S}{\partial T}\right)_{\mu}\,. \tag{6.77}$$

From (6.70) and (6.71) we may also express the specific heat in terms of the function $s(\widehat{\mu})$ as

$$\frac{c}{S} = \frac{9}{5} - \widehat{\mu}\,\frac{\partial}{\partial\widehat{\mu}}\log s(\widehat{\mu})\,. \tag{6.78}$$

Since in the range the black hole geometry is thermodynamically favoured, $s(\widehat{\mu})$ is a decreasing function, as shown in Fig. 6.7b, we conclude that the specific heat is always positive and therefore our solution is thermodynamically stable in this range.

6.5 Discussion

Our main result is the construction of the black hole geometry dual to the deconfined phase of the PWMM. This allowed us to determine the value of the critical temperature at strong coupling as depicted in the phase diagram 6.1. In addition, we determine the thermal expectation values of several observables in the deconfined phase (see Fig. 6.8).

At this point we would like to discuss an important caveat that we disregarded in the main text. There should be many black hole geometries with different horizon topologies and the same asymptotics as the solution we constructed. One can think of these as the finite temperature and backreacted versions of the many ways to distribute spherical probe M5 and M2 branes in equilibrium in the M-theory plane wave [6, 76]. These solutions are in one-to-one correspondence with the many vacua of the PWMM [77]. Our expectation is that the solution with lower free energy in the high temperature limit is the one we found because it has the simplest horizon topology. However, as we decrease the temperature it is possible that other black hole solutions start to dominate the thermal ensemble.[11] Therefore, what we really determined was an upper bound for the critical temperature for the deconfinement transition. Notice that it is sufficient to find one

[10] We present the critical temperature with 6 digits because our numerical solutions satisfied the Smarr formulas with $10^{-6}\%$ accuracy and the polynomial fit in (6.75) decreases precision by one order of magnitude.

[11] Such behavior has been observed at weak coupling in simulations of the PWMM [65].

black hole solution with negative free energy at a given temperature to conclude that the system must be in the deconfined phase at that temperature. Even if this solution is dynamically unstable it must decay to another solution with lower free energy, thus the system remains in the deconfined phase.

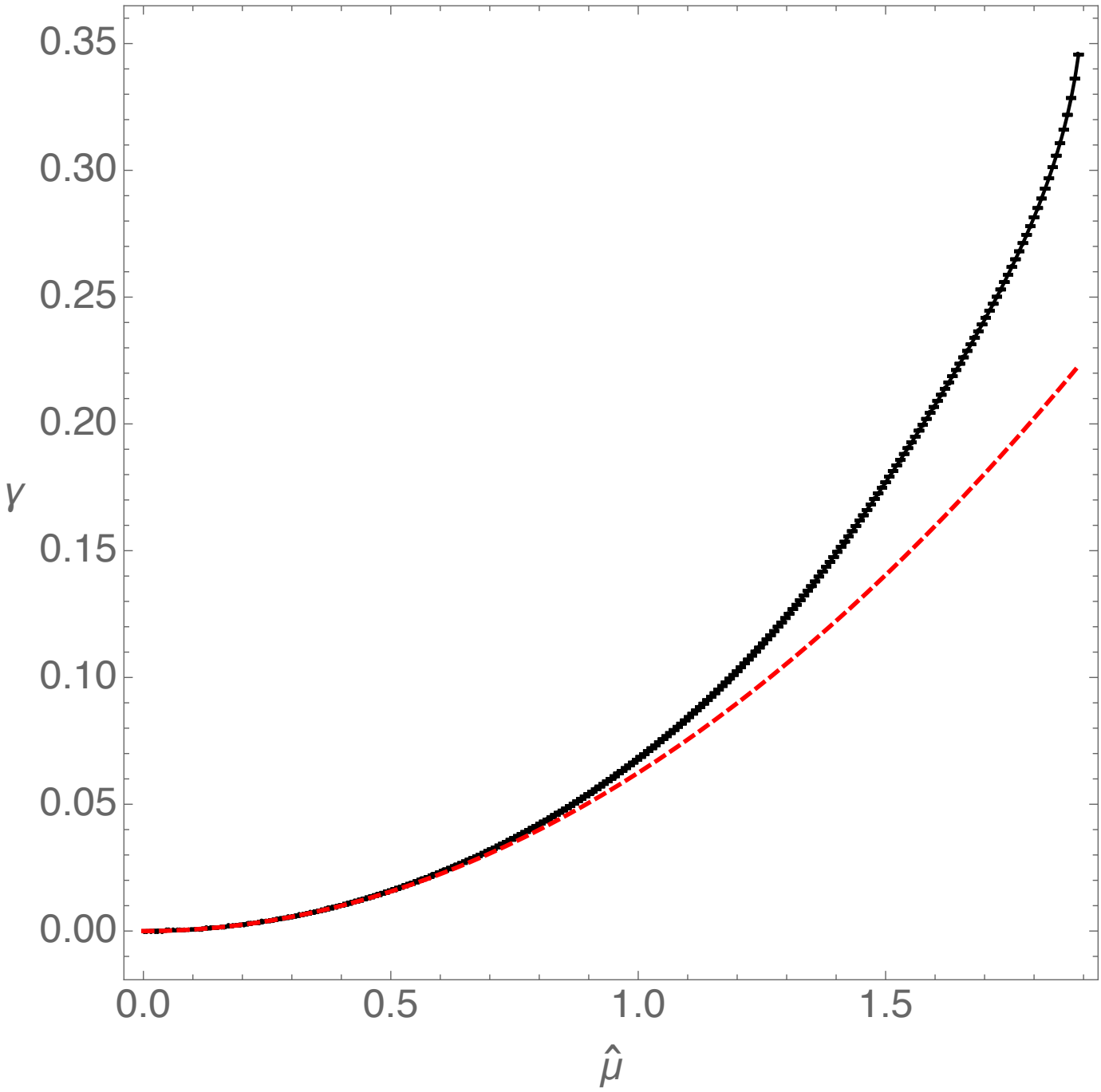

Figure 6.8: α_1, β_2, γ, δ, α_3 and β_4 as a function of $\widehat{\mu}$. These plots contain error bars, obtained via a standard χ^2 fit, which become increasingly larger as $\widehat{\mu}$ increases. The red dashed lines are the prediction up to order $\widehat{\mu}^2$, obtained from the study of perturbations around the $\widehat{\mu} = 0$ exact background (α_3 and β_4 vanish to this order in $\widehat{\mu}$).

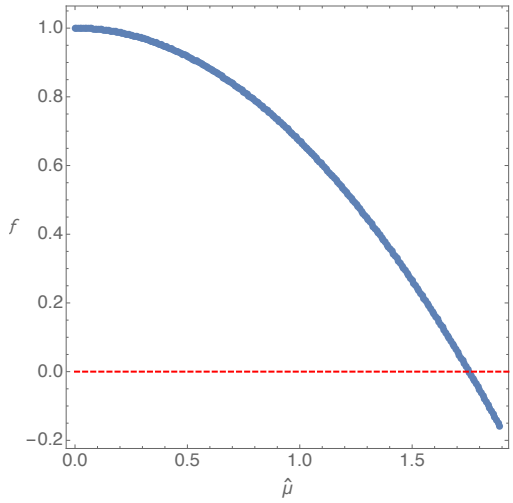

Figure 6.9: The free energy ratio $f(\widehat{\mu})$ obtained numerically using (6.75).

Chapter 7

Conclusion and Future Directions

In this thesis, we applied contemporary numerical techniques to study deformed geometries in the context of the gauge/gravity duality. In chapter two, we gave an overview of the gauge/gravity duality, highlighting the gravitational side of the correspondence as well as introducing the boundary observables we would use throughout the text. In chapter three, we discussed the numerical methods used to solve the Einstein equations in the bulk. In this chapter we introduced the generalized harmonic Einstein equations and detailed the spectral methods we would use to solve them.

In chapter four, we put these numerical methods to use to study the deformed black hole and soliton solutions that result from placing a dipolar potential in an AdS background. These geometries have a phase space parametrized by the electric field magnitude $\mathcal{E}$ and the temperature T. The corresponding phase diagram generalizes that of the Hawking-Page first-order phase transition for Schwarschld-AdS black holes. We found that both black holes and solitons exist for an arbitrarily high value of the electric field. This is in contradiction with the weak coupling phase diagram of a free boson, which we argued has a critical electric field, beyond which the solutions become unstable.

In order to study an example of polarized black holes with a field theory dual, we coupled the polarized geometries discussed previously to a neutral scalar field. In chapter five, we studied such asymptotically AdS geometries in Einstein-Maxwell-dilaton theory subject to the same dipolar potential. These are dual to deformed ABJM theory in three dimensions. In this chapter, we gave a brief overview of ABJM theory and used numerical methods to construct its gravity duals. We found results similar to the scalar free case, with two classes of solutions corresponding to black hole

and horizonless geometries. In contrast, this theory has the addition of a maximum electric field, indicating a qualitatively similar behavior to the weak coupling picture. It is possible that deformed ABJM theory can be compactified on the S^2 and simulated using Monte Carlo techniques. Such an undertaking could not only confirm our results at strong coupling, but also provide another test of the gauge/gravity duality. This is an exciting prospect and would be interesting work for the future.

In chapter six, we constructed the black hole solutions dual to the BMN matrix model. These are deformed geometries in 11D supergravity with a phase space parametrized by the temperature of the horizon and the coupling. In addition, the BMN matrix model is a $0+1$-dimensional theory that is easier to simulate on a computer using Monte Carlo techniques. Thus, the phase diagram constructed in this chapter is a concrete prediction for the phase transition of the BMN matrix model at strong coupling that can be tested directly in the strongly-coupling regime.

We hope our results motivate others to start a systematic exploration of the phase diagram of the PWMM by direct simulation of the matrix quantum mechanics, e.g. using the Monte-Carlo methods of [59, 60, 61, 4, 5]. In fact, there has been a preliminary Monte-Carlo simulation of the PWMM [11]. In this work, the authors simulate the PWMM at fixed temperature ($T/\mu = 1/3$ in our conventions) and as they vary the coupling, they observe a first order phase transition for $0.03 \lesssim g \lesssim 0.045$. This result is not in direct contradiction with our results but it implies a non-monotonic behaviour of the critical temperature as a function of the coupling g, complicating the phase diagram 6.1. Another Monte Carlo simulation is currently underway [78] which treats the temperature, mass parameter, and 't Hooft coupling individually, allowing for a more systematic survey of the phase space. We look forward to comparing our prediction with these results very soon.

Our work provides concrete predictions for the behaviour of several thermodynamic quantities at strong coupling in the deconfined phase. We also provide predictions for thermal expectation values of several operators. However, the precise map between the gravitational parameters shown in Fig. 6.8 and operators of the PWMM is still missing. This map is known [73] in the limit $\mu \to 0$ but its extension to finite μ requires the development of holographic renormalization with plane-wave asymptotics.

It would also be very interesting to perform a Multicanonical Monte-Carlo simulation [79, 80, 81]

of the PWMM that could measure the density of states of the system. This would provide a window into the thermodynamics of the system in the microcanonical ensemble, which is expected to have a richer structure, including a Hagedorn phase.[1]

Our black hole solution was constructed starting from the limit $\mu/T = 0$. It would be interesting to understand our solution in the opposite limit $\mu/T \to \infty$. It is hard to address this question using our numerical methods because the black hole becomes very deformed and requires a much finer discretization grid. In any case, Fig. 6.7a suggests that when $\mu \gg T$ the black hole looks like a pancake (more precisely, a large 6D ball with a small thickness in the transverse 3 directions, times the M-theory circle). It should be possible to study this limit analytically using the blackfold approach of [82]. The large deformation of the horizon also suggests that the system might be unstable to a topology change to a ring-like horizon with $S^5 \times S^3 \times S^1$ topology. It should also be possible to study the low temperature regime of such black holes using the blackfold approach. We leave these ideas for the future.

[1] We thank Eliezer Rabinovici for emphasizing this point.

Appendix A

Perturbative Analysis for Chapter 4

In order to get an analytic understanding of our results for small electric field $\mathcal{E}$ and also to test our numerical results, we performed a perturbative expansion to $\mathcal{E}^3$. Higher orders can be readily obtained, but the functions involved in the expansion become increasingly more complicated.

We start by detailing the generic procedure, which should be valid to any order in perturbation theory. Since the stress energy tensor is even in the Maxwell field, the expansion in powers of $\mathcal{E}$ will take the following schematic form

$$g_{\mu\nu} = \overline{g}_{\mu\nu} + \sum_{j=1}^{+\infty} g_{\mu\nu}^{(2j)} \mathcal{E}^{2j} \,, \qquad \mathcal{A}_\mu = \sum_{j=0}^{+\infty} a_\mu^{(2j+1)} \mathcal{E}^{2j+1} \,. \tag{A.1}$$

We are interested in solutions where the only nontrivial component of the Maxwell field is $\mathcal{A}_t$. Furthermore, for $\overline{g}$ we choose AdS_4 written in global coordinates with standard spherical coordinates, *i.e.*

$$\overline{g}_{\mu\nu} dx^\mu dx^\nu = -\left(1 + \frac{r^2}{l^2}\right) dt^2 + \frac{dr^2}{1+\frac{r^2}{l^2}} + r^2 \left[\frac{d\chi^2}{1-\chi^2} + (1-\chi^2) d\phi^2\right] , \tag{A.2}$$

where $\chi \in [-1, 1]$ can be related to the standard polar coordinate as $\chi = \cos\theta$, and we reintroduced the AdS length l.

At this point, we choose a gauge. A convenient gauge is the so-called *quasi spherical-gauge* [83], in which the full solution, to all orders in $\mathcal{E}$, can be written as

$$ds^2 = -\left(1 + \frac{r^2}{l^2}\right) Q_1(r,\chi) dt^2 + Q_2(r,\chi) \frac{dr^2}{1+\frac{r^2}{l^2}} + Q_3(r,\chi)\, r^2 \left[\frac{d\chi^2}{1-\chi^2} + (1-\chi^2) d\phi^2\right] . \tag{A.3}$$

This gauge completely fixes all gauge redundancy if and only if the functions Q_i, with $i \in \{1,2,3\}$, depend on r and χ. If the Q_i depend on r only, then one is still able to fix $Q_3 = 1$. Our generic

expansion in $\mathcal{E}$ can now be applied to our specific line elements, and yields

$$Q_i(r,\chi) = 1 + \sum_{j=1}^{+\infty} q_i^{(2j)}(r,\chi)\,\mathcal{E}^{2j}\,, \qquad \mathcal{A}_t(r,\chi) = \sum_{j=0}^{+\infty} a_t^{(2j+1)}(r,\chi)\,\mathcal{E}^{2j+1}\,. \tag{A.4}$$

At linear order in $\mathcal{E}$ one obtains a second order differential equation for $a_t^{(1)}$ that can be readily solved using separation of variables

$$a_t^{(1)}(r,\chi) = \sum_{\ell=0}^{+\infty} a_\ell \,\frac{\Gamma\left(\frac{\ell+1}{2}\right)\Gamma\left(\frac{\ell+3}{2}\right)}{\Gamma\left(\ell+\frac{3}{2}\right)}\,{}_2F_1\left(\frac{\ell}{2}+\frac{1}{2},\frac{\ell}{2},\ell+\frac{3}{2},-\frac{r^2}{l^2}\right)L_\ell(\chi)\,, \tag{A.5}$$

where $L_\ell(\chi)$ is a Legendre polynomial of degree ℓ, ${}_2F_1$ is the Gaussian Hypergeometric function and the a_ℓ are real numbers that depend on the harmonic number ℓ and which fully specify the boundary chemical potential. In particular, the factors of Γ ensure that

$$\lim_{r\to+\infty} a_t^{(1)}(r,\chi) = \sum_{\ell=0}^{+\infty} a_\ell L_\ell(\chi)\,. \tag{A.6}$$

In our concrete example, we want $a_1 = 1$ and $a_\ell = 0$ for $\ell \neq 1$. This in turn gives the following expression for $a_t^{(1)}$

$$a_t^{(1)}(r,\chi) = \frac{2}{\pi r^2}\left[\left(l^2+r^2\right)\arctan\left(\frac{r}{l}\right) - lr\right]\chi\,. \tag{A.7}$$

We can now proceed to second order. Essentially, we want to solve for a metric perturbation sourced by a stress energy tensor generated by (A.7). In four spacetime dimensions, metric perturbations about spacetimes which have $SO(3)$ symmetry fall within one of two classes: scalar-type gravitational perturbations and vector-type gravitational perturbations [84, 85, 86, 87]. Within our symmetry class, the quasi spherical gauge kills all vector-type modes, and we are just left with the scalars which makes the problem considerably simpler.

Scalar-type gravitational modes are labelled by spherical harmonics of degree $\widetilde{\ell}$. Since at the linear level the gauge field consists of a single harmonic with $\ell = 1$, we can use the usual decomposition of the product of spherical harmonics into its sum to conclude that the metric perturbation will admit the following decomposition

$$q_i^{(2)} = \alpha_i(r)L_0(\chi) + \beta_i(r)L_2(\chi)\,, \tag{A.8}$$

where we can use the residual gauge freedom of the sector independent of χ to set $\alpha_3(r) = 0$. It is rather trivial to solve these equations subject to normalisability at the conformal boundary and

regularity at the centre of AdS. For completeness, we present the final expressions below

$$\alpha_1(r) = \frac{l^2}{3\pi^2 r^4 \left(l^2+r^2\right)}\Bigg[4l^4r^2 + 3\left(\pi^2-4\right)l^2r^4 - 8lr\left(l^4+3l^2r^2+3r^4\right)\arctan\left(\frac{r}{l}\right) + 4\left(l^6+l^4r^2-3l^2r^4-3r^6\right)\arctan\left(\frac{r}{l}\right)^2 + 3\pi^2 r^6\Bigg], \quad \text{(A.9a)}$$

$$\alpha_2(r) = -\frac{8l^5}{3\pi^2 r^4 \left(l^2+r^2\right)}\left[l\left(l^2+r^2\right)\arctan\left(\frac{r}{l}\right)^2 + lr^2 - \left(2l^2r+r^3\right)\arctan\left(\frac{r}{l}\right)\right], \quad \text{(A.9b)}$$

$$\beta_1(r) = \frac{l^3}{12\pi^2 r^4 \left(l^2+r^2\right)}\Bigg\{-lr^2\left[\left(9\pi^2-8\right)l^2 + 5\left(8+3\pi^2\right)r^2\right] + 32l\left(l^2+r^2\right)^2\arctan\left(\frac{r}{l}\right)^2 + r\left[\left(9\pi^2-40\right)l^4 + 2\left(9\pi^2-8\right)l^2r^2 + \left(9\pi^2-40\right)r^4\right]\arctan\left(\frac{r}{l}\right)\Bigg\}, \quad \text{(A.9c)}$$

$$\beta_2(r) = \frac{l^3}{12\pi^2 r^4 \left(l^2+r^2\right)}\Bigg\{lr^2\left[\left(56+9\pi^2\right)l^2 + 5\left(8+3\pi^2\right)r^2\right] + 32l\left(l^2+r^2\right)^2\arctan\left(\frac{r}{l}\right)^2 - r\left[\left(88+9\pi^2\right)l^4 + 2\left(56+9\pi^2\right)l^2r^2 + \left(9\pi^2-40\right)r^4\right]\arctan\left(\frac{r}{l}\right)\Bigg\}, \quad \text{(A.9d)}$$

$$\beta_3(r) = -\frac{l^2}{12\pi^2 r^4}\Bigg\{r^2\left[12\pi^2r^2 - \left(8+9\pi^2\right)l^2\right] + lr\left[\left(9\pi^2-8\right)l^2 - \left(56+9\pi^2\right)r^2\right]\arctan\left(\frac{r}{l}\right) + 16\left(l^4+4l^2r^2-3r^4\right)\arctan\left(\frac{r}{l}\right)^2\Bigg\}. \quad \text{(A.9e)}$$

At third order in $\mathcal{E}$ the calculation becomes more complicated. In particular, for $a_t^{(3)}$ one now has the following decomposition

$$a_t^{(3)} = f_1(r)L_1(\chi) + f_3(r)L_3(\chi), \quad \text{(A.10)}$$

where normalisability and regularity dictate (all functions are real)

$$
\begin{aligned}
f_1(r) = \frac{8l^2}{525\pi^3 r^6}\Bigg[&25l^6 + 247l^4r^2 - 425l^2r^4 + \\
&288r^4\left(l^2+r^2\right)\log\left(\frac{2ir}{l+ir}\right) + 288ilr^5 - 359r^6\Bigg]\arctan\left(\frac{r}{l}\right)^3 \\
&+ \frac{l^2}{350\pi^3 r^5}\arctan\left(\frac{r}{l}\right)^2\Bigg\{4608ir^3\left(l^2+r^2\right)\mathrm{Li}_2\left(\frac{l-ir}{l+ir}\right) + \\
&l\left[15\left(7\pi^2-8\right)l^4 - 2\left(1816+105\pi^2\right)l^2r^2 + 4608r^4\log\left(\frac{2ir}{l+ir}\right) - \left(5752+315\pi^2\right)r^4\right]\Bigg\} + \\
&\frac{l^2}{5250\pi^3 r^3}\Bigg\{25\left(88+63\pi^2\right)l^3 + 8640r\left[4lr\mathrm{Li}_3\left(\frac{l-ir}{l+ir}\right) - 8i\left(l^2+r^2\right)\mathrm{Li}_4\left(\frac{l-ir}{l+ir}\right) - 9lr\zeta(3)\right] \\
&+ 768i\pi^4 l^2 r + 10lr^2\left[13512 + \pi^2(576\log 2 - 193)\right] + 768i\pi^4 r^3\Bigg\} + \\
&\frac{l^2}{525\pi^3 r^4}\arctan\left(\frac{r}{l}\right)\Bigg\{864r^2\left[12\left(l^2+r^2\right)\mathrm{Li}_3\left(\frac{l-ir}{l+ir}\right) + 9\zeta(3)\left(l^2+r^2\right) + 8ilr\mathrm{Li}_2\left(\frac{l-ir}{l+ir}\right)\right] \\
&- 15\left(16+21\pi^2\right)l^4 - 4l^2r^2\left[2510 + \pi^2(144\log 2 - 127)\right] + 2\pi^2 r^4(359 - 288\log 2)\Bigg\}, \quad \text{(A.11a)}
\end{aligned}
$$

$$
\begin{aligned}
f_3(r) = \frac{8l^2}{525\pi^3 r^6}\Bigg[&175l^6 + 313l^4r^2 - 240il^3r^3 + 195l^2r^4 - 48r^2\left(l^2+r^2\right)\left(5l^2+r^2\right)\log\left(\frac{2ir}{l+ir}\right) \\
&- 208ilr^5 + 89r^6\Bigg]\arctan\left(\frac{r}{l}\right)^3 + \frac{l^2}{700\pi^3 r^5}\arctan\left(\frac{r}{l}\right)^2\Bigg\{l\Bigg[35\left(9\pi^2-136\right)l^4 + 6\left(984+245\pi^2\right)l^2r^2 - \\
&512\left(15l^2r^2+13r^4\right)\log\left(\frac{2ir}{l+ir}\right) + \left(3944+1155\pi^2\right)r^4\Bigg] - 1536ir\left(l^2+r^2\right)\left(5l^2+r^2\right)\mathrm{Li}_2\left(\frac{l-ir}{l+ir}\right)\Bigg\} + \\
&\frac{l^2}{525\pi^3 r^4}\arctan\left(\frac{r}{l}\right)\Bigg\{5l^4\left[2016 + \pi^2(515 + 96\log 2)\right] - 384i\left(15l^3r + 13lr^3\right)\mathrm{Li}_2\left(\frac{l-ir}{l+ir}\right) - \\
&432\left(l^2+r^2\right)\left(5l^2+r^2\right)\left[3\zeta(3) + 4\mathrm{Li}_3\left(\frac{l-ir}{l+ir}\right)\right] + 3l^2r^2\left[560 + \pi^2(589 + 192\log 2)\right] + 2\pi^2 r^4(48\log 2 - 89)\Bigg\} \\
&+ \frac{l^2}{31500\pi^3 r^4}\Bigg\{2880\Bigg[24i\left(l^2+r^2\right)\left(5l^2+r^2\right)\mathrm{Li}_4\left(\frac{l-ir}{l+ir}\right) - 4\left(15l^3r + 13lr^3\right)\mathrm{Li}_3\left(\frac{l-ir}{l+ir}\right) + \\
&9lr\zeta(3)\left(15l^2+13r^2\right)\Bigg] - 3840i\pi^4 l^4 - 75l^3r\left[6328 + \pi^2(2249 + 384\log 2)\right] \\
&- 4608i\pi^4 l^2 r^2 - 20lr^3\left[11016 + \pi^2(5561 + 1248\log 2)\right] - 768i\pi^4 r^4\Bigg\}, \quad \text{(A.11b)}
\end{aligned}
$$

where $\mathrm{Li}_k(x)$ is a polylogarithm function of order k, and $\zeta(x)$ is the Riemann zeta function. At linear order in $\mathcal{E}$ we recover the results of [88].

Appendix B

Perturbative Analysis for Chapter 5

Before solving the equations of motion for the ansatz (5.8) numerically, it is useful to study the perturbative solution to third order in $\mathcal{E}$ as we did for the previous case without a scalar. Again we will consider a metric ansatz in the quasi spherical gauge, with the metric and gauge field expanded in even and odd powers of $\mathcal{E}$, respectively. The expansion for the scalar takes the form

$$\Phi = \sum_{j=0}^{+\infty} f^{(2j)} \mathcal{E}^{2j}. \tag{B.1}$$

The scalar field only appears as backreacted by the dipolar source; it does not enter at leading order in $\mathcal{E}$. At linear order, the result for the gauge field is the same as in section A. At second order, the scalar is labeled by the spherical harmonics like the metric perturbations.

$$Q_i(r,\theta) = 1 + \sum_{j=1}^{+\infty} q_i^{(2j)}(r,\theta)\, \mathcal{E}^{2j}\,. \tag{B.2}$$

The only nontrivial contributions come from $\ell = 0$ and $\ell = 2$, admitting a composition of the form

$$q_i^{(2)} = \alpha_i(r) L_0(\theta) + \beta_i(r) L_2(\theta) \qquad f^2 = \alpha_5(r) L_0(\theta) + \beta_5(r) L_2(\theta) \tag{B.3}$$

The residual gauge freedom is again fixed by setting $\alpha_3(r) = 0$. Solving the equations of motion at this order subject to normalizability at the conformal boundary and regularity at the AdS center

gives

$$\alpha_1(r) = \frac{2\left(l^6 - 3l^2y^4\right)\left(\tan^{-1}\left(\frac{y}{l}\right)\right)^2}{3\pi^2y^4} + \frac{1}{3}\left(\frac{3l^2}{2} + \frac{2l^4\left(\frac{1}{y^2} - \frac{4}{l^2+y^2}\right)}{\pi^2}\right) - \frac{4\left(l^7 + 3l^5y^2 + 3l^3y^4\right)\tan^{-1}\left(\frac{y}{l}\right)}{3\pi^2y^3\left(l^2+y^2\right)}, \tag{B.4a}$$

$$\alpha_2(r) = -\frac{4l^5\left(l\tan^{-1}\left(\frac{y}{l}\right) - y\right)\left(l^2\tan^{-1}\left(\frac{y}{l}\right) + y^2\tan^{-1}\left(\frac{y}{l}\right) - ly\right)}{3\pi^2y^4\left(l^2+y^2\right)}, \tag{B.4b}$$

$$\beta_1(r) = -\frac{l^4\left(\left(9\pi^2-8\right)l^2 + 5\left(8+3\pi^2\right)y^2\right)}{24\pi^2y^2\left(l^2+y^2\right)} + \frac{4l^4\left(l^2+y^2\right)\tan^{-1}\left(\frac{y}{l}\right)^2}{3\pi^2y^4} + \frac{l^3\left(\left(9\pi^2-40\right)l^4 + 2\left(9\pi^2-8\right)l^2y^2 + \left(9\pi^2-40\right)y^4\right)\tan^{-1}\left(\frac{y}{l}\right)}{24\pi^2y^3\left(l^2+y^2\right)}, \tag{B.4c}$$

$$\beta_2(r) = \frac{l^4\left(\left(56+9\pi^2\right)l^2 + 5\left(8+3\pi^2\right)y^2\right)}{24\pi^2y^2\left(l^2+y^2\right)} + \frac{4l^4\left(l^2+y^2\right)\tan^{-1}\left(\frac{y}{l}\right)^2}{3\pi^2y^4} - \frac{l^3\left(\left(88+9\pi^2\right)l^4 + 2\left(56+9\pi^2\right)l^2y^2 + \left(9\pi^2-40\right)y^4\right)\tan^{-1}\left(\frac{y}{l}\right)}{24\pi^2y^3\left(l^2+y^2\right)}, \tag{B.4d}$$

$$\beta_3(r) = \frac{1}{24}l^2\left(\frac{\left(8+9\pi^2\right)l^2}{\pi^2y^2} - 12\right) + \frac{l^3\left(\left(8-9\pi^2\right)l^2 + \left(56+9\pi^2\right)y^2\right)\tan^{-1}\left(\frac{y}{l}\right)}{24\pi^2y^3} - \frac{2\left(l^6 + 4l^4y^2 - 3l^2y^4\right)\tan^{-1}\left(\frac{y}{l}\right)^2}{3\pi^2y^4}. \tag{B.4e}$$

$$\alpha_5(r) = -\frac{l^3\left(4\left(l^3 - ly^2\right)\tan^{-1}\left(\frac{y}{l}\right)^2 - \left(8l^2y + \left(\pi^2-4\right)y^3\right)\tan^{-1}\left(\frac{y}{l}\right) + 4ly^2\right)}{6\pi^2y^4}, \tag{B.4f}$$

$$\beta_5(r) = -\frac{l^3\left(8\left(l^3 + 2ly^2\right)\tan^{-1}\left(\frac{y}{l}\right)^2 + y\left(\left(2+3\pi^2\right)l^2 + \left(\pi^2-10\right)y^2\right)\tan^{-1}\left(\frac{y}{l}\right) + \left(10+3\pi^2\right)(-l)y^2\right)}{6\pi^2y^4}. \tag{B.4g}$$

We can write the gauge field at third order as

$$a_t^{(3)} = f_1(r)L_1(\chi) + f_3(r)L_3(\chi). \tag{B.5}$$

At third order, the gauge field can be written as

$$a_t^{(3)} = f_1(r)L_1(\chi) + f_3(r)L_3(\chi), \tag{B.6}$$

Regularity at the origin and normalisability impose that these are real functions given by

$$
\begin{aligned}
f_1(y) = \frac{8l^2\tan^{-1}\left(\frac{y}{l}\right)^3}{525\pi^3y^6}\Big(&65l^6+176l^4y^2+144Ily^5+2l^2y^4(-115+72\log(2))\\
&+y^6(-197+144\log(2))+144y^4(l^2+y^2)(\log(y)-\log(-Il+y))\Big)\\
&+\frac{l^2\tan^{-1}\left(\frac{y}{l}\right)^2}{700\pi^3y^5}\left(4608iy^3\left(l^2+y^2\right)\mathrm{Li}_2\left(\frac{l-iy}{l+iy}\right)+l\left(5\left(49\pi^2-192\right)l^4\right.\right.\\
&-8\left(594+35\pi^2\right)l^2y^2+4608y^4(\log(y)-\log(y-il))+y^4\left(-525\pi^2-6032+4608\log(2)\right)\Big)\Big)\\
&+\frac{l^2}{10500\pi^3y^3}\Big[3675\pi^2l^3+6400l^3-69120iy\left(l^2+y^2\right)\mathrm{Li}_4\left(\frac{l-iy}{l+iy}\right)+768i\pi^4l^2y+34560ly^2\mathrm{Li}_3\left(\frac{l-iy}{l+iy}\right)\\
&-77760ly^2\zeta(3)+2620\pi^2ly^2+143520ly^2+5760\pi^2ly^2\log(2)+768i\pi^4y^3\Big]\\
&-\frac{l^2\tan^{-1}\left(\frac{y}{l}\right)}{1050\pi^3y^4}\left(735\pi^2l^4+240l^4-10368y^2\left(l^2+y^2\right)\mathrm{Li}_3\left(\frac{l-iy}{l+iy}\right)-7776l^2y^2\zeta(3)\right.\\
&-158\pi^2l^2y^2+10040l^2y^2+576\pi^2l^2y^2\log(2)-6912ily^3\mathrm{Li}_2\left(\frac{l-iy}{l+iy}\right)-7776y^4\zeta(3)\\
&\left.-788\pi^2y^4+576\pi^2y^4\log(2)\right)
\end{aligned}
\tag{B.7a}
$$

$$
\begin{aligned}
f_3(r) = \frac{4l^2\tan^{-1}\left(\frac{y}{l}\right)^3}{525\pi^3y^6}\Big(&245l^6+558l^4y^2-240il^3y^3+405l^2y^4\\
&+48y^2\left(l^2+y^2\right)\left(5l^2+y^2\right)(-\log(2y)+\log(y-il))-208ily^5+124y^6\Big)\\
&l^2+\frac{1}{1400\pi^3y^5}\tan^{-1}\left(\frac{y}{l}\right)^2\Big[l\left(35\left(21\pi^2-128\right)l^4+2\left(2672+1155\pi^2\right)l^2y^2\right.\\
&+512y^2\left(15l^2+13y^2\right)(-\log(2y)+\log(y-il))+\left(3104+1575\pi^2\right)y^4\Big)\\
&\left.-1536iy\left(l^2+y^2\right)\left(5l^2+y^2\right)\mathrm{Li}_2\left(\frac{l-iy}{l+iy}\right)\right]\\
&+\frac{l^2}{63000\pi^3y^4}\left(-3840i\pi^4l^4-11520\left(15l^3y+13ly^3\right)\mathrm{Li}_3\left(\frac{l-iy}{l+iy}\right)+388800l^3y\zeta(3)\right.\\
&-191775\pi^2l^3y-520800l^3y-28800\pi^2l^3y\log(2)-4608i\pi^4l^2y^2\\
&+69120i\left(5l^4+6l^2y^2+y^4\right)\mathrm{Li}_4\left(\frac{l-iy}{l+iy}\right)+336960ly^3\zeta(3)-135020\pi^2ly^3-270720ly^3\\
&\left.-24960\pi^2ly^3\log(2)-768i\pi^4y^4\right)\\
&+\frac{l^2}{1050\pi^3y^4}\tan^{-1}\left(\frac{y}{l}\right)\Big[-6480l^4\zeta(3)+2645\pi^2l^4+10080l^4+480\pi^2l^4\log(2)\\
&-384i\left(15l^3y+13ly^3\right)\mathrm{Li}_2\left(\frac{l-iy}{l+iy}\right)-7776l^2y^2\zeta(3)+1767\pi^2l^2y^2+1680l^2y^2\\
&+576\pi^2l^2y^2\log(2)-1728\left(5l^4+6l^2y^2+y^4\right)\mathrm{Li}_3\left(\frac{l-iy}{l+iy}\right)-1296y^4\zeta(3)-248\pi^2y^4+96\pi^2y^4\log(2)\Big]
\end{aligned}
\tag{B.7b}
$$

where $\mathrm{Li}_k(x)$ is a polylogarithm function of order k, and $\zeta(x)$ is the Riemann zeta function.

Appendix C

Perturbative Analysis for Chapter 6

We begin by expanding the functions using the spherical harmonics outlined in section 2,

$$A = 1 + \widehat{\mu}^2 y^2 \sum_l q_{1,l}(y)\mathbb{S}_l(x) + O(\widehat{\mu}^4)\,, \qquad B = 1 + \widehat{\mu}^2 y^2 \sum_l q_{2,l}(y)\mathbb{S}_l(x) + O(\widehat{\mu}^4)\,, \tag{C.1}$$

$$T_4 = 1 + \widehat{\mu}^2 y^2 \sum_l q_{7,l}(y)\mathbb{S}_l(x) + O(\widehat{\mu}^4)\,, \qquad \Omega = 1 + \widehat{\mu}^2 y^2 \sum_l q_{8,l}(y)\mathbb{S}_l(x) + O(\widehat{\mu}^4)\,,$$

$$F = \widehat{\mu}^2 y^6 \sqrt{1-y} \sum_l q_{3,l}(y)\partial_x \mathbb{S}_l(x) + O(\widehat{\mu}^4)\,, \qquad Q = 1 + \widehat{\mu}^2 y^5 \sum_l q_l(y)\mathbb{S}_l(x) + O(\widehat{\mu}^4)\,,$$

$$T_{ij} = \widehat{\mu}^2 y^5 \sum_l \left[\widetilde{q}_l(y)\Delta_{ij}\mathbb{S}_l(x) + \widehat{q}_l(y)\mathbb{T}_{ij}(x)\right] + O(\widehat{\mu}^4)\,,$$

$$M = \sqrt{1-y}\; y^{-3}\widehat{\mu} \sum_k q_{9,k}(y)\mathbb{H}_k(x) + O(\widehat{\mu}^3)\,, \qquad L = \frac{3}{2} y^4 \widehat{\mu} \sum_k q_{10,k}(y)\mathbb{H}_k(x) + O(\widehat{\mu}^3)\,,$$

where Q and T_{ij} were introduced in (6.46). We plug this Ansatz into the equations of motion and expand them up to $O(\widehat{\mu}^2)$. In particular, the equation of motion $d \star dC = 0$ gives rise to linear ODEs for the functions $q_{9,l}(y)$ and $q_{10,l}(y)$. Moreover, the boundary conditions discussed in section 6.3.2 imply that the only non-zero modes are $q_{9,1}(y)$ and $q_{10,1}(y)$. We find these functions using a single variable version of the Chebyshev method described in the main text to reduce the two linear ODEs to a set of linear algebraic equations, which can easily be solved using Newton's method (we solve the equations in the $\widetilde{y}$ coordinates because this simplifies the boundary conditions on the horizon).

The harmonic Einstein equations $E_{ab} = 0$, expanded up to $O(\widehat{\mu}^2)$, can also be decomposed into

spherical harmonics. The equations of scalar type are $E_{\tau\tau}$, E_{yy}, E_{zz}, and $E_{\tau z}$. For example

$$E_{\tau\tau}(x,y) = \sum_l \mathbb{S}_l(x) f_{1,l}(y). \tag{C.2}$$

The vector equation E_{yi} (where i runs over the S^8 coordinates) can be decomposed as follows

$$E_{yi}(x,y) = \sum_l \partial_i \mathbb{S}_l(x) f_{3,l}(y) \quad \Rightarrow \quad \nabla^i E_{yi}(x,y) = -\sum_l \lambda_l \mathbb{S}_l(x) f_{3,l}(y).$$

Finally, we can use the tracelessness of the tensor harmonics as well as the divergence-less nature of $\mathbb{T}_{ij}$ to write the components of the Harmonic Einstein equations corresponding to the S^8

$$E_{ij} = \sum_l \left(h_{ij} \mathbb{S}_l(x) f_l(y) + \Delta_{ij} \mathbb{S}_l(x) \widetilde{f}_l(y) + \mathbb{T}_{ij}(x) \widehat{f}_l(y) \right) \tag{C.3}$$

$$\Rightarrow h^{ij} E_{ij} = 8 \sum_l \mathbb{S}_l(x) f_l(y)\,, \qquad \nabla^i \nabla^j E_{ij} = -\sum_l \left[\lambda_l f_l(y) + \frac{7}{8} \lambda_l \left(1 - \lambda_l\right) \widetilde{f}_l(y) \right] \mathbb{S}_l(x)\,.$$

Written in this way, the equations $E_{ab} = 0$ can easily be projected onto a basis of the scalar harmonics, resulting in a system of seven ODEs,

$$f_{1,l}(y) = f_{2,l}(y) = f_{7,l}(y) = f_{8,l}(y) = f_{3,l}(y) = f_l(y) = \widetilde{f}_l(y) = 0\ . \tag{C.4}$$

These ODEs are linear in the functions $q_{1,l}(y), q_{2,l}(y), q_{7,l}(y), q_{8,l}(y), q_{3,l}(y), q_l(y), \widetilde{q}_l(y)$ and quadratic in the functions $q_{9,l}(y)$ and $q_{10,l}(y)$ that can be previously determined from the gauge field equation of motion $d \star dC = 0$. [1] The terms quadratic in the known functions $q_{9,l}(y)$ and $q_{10,l}(y)$ can be thought of as sources in the linear equations for the other 7 functions. This gives rise to 7 linear non-homogeneous ODEs which can easily be solved using spectral methods. To this order in $\widehat{\mu}$, the sources are only non-zero for $l = 0$ and $l = 2$.

The normalizable modes can be extracted from the solutions by comparing their behavior with the asymptotic expansions of the fields. In particular,

$$\frac{\alpha_1}{\widehat{\mu}} = \frac{3}{4} \partial_y^2 q_{10,1}(0) + O(\widehat{\mu}^2) \approx -0.4765 + O(\widehat{\mu}^2)\,, \tag{C.5}$$

$$\frac{\beta_2}{\widehat{\mu}^2} = -q_{1,2}(0) + O(\widehat{\mu}^2) \approx 0.0732 + O(\widehat{\mu}^2)\,, \tag{C.6}$$

$$\frac{\gamma}{\widehat{\mu}^2} = \frac{1}{2} \partial_y^2 q_0(0) + O(\widehat{\mu}^2) \approx 0.0624 + O(\widehat{\mu}^2)\,, \tag{C.7}$$

$$\frac{\delta}{\widehat{\mu}^2} = \frac{1}{2} \partial_y^2 q_{2,0}(0) + O(\widehat{\mu}^2) \approx -0.5809 + O(\widehat{\mu}^2)\,. \tag{C.8}$$

[1] Note that the equation $\widehat{f}_l(y) = 0$ is automatically satisfied setting $\widehat{q}_l(y) = 0$.

These values satisfy the Komar identities developed later (**??**, 6.68) and provide a non-trivial check of the numerics as shown in Figure 8.

Another way to see that we have chosen the correct boundary conditions is to recall the asymptotics of the vacuum solutions, expressed as a collection of charged discs as in [9]. These must have the same asymptotic behavior as the deformed black brane solutions we will find. The potential at large $z \sim \rho$ is ,

$$V = \rho^2 z - \frac{2}{3} z^3 + \frac{1}{60} \sum_{l \, \text{odd}} \frac{2^{-l} \, a_l}{(\rho^2 + z^2)^{\frac{l+1}{2}}} P_l \left(\frac{z}{\sqrt{\rho^2 + z^2}} \right) \tag{C.9}$$

where the P_l is the Legendre polynomial and a_l characterize each specific vacuum because they are multipoles of the charge distribution that sources the potential V. Inserting this expansion of the potential in the solution (6.10) we obtain an asymptotic expansion that can be compared with the asymptotic expansion of our Ansatz (6.15) discussed in section 6.3.2. More precisely, we perform the following change of coordinates in our Ansatz (6.15)

$$d\eta = -\frac{dt}{\sqrt{a_1}} \ , \qquad d\zeta = 2\sqrt{a_1} dx_{11} + \phi_0 \frac{dt}{\sqrt{a_1}} \ , \tag{C.10}$$

$$y = \frac{1}{2\sqrt{\rho^2 + z^2}} \left[1 + \dots \right] , \qquad x = \left(1 - \frac{\rho}{\sqrt{\rho^2 + z^2}} \right)^{\frac{1}{2}} \left[1 + \dots \right]$$

where the dots denote terms suppressed by powers of $\sqrt{\rho^2 + z^2}$ that are determined so that our Ansatz (6.15) has the same type of asymptotic expansion as the vacuum solutions (6.10). This comparison leads to the following relations

$$\widehat{\mu} = 2\sqrt{a_1} \ , \qquad \beta_2 = \frac{a_3}{a_1} \ , \qquad \beta_4 = \frac{a_5}{a_1} \ , \qquad \beta_6 = \frac{a_7}{a_1} \ , \tag{C.11}$$

$$\alpha_1 = \frac{49 a_3}{33\sqrt{a_1}} \ , \qquad \alpha_3 = -\frac{63 a_5}{10\sqrt{a_1}} \ , \qquad \alpha_5 = \frac{2541 a_7}{152\sqrt{a_1}} \ , \tag{C.12}$$

$$\gamma = \frac{5}{14} + \frac{149 a_3}{396} + \phi_0 \ , \qquad \delta = -\frac{22}{7} - \frac{136 a_3}{99} - 6\phi_0 \ . \tag{C.13}$$

In other words, the vacuum geometries of [8, 9] have an asymptotic expansion of the form of section 6.3.2 with all the parameters given in terms of the multipoles a_l and an arbitrary constant ϕ_0 that represents the freedom to shift the potential associated to the D0-brane charge (from the 10-dimensional point of view). In addition, the parameter $\widetilde{\beta}_2$, that appears for example in (6.58), vanishes in all vacuum solutions. This confirms our interpretation of β_2 as a state dependent response and $\widetilde{\beta}_2$ as a source that deforms the theory.

Bibliography

[1] O. Aharony, O. Bergman, D. L. Jafferis, and J. Maldacena, "N=6 superconformal Chern-Simons-matter theories, M2-branes and their gravity duals," *JHEP* **0810** (2008) 091, arXiv:0806.1218 [hep-th].

[2] T. Eguchi and H. Kawai, "Reduction of Dynamical Degrees of Freedom in the Large N Gauge Theory," *Phys.Rev.Lett.* **48** (1982) 1063.

[3] T. Banks, W. Fischler, S. H. Shenker, and L. Susskind, "M theory as a matrix model: A conjecture," *Phys. Rev.* **D55** (1997) 5112–5128, arXiv:hep-th/9610043.

[4] M. Hanada, Y. Hyakutake, J. Nishimura, and S. Takeuchi, "Higher derivative corrections to black hole thermodynamics from supersymmetric matrix quantum mechanics," *Phys. Rev. Lett.* **102** (2009) 191602, arXiv:0811.3102 [hep-th].

[5] M. Hanada, Y. Hyakutake, G. Ishiki, and J. Nishimura, "Holographic description of quantum black hole on a computer," arXiv:1311.5607 [hep-th].

[6] D. E. Berenstein, J. M. Maldacena, and H. S. Nastase, "Strings in flat space and pp waves from N = 4 super Yang Mills," *JHEP* **04** (2002) 013, arXiv:hep-th/0202021.

[7] M. S. Costa, L. Greenspan, J. Penedones, and J. Santos, "Thermodynamics of the BMN matrix model at strong coupling," *JHEP* **03** (2015) 069, arXiv:1411.5541 [hep-th].

[8] H. Lin, O. Lunin, and J. M. Maldacena, "Bubbling AdS space and 1/2 BPS geometries," *JHEP* **0410** (2004) 025, arXiv:hep-th/0409174 [hep-th].

[9] H. Lin and J. M. Maldacena, "Fivebranes from gauge theory," *Phys. Rev.* **D74** (2006) 084014, arXiv:hep-th/0509235.

[10] D. Kastor, "Komar Integrals in Higher (and Lower) Derivative Gravity," *Class. Quant. Grav.* **25** (2008) 175007, arXiv:0804.1832 [hep-th].

[11] S. Catterall and G. van Anders, "First Results from Lattice Simulation of the PWMM," *JHEP* **09** (2010) 088, arXiv:1003.4952 [hep-th].

[12] J. M. Maldacena, "The Large N limit of superconformal field theories and supergravity," *Int. J. Theor. Phys.* **38** (1999) 1113–1133, arXiv:hep-th/9711200 [hep-th]. [Adv. Theor. Math. Phys.2,231(1998)].

[13] J. Polchinski, *String Theory: Volume 2, Superstring Theory and Beyond*. Cambridge Monographs on Mathematical Physics. Cambridge University Press, 1998. https://books.google.ca/books?id=WKatSc5pjOgC.

[14] D. Tong, "String Theory," arXiv:0908.0333 [hep-th].

[15] M. Ammon and J. Erdmenger, *Gauge/Gravity Duality: Foundations and Applications*. Cambridge University Press, 2015. https://books.google.ca/books?id=GOOsoAEACAAJ.

[16] H. Năstase, *Introduction to the AdS/CFT Correspondence*. Cambridge University Press, 2015. https://books.google.ca/books?id=yHIQrgEACAAJ.

[17] J. M. Bardeen, B. Carter, and S. W. Hawking, "The four laws of black hole mechanics," *Comm. Math. Phys.* **31** no. 2, (1973) 161–170. http://projecteuclid.org/euclid.cmp/1103858973.

[18] J. D. Brown and J. W. York, Jr., "Quasilocal energy and conserved charges derived from the gravitational action," *Phys. Rev.* **D47** (1993) 1407–1419, arXiv:gr-qc/9209012 [gr-qc].

[19] K. Skenderis, "Lecture notes on holographic renormalization," *Class. Quant. Grav.* **19** (2002) 5849–5876, arXiv:hep-th/0209067 [hep-th].

[20] V. Balasubramanian and P. Kraus, "A Stress tensor for Anti-de Sitter gravity," *Commun. Math. Phys.* **208** (1999) 413–428, arXiv:hep-th/9902121 [hep-th].

[21] S. de Haro, S. N. Solodukhin, and K. Skenderis, "Holographic reconstruction of space-time and renormalization in the AdS / CFT correspondence," *Commun. Math. Phys.* **217** (2001) 595–622, arXiv:hep-th/0002230 [hep-th].

[22] T. Wiseman, *Numerical construction of static and stationary black holes.* 2011. arXiv:1107.5513 [gr-qc]. http://inspirehep.net/record/920553/files/arXiv:1107.5513.pdf.

[23] M. Headrick, S. Kitchen, and T. Wiseman, "A New approach to static numerical relativity, and its application to Kaluza-Klein black holes," *Class.Quant.Grav.* **27** (2010) 035002, arXiv:0905.1822 [gr-qc].

[24] O. J. C. Dias, J. E. Santos, and B. Way, "Numerical Methods for Finding Stationary Gravitational Solutions," arXiv:1510.02804 [hep-th].

[25] P. Figueras, J. Lucietti, and T. Wiseman, "Ricci solitons, Ricci flow, and strongly coupled CFT in the Schwarzschild Unruh or Boulware vacua," *Class.Quant.Grav.* **28** (2011) 215018, arXiv:1104.4489 [hep-th].

[26] A. Adam, S. Kitchen, and T. Wiseman, "A numerical approach to finding general stationary vacuum black holes," *Class.Quant.Grav.* **29** (2012) 165002, arXiv:1105.6347 [gr-qc].

[27] J. Boyd, *Chebyshev and Fourier Spectral Methods: Second Revised Edition.* Dover Books on Mathematics. Dover Publications, 2001. https://books.google.ca/books?id=lEWnQWyzLQYC.

[28] F. J. Ernst, "A new family of solutions of the Einstein field equations.," *Journal of Mathematical Physics* **18** (1977) 233–234.

[29] C. Fefferman and C. R. Graham, "The ambient metric," arXiv:0710.0919 [math.DG].

[30] V. P. Frolov, "Embedding of the Kerr-Newman black hole surface in Euclidean space," *Phys. Rev.* **D73** (2006) 064021, arXiv:gr-qc/0601104 [gr-qc].

[31] A. Chamblin, R. Emparan, C. V. Johnson, and R. C. Myers, "Charged AdS black holes and catastrophic holography," *Phys. Rev.* **D60** (1999) 064018, arXiv:hep-th/9902170 [hep-th].

[32] A. Chamblin, R. Emparan, C. V. Johnson, and R. C. Myers, "Holography, thermodynamics and fluctuations of charged AdS black holes," *Phys. Rev.* **D60** (1999) 104026, arXiv:hep-th/9904197 [hep-th].

[33] B. Sundborg, "The Hagedorn transition, deconfinement and N=4 SYM theory," *Nucl. Phys.* **B573** (2000) 349–363, arXiv:hep-th/9908001 [hep-th].

[34] A. M. Polyakov, "Gauge fields and space-time," *Int. J. Mod. Phys.* **A17S1** (2002) 119–136, arXiv:hep-th/0110196 [hep-th].

[35] O. Aharony, J. Marsano, S. Minwalla, K. Papadodimas, and M. Van Raamsdonk, "The Hagedorn - deconfinement phase transition in weakly coupled large N gauge theories," *Adv. Theor. Math. Phys.* **8** (2004) 603–696, arXiv:hep-th/0310285 [hep-th]. [,161(2003)].

[36] O. Aharony, O. Bergman, D. L. Jafferis, and J. Maldacena, "N=6 superconformal Chern-Simons-matter theories, M2-branes and their gravity duals," *JHEP* **10** (2008) 091, arXiv:0806.1218 [hep-th].

[37] M. Cvetic, M. J. Duff, P. Hoxha, J. T. Liu, H. Lu, J. X. Lu, R. Martinez-Acosta, C. N. Pope, H. Sati, and T. A. Tran, "Embedding AdS black holes in ten-dimensions and eleven-dimensions," *Nucl. Phys.* **B558** (1999) 96–126, arXiv:hep-th/9903214 [hep-th].

[38] M. S. Costa, L. Greenspan, M. Oliveira, J. Penedones, and J. E. Santos, "Polarised Black Holes in AdS," *Class. Quant. Grav.* **33** no. 11, (2016) 115011, arXiv:1511.08505 [hep-th].

[39] M. Bianchi, R. Poghossian, and M. Samsonyan, "Precision Spectroscopy and Higher Spin symmetry in the ABJM model," *JHEP* **10** (2010) 021, arXiv:1005.5307 [hep-th].

[40] D. Yamada, "Metastability of R-charged black holes," *Class. Quant. Grav.* **24** (2007) 3347–3376, arXiv:hep-th/0701254 [HEP-TH].

[41] P. Basu, C. Krishnan, and P. N. B. Subramanian, "Phases of Global AdS Black Holes," *JHEP* **06** (2016) 139, arXiv:1602.07211 [hep-th].

[42] A. A. Abrikosov, Jr., "Dirac operator on the Riemann sphere," arXiv:hep-th/0212134 [hep-th].

[43] T. Nishioka and T. Takayanagi, "On Type IIA Penrose Limit and N=6 Chern-Simons Theories," *JHEP* **08** (2008) 001, arXiv:0806.3391 [hep-th].

[44] S. A. Hartnoll, C. P. Herzog, and G. T. Horowitz, "Building a Holographic Superconductor," *Phys. Rev. Lett.* **101** (2008) 031601, arXiv:0803.3295 [hep-th].

[45] S. A. Hartnoll, C. P. Herzog, and G. T. Horowitz, "Holographic Superconductors," *JHEP* **12** (2008) 015, arXiv:0810.1563 [hep-th].

[46] O. J. C. Dias, R. Monteiro, H. S. Reall, and J. E. Santos, "A Scalar field condensation instability of rotating anti-de Sitter black holes," *JHEP* **11** (2010) 036, arXiv:1007.3745 [hep-th].

[47] O. J. C. Dias, P. Figueras, S. Minwalla, P. Mitra, R. Monteiro, and J. E. Santos, "Hairy black holes and solitons in global AdS_5," *JHEP* **08** (2012) 117, arXiv:1112.4447 [hep-th].

[48] J. Markeviciute and J. E. Santos, "Hairy black holes in AdS_5 ? S^5," *JHEP* **06** (2016) 096, arXiv:1602.03893 [hep-th].

[49] D. Yamada and L. G. Yaffe, "Phase diagram of N=4 super-Yang-Mills theory with R-symmetry chemical potentials," *JHEP* **09** (2006) 027, arXiv:hep-th/0602074 [hep-th].

[50] J. M. Maldacena, "The large N limit of superconformal field theories and supergravity," *Adv. Theor. Math. Phys.* **2** (1998) 231–252, arXiv:hep-th/9711200.

[51] N. Itzhaki, J. M. Maldacena, J. Sonnenschein, and S. Yankielowicz, "Supergravity and the large N limit of theories with sixteen supercharges," *Phys. Rev.* **D58** (1998) 046004, arXiv:hep-th/9802042.

[52] Y. Hyakutake, "Quantum Near Horizon Geometry of Black 0-Brane," arXiv:1311.7526 [hep-th].

[53] T. Wiseman, "On black hole thermodynamics from super Yang-Mills," *JHEP* **1307** (2013) 101, arXiv:1304.3938 [hep-th].

[54] T. Morita, S. Shiba, T. Wiseman, and B. Withers, "Warm p-soup and near extremal black holes," arXiv:1311.6540 [hep-th].

[55] D. N. Kabat and G. Lifschytz, "Approximations for strongly coupled supersymmetric quantum mechanics," *Nucl.Phys.* **B571** (2000) 419–456, arXiv:hep-th/9910001 [hep-th].

[56] D. N. Kabat, G. Lifschytz, and D. A. Lowe, "Black hole thermodynamics from calculations in strongly coupled gauge theory," *Int.J.Mod.Phys.* **A16** (2001) 856–865, arXiv:hep-th/0007051 [hep-th].

[57] D. N. Kabat, G. Lifschytz, and D. A. Lowe, "Black hole entropy from nonperturbative gauge theory," *Phys.Rev.* **D64** (2001) 124015, arXiv:hep-th/0105171 [hep-th].

[58] Y.-H. Lin, S.-H. Shao, Y. Wang, and X. Yin, "A Low Temperature Expansion for Matrix Quantum Mechanics," arXiv:1304.1593 [hep-th].

[59] S. Catterall and T. Wiseman, "Towards lattice simulation of the gauge theory duals to black holes and hot strings," *JHEP* **0712** (2007) 104, arXiv:0706.3518 [hep-lat].

[60] K. N. Anagnostopoulos, M. Hanada, J. Nishimura, and S. Takeuchi, "Monte Carlo studies of supersymmetric matrix quantum mechanics with sixteen supercharges at finite temperature," *Phys.Rev.Lett.* **100** (2008) 021601, arXiv:0707.4454 [hep-th].

[61] S. Catterall and T. Wiseman, "Black hole thermodynamics from simulations of lattice Yang-Mills theory," *Phys.Rev.* **D78** (2008) 041502, arXiv:0803.4273 [hep-th].

[62] S. Catterall and T. Wiseman, "Extracting black hole physics from the lattice," *JHEP* **1004** (2010) 077, arXiv:0909.4947 [hep-th].

[63] M. Hanada, J. Nishimura, Y. Sekino, and T. Yoneya, "Direct test of the gauge-gravity correspondence for Matrix theory correlation functions," *JHEP* **1112** (2011) 020, arXiv:1108.5153 [hep-th].

[64] S. Catterall, A. Joseph, and T. Wiseman, "Thermal phases of D1-branes on a circle from lattice super Yang-Mills," *JHEP* **1012** (2010) 022, arXiv:1008.4964 [hep-th].

[65] N. Kawahara, J. Nishimura, and K. Yoshida, "Dynamical aspects of the plane-wave matrix model at finite temperature," *JHEP* **0606** (2006) 052, arXiv:hep-th/0601170 [hep-th].

[66] K. Furuuchi, E. Schreiber, and G. W. Semenoff, "Five-brane thermodynamics from the matrix model," arXiv:hep-th/0310286 [hep-th].

[67] S. Hadizadeh, B. Ramadanovic, G. W. Semenoff, and D. Young, "Free energy and phase transition of the matrix model on a plane-wave," *Phys.Rev.* **D71** (2005) 065016, arXiv:hep-th/0409318 [hep-th].

[68] N. Kim, T. Klose, and J. Plefka, "Plane wave matrix theory from N=4 superYang-Mills on R x S**3," *Nucl.Phys.* **B671** (2003) 359–382, arXiv:hep-th/0306054 [hep-th].

[69] O. Aharony, J. Marsano, S. Minwalla, K. Papadodimas, and M. Van Raamsdonk, "The Hagedorn - deconfinement phase transition in weakly coupled large N gauge theories," *Adv.Theor.Math.Phys.* **8** (2004) 603–696, arXiv:hep-th/0310285 [hep-th].

[70] S. Hawking and D. N. Page, "Thermodynamics of Black Holes in anti-De Sitter Space," *Commun.Math.Phys.* **87** (1983) 577.

[71] E. Witten, "Anti-de Sitter space, thermal phase transition, and confinement in gauge theories," *Adv.Theor.Math.Phys.* **2** (1998) 505–532, arXiv:hep-th/9803131 [hep-th].

[72] H. Ling, A. R. Mohazab, H.-H. Shieh, G. van Anders, and M. Van Raamsdonk, "Little string theory from a double-scaled matrix model," *JHEP* **0610** (2006) 018, arXiv:hep-th/0606014 [hep-th].

[73] Y. Sekino and T. Yoneya, "Generalized AdS / CFT correspondence for matrix theory in the large N limit," *Nucl.Phys.* **B570** (2000) 174–206, arXiv:hep-th/9907029 [hep-th].

[74] M. T. Anderson, "On boundary value problems for Einstein metrics," *ArXiv Mathematics e-prints* (Dec., 2006) , math/0612647.

[75] M. T. Anderson, "Extension of symmetries on Einstein manifolds with boundary," *ArXiv e-prints* (Apr., 2007) , arXiv:0704.3373 [math.DG].

[76] H. Lin, "The supergravity duals of the BMN matrix model," *JHEP* **12** (2004) 001, arXiv:hep-th/0407250.

[77] J. M. Maldacena, M. M. Sheikh-Jabbari, and M. Van Raamsdonk, "Transverse five-branes in matrix theory," *JHEP* **0301** (2003) 038, arXiv:hep-th/0211139 [hep-th].

[78] A. Joseph and T. Wiseman, "In preparation,".

[79] B. A. Berg and T. Neuhaus, "Multicanonical ensemble: A new approach to simulate first-order phase transitions," *Phys. Rev. Lett.* **68** (Jan, 1992) 9–12. http://link.aps.org/doi/10.1103/PhysRevLett.68.9.

[80] J. Lee, "New monte carlo algorithm: Entropic sampling," *Phys. Rev. Lett.* **71** (Jul, 1993) 211–214. http://link.aps.org/doi/10.1103/PhysRevLett.71.211.

[81] F. Wang and D. P. Landau, "Determining the density of states for classical statistical models: A random walk algorithm to produce a flat histogram," *Phys. Rev. E* **64** (Oct, 2001) 056101. http://link.aps.org/doi/10.1103/PhysRevE.64.056101.

[82] R. Emparan, T. Harmark, V. Niarchos, and N. A. Obers, "Essentials of Blackfold Dynamics," *JHEP* **1003** (2010) 063, arXiv:0910.1601 [hep-th].

[83] R. Bartnik, "Einstein equations in the null quasispherical gauge," *Class. Quant. Grav.* **14** (1997) 2185–2194, arXiv:gr-qc/9611045 [gr-qc].

[84] T. Regge and J. A. Wheeler, "Stability of a Schwarzschild singularity," *Phys. Rev.* **108** (1957) 1063–1069.

[85] F. J. Zerilli, "Perturbation analysis for gravitational and electromagnetic radiation in a reissner-nordstroem geometry," *Phys. Rev.* **D9** (1974) 860–868.

[86] V. Moncrief, "Gravitational perturbations of spherically symmetric systems. I. The exterior problem.," *Annals Phys.* **88** (1974) 323–342.

[87] H. Kodama and A. Ishibashi, "A Master equation for gravitational perturbations of maximally symmetric black holes in higher dimensions," *Prog. Theor. Phys.* **110** (2003) 701–722, arXiv:hep-th/0305147 [hep-th].

[88] C. Herdeiro and E. Radu, "Anti-de-Sitter regular electric multipoles: Towards EinsteinMaxwell-AdS solitons," *Phys. Lett.* **B749** (2015) 393–398, arXiv:1507.04370 [gr-qc].